AMGAD R. REZK

MICROFLUIDIC ACTUATION ON LITHIUM NIOBATE AND PAPER SUBSTRATES USING MHZ SURFACE AND BULK ACOUSTIC WAVES

MICROFLUIDIC ACTUATION ON LITHIUM NIOBATE AND PAPER SUBSTRATES USING MHZ SURFACE AND BULK ACOUSTIC WAVES

AMGAD R. REZK

A thesis submitted in partial fulfilment of the
requirements for the degree of Doctor of Philosophy

School of Electrical and Computer Engineering
RMIT UNIVERSITY

SUPERVISORS:
PROF. JAMES R. FRIEND and PROF. LESLIE Y. YEO
JANUARY 2014

Amgad R. Rezk: *Microfluidic Actuation on Lithium Niobate and Paper Substrates using MHz Surface and Bulk Acoustic Waves* , A thesis submitted in fulfilment of the requirements for the degree of Doctor of Philosophy, © January 2014

ABSTRACT

Surface acoustic waves are ~ 1 nm amplitude vibrations that can be generated on a piezoelectric material by applying an alternating current. Due to the relatively high frequency (MHz range), the generated surface vibration velocity is typically ~ 1 m/s with a tremendous acceleration of $\sim 10^7$ m/s. For the last decade, SAW have found their way into a wide range of microfluidic applications, and a fascinating variety of fluid and microparticle flow phenomena.

However, the majority of these applications have been without a deep understanding of the governing physics in conjunction with a systematic experimental study; justifiably, due to the complexity of the interactions of these waves with fluids considering the high frequency used, (MHz range), compared to the natural resonance frequecy of these fluids (Hz and KHz range). In this thesis, we demonstrate through experimental, theoretical, and limited numerical study how SAW interacts with microfluidic films and drops, and through the investigation we unravel two novel phenomena of unique fingering instability and soliton-like wave emergence and propagation, although the former — i.e. fingering instability — is akin in appearance to the classical viscous fingering instabilitiy, is distinct as the driving mechanism being the SAW diffraction.

Beyond elucidating the underlying physics governing SAW-driven thin films, we designed an experimental setup comprising the integration of the SAW with microchannels patterned on a wet paper substrate, where a thin film at the paper's tip was drawn out using SAW atomisation, which, led to driving the rest of the fluids at the channel's other ends, leading to fluid mixing along the michrochannels. Mixing was quantified using a novel technique based on hue, which is shown to be a more practical solution compared to the commonly known greyscale method, because of the latter's lack of accuracy with limited colour contrast between fluids.

Beyond the thorough experimental and theoretical understanding and integration with paper-based microfluidics, finally, for cost effectiveness and simplicity of use we trade off SAW with a similar type of waves, in some aspects, known as the Lamb waves to drive a range of microfluidic applications already achieved by SAW. The setup used here is exceptionally simple to the point that, in some cases, only standard aluminium foil is sufficient in simple contact with the lithium niobate substrate to good actuation. Large elastic deformations were achieved causing neublisation of triggering a few μm mono-dispersed mist from a single μL drop or a paper wick.

DECLARATION

In accordance with RMIT University Doctorate Regulation for Doctor of Philosophy regulations the following declarations are made:

I hereby declare that this thesis contains no material which has been accepted for the award of any other degree or diploma at any university or equivalent institution and that, to the best of my knowledge and belief, this thesis contains no material previously published or written by another person, except where due reference is made.

This thesis includes two original papers published in peer reviewed journals and four publications under/about to be submitted for peer review. The core theme of the thesis is microfluidic actuation on lithium niobate and paper substrates including film spreading, fluid mixing, particle pattering, atomisation, amongst other novel phenomena such as unique fingering instabilities and soliton-like wave emergence using surface and bulk MHz frequency acoustic waves. The ideas, development and writing up of all the papers in the thesis were the principal responsibility of myself, the candidate, working within the school of Electrical and computer engineering under the joint supervision of Prof. James Friend and Prof. Leslie Yeo.

The inclusion of co-authors reflects the fact that the work came from active collaboration between researchers and acknowledges input into team-based research. In the case of the each publication reproduced in this thesis (next page), my contribution to the work involved being chief investigator; responsible for the initiation, design, modelling, experimental work, numerical invistigation, results interpretation and writing of the paper.

Amgad R. Rezk

Date

FULL LIST OF RELATED PUBLICATIONS

Journal Articles Included in Thesis

- A. Rezk, O. Manor, J. Friend and L. Yeo, Unique Fingering Instabilities and Soliton-Like Wave Propagation in Thin Acoustowetting Films, *Nature Communications*,3,1167, 2012[1]
- A. Rezk, O. Manor, L. Yeo and J. Friend, Double Flow Reversal in Thin Liquid Films Driven by MHz Order Surface Vibration, *Proc. Roy. Soc. A*, to appear [2]
- O. Manor, A. Rezk, J. Friend and L. Yeo, On the Dynamics of Liquid Films Exposed to High Frequency Surface Vibration, *Journal of Fluid Mechanics*, to be submitted [3]
- A. Rezk, A. Qi, J. Friend, W. Li, and L. Yeo, Uniform Mixing in Paper-Based Microfluidic Systems Using Surface Acoustic Waves, *Lab on a Chip*,12, 773:779, 2012[4]
- A. Rezk, J. Friend and L. Yeo, Poloidal flow in a drop Driven by MHz Order Vibration, under review [5]
- A. Rezk, J. Friend and L. Yeo, Low Cost MHz-Order Acoustomicrofluidics using Aluminium Foil Electrodes, *Lab Chip*,14, 1802:1805, 2014 [6]

Related Journal Articles

- D. Yudistira, A. Boes, A. Rezk, L. Yeo, and J. Friend, A. Mitchell, UV Direct Write Metal Enhanced Redox (MER) Domain Engineering for Realization of Surface Acoustic Devices on Lithium Niobate, Advanced Materials Interfaces. doi: 10.1002/admi.201400006 [7]

Conferences & Symposiums Oral presentations

- A. Rezk, A. Qi, J. Friend, W. Li and L. Yeo, Novel mixing of fluids in paper using SAW, *Smart Nano+ Micro Materials and Devices, Swinburne University*, December, 2011
- A. Rezk, O. Manor, J. Friend and L. Yeo, 30 MHz driven fluid mixing in paper-based microfluidic systems, *Advances in Microfluidics & Nanofluidics, Hong kong*, May, 2012

---

[1] Chapter 2
[2] Chapter 2
[3] Chapter 2
[4] Chapter 3
[5] Chapter 4
[6] Chapter 4
[7] Chapter 5

- A. Rezk, A. Qi, J. Friend, W. Li and L. Yeo, Uniform mixing in paper-based microfluidic systems using surface acoustic waves, *Advances in Microfluidics & Nanofluidics, RMIT Univerisyt, Melbourne, Australia*, December, 2012
- A. Rezk, O. Manor, J. Friend and L. Yeo, Acoustowetting: Film Spreading, Fingering Instabilities and Soliton-Like Wave Propagation, *4th ANZ Nano/Microfluidics Symposium, Adelaide, Australia*, April, 2013
- A. Rezk, A. Qi, J. Friend, W. Li and L. Yeo, Uniform Mixing in Paper-Based Microfluidic Systems Using MHz acoustic waves, *Advances in Microfluidics & Nanofluidics, Notre Dame, USA*, May, 2013
- A. Rezk, O. Manor, J. Friend and L. Yeo, Acoustowetting: Film Spreading, Fingering Instabilities and Soliton-Like Wave Propagation, *Advances in Microfluidics & Nanofluidics, Notre Dame, USA*, May, 2013

Book Chapter

- A. R. Rezk, J. R. Friend and L. Y. Yeo, Actuation mechanisms for microfluidic biomedical devices, *Woodhead Publishing Limited*, 2013

Patent

- Electrode-less generation of bulk and surface vibration on lithium noibate for microfluidic applications, Provisional patent 2013903999, Filed on 17 October 2013

ACKNOWLEDGMENTS

I would like to start by thanking my supervisors Professors James R. Friend and Leslie Y. Yeo for giving me such a great opportunity to be part of your team. Your complementary expertise, spanning across many fields, has given me a unique opportunity and learning experience that enriched my PhD.

Next, I would like to thank all the people that shared my journey along the way; Anushi, Christina, Daniel, Dave, Debadi, Dev, Jess, Jan, Jeremy, Mike, Morteza, Nick, Nooshin, Kai, Ricky, Sarah M., Sarah T., Sean[8]. All of you have helped me in some way or another over my time at the MicroNanophysics Research Laboratory, and in particular I would like to thank Dr. Aisha Qi for technical help and training early in my PhD and Dr. Ofer Manor for working closely and helping guide experiments as well as the mathematical derivation in chapter 2. I also extend my thanks to the Melbourne Centre for Nanofabrication for the use of your facilities, thanks to the staff there that helped me out in the clean room.

Thanks to my parents who have sacrificed *a lot* for me to get to this point in my life. No words can explain my gratitude. Lastly, all my love and thanks to my gorgeous, loving and patient wife, Courtney.

---

[8] Past and present members of the MicroNanophysics Research Laboratory.

CONTENTS

LIST OF FIGURES

LIST OF TABLES

ACRONYMS

IDT	Interdigital Transducer
SAW	Surface Acoustic Wave
SW	Surface Wave

Part I

CHAPTERS

1

INTRODUCTION AND LITERATURE REVIEW

In this chapter a broad introduction to the field of microfluidics and the associated challenges in actuation are presented, followed by an overview of different actuation mechanisms classified into mechanical and non mechanical ones. A special attention is then given to acoustics, as one of the non-mechanical mechanisms that gained considerable attention of late and is the mechanism of choice for this thesis, followed by a variety of actuation examples achieved by the use of Surface Acoustic Waves (SAWs). The chapter finishes with the motivation behind the work presented in this thesis and a roadmap for the included chapters.

1.1 CHALLENGES IN MICROFLUIDICS

Actuating and manipulating fluids and particles at microscale dimensions poses a considerable challenge, primarily due to the increasing surface area to volume ratio as the characteristic system dimension is reduced, which reflects the increasing dominance of surface and viscous forces in retarding fluid flow. This is captured by the characteristically small Reynolds numbers ($\mathrm{Re} \equiv \rho U L/\mu \leq 1$) in microfluidic systems wherein ρ and μ is the density and viscosity of the fluid, and, U and L are the characteristic velocity and length scales, respectively. Laminarity of the flow is also inherent in these low Re systems, thereby highlighting further challenges with regards to fluid mixing, especially in diffusion-limited systems.

To date, external syringe pumps have been widely utilized to induce flow and mixing in microfluidic systems. Although these are precise and reliable, they are fairly large and hence confined to laboratory benchtops, thereby proving difficult to integrate with other operations on the microfluidic device to comprise a miniaturized handheld platform for portable operations, for example, for use at the point of need [223]. This is further complicated by the inlet and outlet tubing and ancillary connections required for fluid transfer between the pump and the chip, which requires careful handling by a skilled user, therefore, making their use considerably challenging for adoption by patients, for example, in diagnostic testing. The majority of medical testing also involves molecular and bioparticle manipulation, which require additional microfluidic capability for fast and sensitive preconcentration, sorting and detection.

As shown below in table. 1.1 and 1.2, we summarize the various actuation mechanisms for microfluidic actuation within two subcategories: mechanical and nonmechanical actuation mechanisms, as shown below.

Table 1.1: Summary of the main ***mechanical*** actuation mechanisms for microfluidic actuation.

Mechanism	**Principal/Notes**	**References**
Piezoelectric	A diaphragm comprising a piezoelectric disc, or a stack, that deforms when subject to an electric field to induce fluid motion by peristaltic (i.e., sequential contraction and relaxation) action along the length of the channel.	Koch et al., 1998 [96]; Schabmueller et al., 2002 [170]; and Jang et al., 2007 [85]
Pneumatic/Thermopneumatic	Air is employed to actuate and relax a diaphragm to create a pressure difference that pumps the fluid; often combined with diffusers. Thermopneumatic uses heated and cooled air.	Pol et al, 1990 [198]; Jeong et al., 2000 [86]; Kim et al., 2005 [94]and Grover et al., 2006 [69]
Rotary/Centrifugal (e.g., rotary gears, Lab-on-a-CD)	Reservoirs, valves and channels are patterned on a compact disc (CD). Fluid actuation within these structures arising from centrifugal forces is achieved upon rotation using a laboratory micromotor. A thermopneumatic addition combines this with heating of the reservoir to allow bidirectional pumping.	Gorkin et al., 2010 [66] and Abi-Samra et al., 2011 [2]
Shape-memory alloys (SMA)	Shape memory alloy (SMA) are thin films, and recently wires, are used as valves, pumps, latches and multiplexers as under electric field, they can exert a large strain on soft elastomers such as PDMS.	Benard et al., 1998 [16]; Xu et al., 2001 [214] and Vyawahare et al., 2008 [200]
Electromagnetic	Fluid actuation is achieved by applying an oscillating magnetic field with the use of magnetic elements strategically embedded in a soft polymeric structure, resulting in its vibration. This is combined with diffuser and nozzle elements close to the inlets and outlets to achieve net flow direction.	Al-Halhouli et al, 2010 [5]; and Zhou and Amirouche 2011 [225].

...(continued)

Mechanism	**Principal/Notes**	**References**
Electrostatic	Coulombic attraction force between oppositely charged plates drives the deflection of a soft membrane when an appropriate voltage is applied. The deflected membrane returns to its initial position upon relaxation of the field. The alternating deflection results in a pressure difference that, in turn, pumps the fluid.	Machauf et al., 2005 [122]; and Bau et al., 2007 [15]
Acoustic (e.g., Flexural waves, bubble streaming and surface acoustic waves (SAW))	Flexural Waves: Bulk vibration of a thin piezoelectric film that generates an acoustic field, which, in turn, causes fluid to flow (acoustic streaming).	Moroney et al., 1991 [139]; Luginbuhl et al., 1997 [118]; and Meng et al., 2000 [137]
	Bubble streaming: acoustic streaming driven via excitation of bubbles attached at strategic positions on a channel using a piezoelectric transducer. Typically used for fluid mixing and recently for particle sorting and trapping.	Ahmed et al., 2009a [3]; Ahmed et al., 2009b [4]; Wang et al., 2012 [203]; and Hashmia et al., 2012 [74]
	SAW: MHz-order frequency electromechanical surface waves that generate a direct acoustic force on particles or a momentum that generates fluid flow (acoustic streaming) for fluidic actuation and micro/nano particle and biomolecule manipulation	Friend & Yeo, 2011 [58]; and Yeo et al., 2011 [223]

Table 1.2: Summary of the main ***nonmechanical*** actuation mechanisms for microfluidic actuation.

Mechanism	**Principal/Notes**	**References**
Capillary (e.g., pressure and surface tension gradients)	Pressure gradient: flow induced by a pressure difference across an interface that drives wetting of fluids in channels or in paper-based substrates. Attractive because it offers a passive actuation mechanism without requiring active pumping.	IIchikawa et al., 2004 [82]; Gervais and Delamarche 2009 [64]and Martinez et al., 2010 [132]
	Surface tension gradient: generation of interfacial flow due to chemical (e.g., surfactant) concentration, thermal (thermocapillary),electrical (electrocapillary), or optical (optocapillary) gradients.	Darhuber and Troian, 2005 [39] and Basu and Gianchandani, 2008 [13]
Electrokinetics (e.g., electroosmosis, electrophoresis, dielectrophoresis and electrowetting) - Chang and Yeo (2010) [32]	Electroosmosis: bulk motion of aqueous solution along a fixed solid boundary due to an external electric field.	Lazar and Karger, 2002 [102]; Takamura et al., 2003 [189] and Wang et al., 2009 [203]
	Electrophoresis: use of an applied electric field to move charged particles or ions in a stationary fluid.	Wu et al., 2008 [212] and Kenyon et al., 2011 [92]
	Dielectrophoresis: motion of dielectric particles suspended in a medium due to the application of a nonuniform electric field.	Pethig, 2010 [155]and Menachery et al., 2010. [136]
	Electrowetting: control of the wettability of a drop or film through an applied electric field by the generation of a Maxwell force at the contact line or a Maxwell pressure along the interface (depending on electrode configuration).	Yeo and Chang, 2005 [219] ; Mugele and Baret, 2005 [140]; and Wheeler, 2008 [208]

...(continued)

Mechanism	**Principal/Notes**	**References**
Optics (optofluidics) (e.g., Laser microfluidic actuation, optical tweezing and, optical chromatography) - Fainman et al., (2010) [51]	Laser microfluidic actuation: the momentum carried by the incident propagating light gives rise to a radiation pressure at the fluid interface due to the difference in refractive index, resulting in interfacial deformation or even jetting. In addition, localized laser induces thermocapillary forces leading to fluid flow (see also Capillary entry).	Grigoriev, 2005 [68]; Baroud et al., 2007 [12]; Delville et al., 2009 [41] and Dixit et al., 2010 [47]
	Optical tweezers: Dielectric particles can be trapped and moved due to the optical gradient within the tightly focused leaser beam. Alternatively, birefringence can be exploited in which a particle can be rotated in a standard optical trap simply by manipulating the polarization of the light beam.	Grier, 1997 [68]; Dholakia et al., 2002 [43], Chiou et al., 2005 [34]and Neale, 2005 [143]
	Optical chromatography: Use of a focused laser beam to trap particles along its axis of propagation, where the beam is positioned against the fluid flow and the particles trapped location is a balance between fluid drag and optical pressure.	Hart and Terray, 2003 [71] and Hart et al., 2007 [72]
Magnetohydrodynamic	Use of a Lorentz force to pump conducting fluids, perpendicular to both the electric and the magnetic field.	Lemoff and Lee, 2000 [104]; Jang and Lee 2000 [84]; Bau et al., 2001 [15] and Eijel et al., 2003 [50]
Microbubbles	Generated either electrochemically (e.g., via electrolysis) or thermally (e.g., cavitation). The bubble oscillation is used to drive pumping in microchannels, often by pushing on diaphragms.	Suzuki and Yoneyama 2002 [188]; Yoshimi et al., 2004 [180]; Yin and Prosperetti 2005 [224]

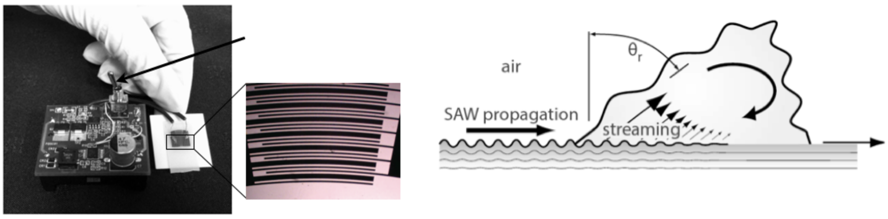

Figure 1.1: A typical SAW device comprising a piezoelectric substrate on which IDT electrodes are patterned (as shown in the enlarged inset) and a portable battery-operated electronic circuit and power supply. The black arrow points at the On/Off switch to drive the circuit. (b) Schematic depiction of the Eckart streaming generated when energy leaks into a drop at the Rayleigh angle θ_R when it is irradiated by SAWs propagating along the underlying substrate.

A technology that has attracted considerable traction of late is the use of surface acoustic waves (SAWs). Since the piezoelectric substrate required could comprise the microfluidic chip itself and as the interdigital transducer Interdigital Transducers (IDTs) electrodes required to generate the SAW can be integrated on the substrate, there is no need for the large transducers typically used in conventional ultrasonic microfluidics. Moreover, it has been shown that the ability to access high (MHz order and above) frequencies significantly avoids the amount of molecular damage caused. One further advantage is the typically low powers (1 W) required to drive fluid and particle actuation with SAWs, even to the point of fluid atomization, therefore allowing the entire operation to be driven using a portable driver circuit that is driven by camera batteries, which, together with the chip-scale substrate (Fig. 1.1(a)), potentially allows for complete miniaturization and integration into a truly handheld and portable microfluidic device. Here, we briefly discuss the basic principles underlying acoustic fluid and particle actuations and review the developments in the field to date, particularly focusing on the SAW technology.

1.2 BASIC PRINCIPLES OF ACOUSTIC FLUID AND PARTICLE MANIPULATION

A sound wave is the result of pressure or velocity oscillations that propagate through a compressible medium, and can be generated through bulk or surface vibrations of solid materials. A convenient way to produce such vibration, especially at small scales in microfluidic systems, is with the use of oscillation electric fields by exploiting the electromechanical coupling afforded by piezoelectric transducers or substrates. There are primarily two broad strategies employed for acoustic particle and fluid actuation, which we describe next.

The first, generally known as acoustophoresis, exploits standing acoustic waves set up in a resonator configuration to spatially trap and move cells. The fundamental basis of the particle localisation at pressure nodes/antinodes of the standing wave and hence the ability to carry out particle separation arises from a competition between the dominant forces acting on the particle (assuming that sedimentation and buoyancy forces are negligible), namely, the primary acoustic radiation force

$$F_a = -kE_aV_p\phi(\beta,\rho)sin(2kx), \tag{1.1}$$

assuming a one-dimensional planar standing wave, and the drag force

$$F_d = -6\pi\mu ua \tag{1.2}$$

acting on the particle of dimension a and volume V_p, in which x is the distance from a pressure node along the wave propagation axis. In the above, $k = 2\pi f/c_l$ is the wave number, with f denoting the applied frequency and c_l the sound speed in the fluid medium, $E_a = P_0^2\beta_l/4 = P_0^2/4K_l = P_0^2/4\rho_l c_l^2$ the acoustic energy density of the standing wave, with P_0 being the pressure amplitude of the standing wave, β_l the liquid compressibility, K_l the bulk modulus and ρ_l the liquid density, and,

$$\phi = \frac{5\rho_p - 2\rho_l}{2\rho_p + \rho_l} - \frac{\beta_P}{\beta_l} \tag{1.3}$$

is an acoustic contrast factor in which ρ_p and β_p is the particle density and compressibility, respectively. Particles therefore aggregate at the pressure nodes for $\phi > 0$ and at the antinodes for $\phi < 0$.

The second exploits the fluid flow that results as the acoustic wave propagates through a fluid, known as acoustic streaming [58]. Different acoustic streaming phenomena are observed to occur over a variety of length scales imposed by the system geometry. In a thin boundary layer of fluid immediately adjacent to the vibrating surface with a characteristic thickness defined by the viscous penetration depth $(2v/\omega)^{1/2}$ strong viscous dissipation of the acoustic wave gives rise to flow known as Schlichting streaming [172] that is vortical in nature due to the no-slip condition at the oscillating solid boundary; v is the kinematic viscosity and ω the angular frequency. At the edge of the boundary layer (also known as the Stokes layer) over a length scale on the order of the sound wavelength in the liquid λ_L (which, in turn, is related to the excitation frequency), a steady irrotational drift flow, known as Rayleigh streaming, occurs as a consequence of the periodic recirculation in the boundary layer. Over longer length scales $>> \lambda_L$, the viscous dissipation of the acoustic radiation due to absorption in the fluid whose pressure and velocity fluctuations give rise to a time-averaged particle displacement and hence steady momentum flux (i.e., Reynolds stress) that is non-zero despite the harmonic oscillation due to the nonlinear effects arising from viscous attenuation of the wave [112]; the resultant flow being known as Eckart streaming [49]. It is not uncommon that a combination or all of the various streaming phenomena exists together in a system, although one particular mechanism typically dominates contingent upon the system geometry.

1.3 SURFACE ACOUSTIC WAVES (SAWS)

Nanometer amplitude surface vibrations on a substrate in the form of Rayleigh waves offer an attractive and arguably superior alternative for microfluidic actuation compared to bulk ultrasound. The energy localization of these SAWs on the substrate and their efficient coupling into the fluid allows fluid actuation to be carried out with significantly lower dispersive losses, and hence the power requirement to drive comparable fluid actuation to that generated by bulk acoustics is significantly less, by one to two orders of magnitude, therefore offering possibility for the battery-powered operation, which, together with the chip-scale SAW device in Figure 1.1(a), enables attractive miniaturization possibilities [222]. Further, the low powers, together with the higher frequencies accessible with the SAWs, 10 MHz and above, has been found to suppress shear or cavitation damage on molecules[158] thus making them attractive for bioapplications.

The SAW can be generated on a piezoelectric substrate by applying a sinusoidal electrical signal to interdigital transducer (IDT) electrodes patterned on the substrate whose finger width d determines the frequency f of the SAW and hence its wavelength λ_{SAW}, i.e., $f = c_s/4d = c_s/\lambda_{SAW}$. As illustrated in Figure 1.1(b), the coupling of acoustic energy into the fluid to drive Eckart streaming then arises from the diffraction of the SAW front in the presence of the fluid which leads to leakage of the energy into the fluid at the Rayleigh angle, defined as the ratio between the sound speed of the Rayleigh wave on the substrate c_s to the speed of sound in the fluid c_l, i.e., $\theta_R = sin^{-1}(c_s/c_l)$. In addition to the recirculation within the fluid, the acoustic radiation pressure also imparts a force at the interface, that together with the momentum transfer to the interface due to

Eckart streaming, imparts a body force on the drop whose horizontal component causes it to translate in the direction of the SAW. In the same way that ultrasonic standing waves and acoustic streaming can be exploited to drive microscale fluid actuation and particle manipulation, we provide a short discussion of the use of SAWs for this purpose and their associated applications. For a more detailed discussion on SAW microfluidics, see, for example, [58].

1.4 SAW PARTICLE MANIPULATION

Acoustophoretic manipulation can also be carried out using standing SAWs in a similar manner to bulk ultrasonic standing waves. The standing wave, in the SAW devices, however, arises when diffraction of the SAW from the substrate into the liquid (Fig. 1.1(b)) generates sound waves in the liquid bulk that reflects off the walls of the microchannel (often fabricated from polydimethlysiloxane (PDMS) and placed atop the SAW substrate). Depending on the channel dimension and the sound wavelength in the fluid, the particles then aggregate along one or more pressure nodal (or antinodal) lines along the channel. Conventionally, the IDTs are placed perpendicular to the channel and hence flow direction [177], to achieve linear focusing and subsequent separation/sorting, for example, by size, compressibility or density [141]. In addition, the IDTs can also be arranged orthogonally at two lateral sides of a square chamber to obtain two-dimensional patterning [178]. A discussion on the use of these devices as 'acoustic tweezers' for cell manipulation is give in [114].

In addition, the nodal and hence particle positions can also be shifted along the axis of the standing wave by shifting the relative phase between the input IDT signal [138, 149]. Particle alignment and sorting can also be carried out using using IDTs placed at the ends of the channel such that the SAW propagates along the channel axis [193]. One advantage of this configuration is the ability to alter between fluid pumping and particle focusing simply by switching the frequency from the fundamental mode to a higher harmonic [195].

1.5 SAW FLUID ACTUATION AND MANIPULATION

SAW particle aggregation, trapping, patterning and separation is typically carried out at low input powers, considerably below 1 W, where the SAW displacement amplitude and velocity are relatively small, on the order of 0.1 nm and 0.01 m/s, respectively, such that the streaming is weak in order to avoid dispersion of the particles. At these low powers, other particle patterning phenomena are also

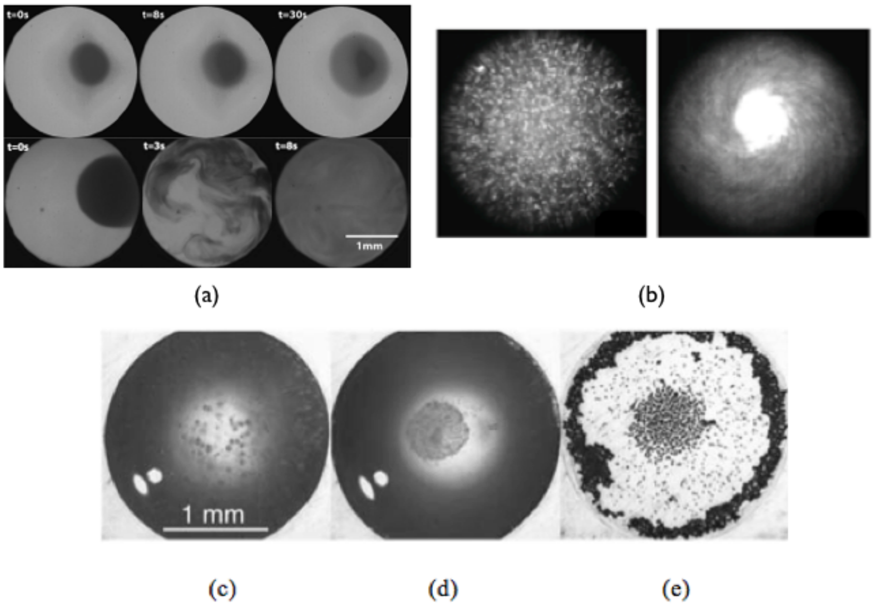

Figure 1.2: (a) The images in the top row show mixing of a dye due to pure diffusion without the action of the SAW, whereas the images in the bottom rows show effective mixing under chaotic flow conditions driven by the SAW with an input power of 1 W. (Source: Shilton et al. (2011).) (b) Concentration of particles in a 0.5 /*mu*L drop via drop rotation induced by acoustic radiation due to SAW. (Source: Shilton et al. (2008).) (c) - (e) Separation of pollen and synthetic particles. (Source: Rogers et al. (2010).) (c) Prior to the application of the SAW, the pollen and synthetic particles were suspended homogeneously throughout the entire quiescent drop. (d) 3 s of applying the SAW, the pollen particles appear to concentrate in the centre of the drop and are hence separated from the synthetic particles, which tend to concentrate along the periphery of the drop. (e) The two species remain separated even after removal of the SAW and when the drop is fully evaporated after 1 min.

observed, for example, those that form on the nodes or antinodes of capillary waves induced on the free surface of drops vibrated by the SAW excitation [109].

At moderate power levels (approximately up to 1 W), it is possible to dispense and transport drops [160]. For example, sessile drops can be translated on the substrate when the acoustic radiation pressure and acoustic streaming results is sufficient to impart momentum transfer to the interface to overcome the pinning of the contact line [28]. This was shown for a variety of applications in open microfluidic systems such as polymerase chain reactions (Wixforth et al., 2004) [211], bioparticle sampling, collection and concentration [191] scaffold cell seeding [107] and protein unfolding [174]. In addition, the SAW has also been combined with electrowetting to enhance drop manipulation operations such as splitting [106].

At these powers, the SAW can also be used to drive strong convective flows both within the drop and in channels. For example, it is possible to break the planar symmetry of the SAW to drive azimuthal recirculation in a drop or a microfluidic chamber to generate a rapid microcentrifugation effect [179]. This was used for example for inducing rapid and chaotic mixing (Fig. 1.2(a)) which can be used to enhance chemical and biochemical reactions [98, 99], or for particle concentration/separation (Fig. 1.2(b)). It is also possible to sort two particle species based on size in this microcentrifugation flow by exploiting the discrepancy in the scaling between the acoustic radiation force and the drag force exerted on the particle (Eqs. 1.1 and 1.2): from a balance between these two forces, it is then possible to derive a frequency-dependent crossover particle size below which the drag force dominates to drive smaller particles to the center of the drop and above which the acoustic force dominates to drive larger particles to the periphery (Fig. 1.2(c)) [169]. Finally, the drop rotation can also be used to spin 100 μm to 10 mm thin SU-8 discs on which microfluidic channels and chambers can be patterned, as a miniaturized counterpart to the Lab-on-a-CD [123] for centrifugal microfluidic operations; unlike the Lab-on-a-CD, however, the SAW miniaturized Lab-on-a-Disc (miniLOAD) platform does not require a laboratory bench-scale motor given that the SAW can be driven using a portable driver circuit (Fig. 1.1(a)), therefore constituting a completely handheld microfluidic platform (Fig. 1.3) [65].

SAW streaming has been demonstrated for fluid actuation in PDMS channels placed atop the substrate [134], in channels ablated into the SAW substrate [193] and even on paper [163] In addition, it was also shown that the SAW can be used to deflect the interfaces of co-flowing streams for directing emulsion droplets [56] and sorting cells [57]. Whilst the body of earlier work was carried out in open microchannels, which have severe limitations due to evaporation and possible contamination, recent work has focused on fluid actuation in a closed PDMS microchannel loop [174] although the efficiency of the pump remained modest as a consequence of the strong absorption of the acoustic energy by the PDMS channel placed atop the SAW substrate. A way to circumvent this limitation was proposed in [100], in which a glass superstrate housing the microchannel was directly bonded to the SAW substrate using a UV epoxy; alternatively a SU-8 glue layer can also be used [89]. Importantly, it was shown that the SAW is retained at the interface between the substrate and superstrate. This is in contrast to previous uses of a superstrate, first proposed in [80], in which a fluid layer between the SAW substrate and the superstrate was employed to couple the acoustic energy into the latter, resulting in a Lamb wave on the superstrate. Nevertheless, it was shown, that it is possible to achieve similar fluid actuation and particle manipulation on the superstrate through Lamb wave excitation, albeit at considerably lower efficiency. Regardless, the use of a superstrate remains attractive since the microfluidic operations can be carried out in conventional silicon-based materials, which are considerably cheaper, thus allowing the option of disposability. It was later showed in [25] that it is possible to pattern periodic arrays of holes or posts in the superstrate to form a phononic crystal lattice that acts as a bandgap to drive similar azimuthal recirculation to that discussed for a drop above, or to filter, scatter, reflect or focus the Lamb wave. This was employed for the development of a biosensor platform for the concentration of beads labelled with antibodies onto surface sites for subsequent binding and fluorescent detection [25].

At higher powers above 1 W, it is possible to drive sufficient interfacial deformation of a film or a drop to extrude fluid jets [192, 20] or to drive atomization [156]. Given that a monodispersed distribution of 1 - 10 μm aerosol droplets can be formed in the latter without requiring nozzles or orifices, the latter is particularly useful for pulmonary drug delivery [157], especially the next generation of therapeutic agents such as DNA, peptides and proteins, in a miniaturized portable platform for point-of-care therapeutics and personalized medicine. A significant advantage of the SAW pulmonary delivery platform over conventional nebulizers is the ability to preserve the viability of the drug, particularly shear-sensitive molecules such as DNA and peptides. In addition to drug delivery, the SAW atomization platform has been shown to be an efficient ionization source for microfluidic mass spectrometry interfacing [76, 77]. The atomization of polymer solutions using the SAW is also a rapid technique for template-free polymer patterning for microarray applications [6] as well as for synthesizing 100 nm dimension protein and polymer nanoparticles [59, 7] within which drugs can be encapsulated[8]. This was more recently extended to synthesize nanocapsules of complementary polyelectrolyte layers for DNA encapsulation, as an example of tunable controlled release delivery [159].

1.6 LIMITATIONS AND MOTIVATION FOR THIS THESIS

Although a wide variety of SAW-driven applications have been demonstrated in the last few years, as alluded to above, a deep understanding of the physics governing the dynamics of films driven by SAW is not clear. This is due to the complexity and non-linearity of the waves upon interaction with the fluids with the added complexity of using high frequency vibrations - 10 MHz and beyond - which is extremely

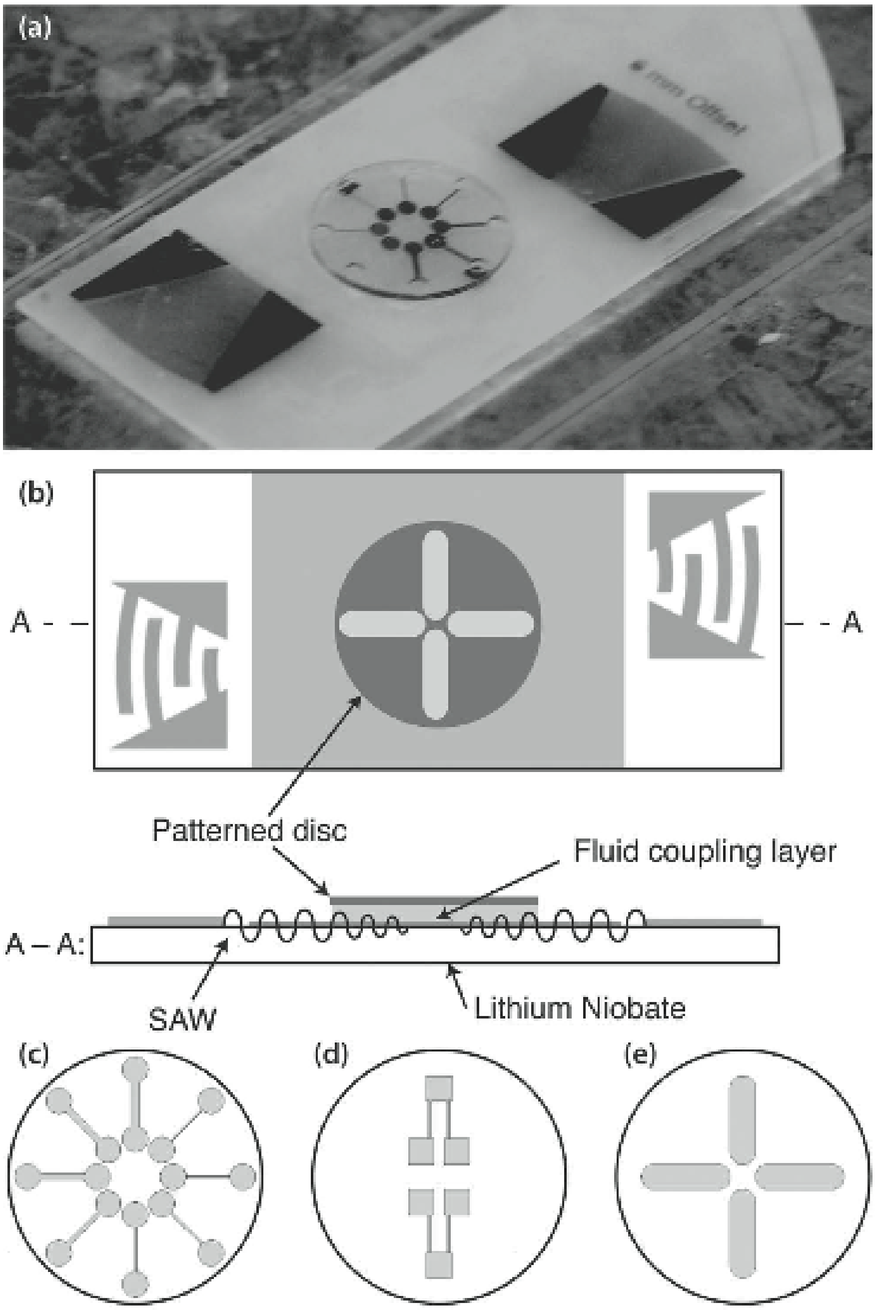

Figure 1.3: (a) Image and (b) schematic depiction of the miniLOAD platform comprising a 10 mm diameter SU-8 disc on which microchannels with a variety of designs ((c) - (e)) are fabricated to demonstrate capillary valving, micromixing and particle concentration/separation on a miniaturized centrifugal platform.The disc rotation is driven by coupling an asymmetric pair of SAWs into the fluid underneath the disc. (Source: Glass et al. (2012).

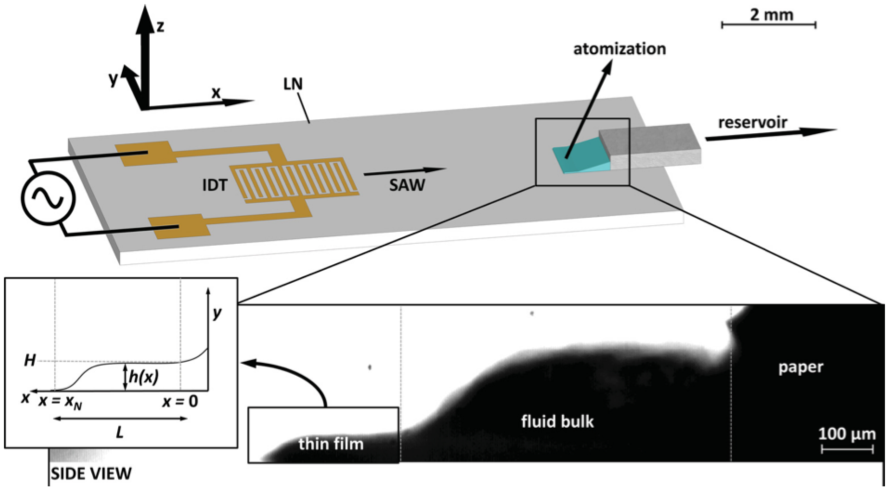

Figure 1.4: Schematic illustration of the SAW atomization device setup. The liquid to be atomized was supplied from a reservoir (not shown) through a paper wick. As illustrated by the expanded inset image, the SAW drew out a meniscus from the paper, comprising a thin advancing film and a bulk region, both of which are characterized by different length scales, capillary frequencies, and resultant droplet sizes. The majority of the atomized droplets, however, originated from the thin film region with characteristic height and length scales denoted by H and L, respectively, both of which are small compared to the width of the film, which, in turn, is set by the width of the paper wick. Source: David et al. 2012 [36].

far from the typical natural resonances of liquids at the Hz and KHz range.

However, we do believe that, a thorough understanding of the interactions of SAW with fluids will not only enrich our understanding of these fascinating systems from a physical point of view, which we shall explore in chapter 2, but will also open the door for more controlled practical applications, especially for neubilisation. One example of practical applications is shown in chapter 3, where SAW is used to drive reliable and fast mixing in paper-based microfluidic channels.

One example of a recent work in [36] were SAW-driven thin films where investigated from atomisation behaviour and drop size distribution point of view, where the set up, as shown in figure 1.4, consisted of a wet paper in contact with the lithium nioabte substrate. The authors gave a qualitative picture, shown in figure 1.5, of the transient response of the water in the paper to the propagating SAW. The complex transient dynamics, starting from a water meniscus in figure 1.5(a), when the SAW was off to a bulk recirculation in figure 1.5(b), immediately after SAW was on, followed by a bulk pullback of the majority of the fluid in figure 1.5(c) and finally an oscillating thin film, from which atomisation took place in figure 1.5(d). The interesting highlight of this work is that the dimensions and aspect ratio of this

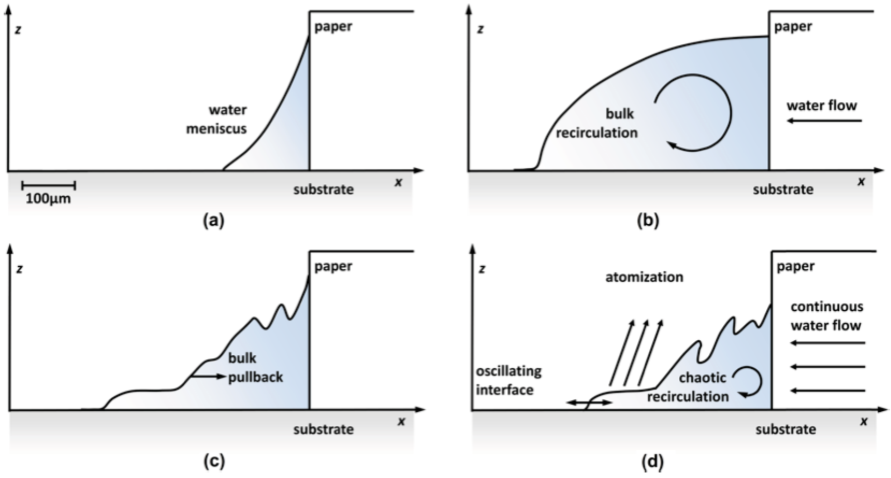

Figure 1.5: (a) At rest and prior to SAW actuation, a liquid meniscus formed between the wetted paper and the LN substrate. (b) Application of the SAW results in the pullout of a liquid bulk with height and length scales several times the liquid wavelength λ_l. (c) After 50 - 500 ms, the leading edge of the liquid bulk was observed to retreat, (d) leaving behind a thin film region from which atomization occurred. The film and chaotic bulk liquid regions interacted dynamically, with the film moving horizontally and occasionally being obscured completely by the bulk region. Source: David et al. 2012 [36].

thin film dedicates the atomised drop size. Since the ejected drop size value and distribution is crucial for many applications, a closer look and deeper understanding of these films can indeed warrant a more controlled atomisation. Therefore, using oil films, to circumvent evaporation, and using input powers below that it is required for atomisation, we show in chapter 2 a thorough systematic experimental procedure of a variety of film thicknesses driven by SAW, and with the aid of robust mathematical derivation and numerical analysis we unlocked the physics governing these thin films and unravel two new fluid dynamics phenomena; SAW diffraction driven fingering instabilities and soliton-like wave emergence and propagation, a unique fluid flow phenomenon with no precedent in microfluidics.

In addition, although a lab-type prototype incorporating SAW with microfluidics can be shown to drive a range of microfluidics applications, a practical issue for development and commercialisation is the cost and complexity of use by non-skilled users, which constitutes a huge hurdle for these prototypes to make their way to the market. Therefore, we shall show in chapter 4 that, contrary to the status quo adopted by many scientists across the world, bulk waves vibrations and more specifically Lamb waves, are shown to drive a reasonable range of microfluidic applications with a small fraction of cost required for fabrication of IDT for SAWs generation, as the Lamb wave design does not require any cleanroom fabrication. Furthermore, we show that these devices are superior to SAWs in terms of power consumption as well as atomised drop size and distribution.

A road map for the remainder of this thesis will now be provided.

1.7 THESIS OUTLINE

Chapter 2: ACOUSTOWETTING: THE STUDY OF FILM ACTUATION UNDER SAW AND OTHER PECULIAR PHENOMENA

In chapter 2 we report a comprehensive study of thin films actuation driven by SAW using elaborate experiments, analysis, rigourous mathematical derivations as well as numerical modelling. The study has revealed the competing role of the interplay between capillary, acoustic, and intermolecular forces, surface acoustic waves (SAWs) drive a fascinating emph flow reversal phenomenon in the spreading of thin films. Other novel phenomenon were observed and elucidated including unique fingering instabilities due to SAW diffraction as well as the formation and propagation of soliton-like waves.

Chapter 3: FLUID PUMPING AND MIXING ON PAPER-BASED MICROFLUIDICS DRIVEN BY SAW

Beyond elucidating the underlying physics governing SAW-driven thin films, in chapter Chapter 3, we designed and conducted experiments comprising the integration of the SAW with Y-shaped microchannels patterned on wet paper susbtrate, where a thin film at the paper's tip was drawn out using SAW atomisation, which, consequently, led to driving the rest of the fluids at the channel's other ends, thus, leading to fast and repeatable fluid mixing along the michrochannels. Mixing was compared for SAW atomisation assisted pumping method versus typical capillary driven mixing. The former has shown to offer more control on the flow rate and is capable of performing faster, more uniform and reliable mixing, irrespective of the paper surface roughness. The mixing process was quantified using a novel technique based on *hue*, offering more practical and broader use, especially when the fluids used have similar colour contrast, compared to the commonly used greyscale method.

Chapter 4: BULK ACOUSTICS: SIMPLER AND CHEAPER ACTUATION SETUP AND OTHER PECUILAR FLOWS

In chapter 4 noting from chapter 3 that although a laboratory prototype is indeed possible to demonstrate the functionally of SAW driven microfluidics, a significant hurdle for practical use is the cost and complexity of the patterned IDTs. Here, we exploited the use of simpler designs and thus selected bulk waves, especially Lamb waves, a more practical solution from a cost and simplicity of use point of view. Very simple electrode deposition techniques where used, such as direct ink transfer from paper onto lithium niobate using a laminator, where the ink acts as a shadow mask or even in some cases aluminium foil — available in any kitchen — was cut into small pieces and brought into contact with the piezoelectric surface. These simple setups have shown a tremendous potential for use in a variety of microfluidic applications such as particle patterning, concentration, drop translation and mixing and more importantly, atomisation. A monodispersed mist, with dimensions even smaller than achieved by SAW, were produced, rendering the applicability of these simple systems for many applications including drug delivery by inhalation. In addition to this, a novel poloidal flow phenomena for microparticles circulating within a water drop was also discovered when frequencies $\sim$ 100 MHz and beyond were used.

Chapter 5: CONCLUSIONS AND FUTURE WORK

In the final chapter an overview of the work conducted in the thesis will be provided with a list of the key contributions made. The chapter and thesis will conclude with possible future work.

2

ACOUSTOWETTING: THE STUDY OF FILM ACTUATION UNDER SAW AND OTHER PECULIAR PHENOMENA

As alluded to earlier in chapter 1, since thin film dynamics and dimensions driven by SAW control the atomised drop size and rate, thorough understanding of these thin films can indeed guide more controlled experiments for the atomisation process. This chapter elucidates the mechanisms behind the dynamics of thin films upon the interaction with SAWs, for input powers below the ones required for atomisation to facilitate an accurate study and revealing double flow reversal behaviour for different film thicknesses. Ultra-thin films $\sim$ 1 µm were observed to move along the SAW propagation direction, while intermediate (also named thin films in this thesis) films $\sim$ 10 µm were observed to move counter to the SAW propagation direction. However, thicker films or drops were observed to reverse direction, again, and move along the SAW propagation direction. In addition to this, thin films were observed to develop a unique fingering instabilities due to the SAW diffraction. Furthermore, solition-like waves, on a microfluidic scale, were observed for first time, to develop and propagate in a SAW-driven system. All these fascinating observations, together with a thorough mathematical derivation has led to a remarkable understanding to this variety of discoveries and is evident in the publication of parts of this work in Nature Communications*, as well as two other manuscripts one currently under review and the other about to be submitted. The thorough understanding of the dominance of relevant streaming at different length scales, could guide further applications for the SAW microfluidics, as will be shown later in chapter 3*

2.1 INTRODUCTION

High frequency vibration in solids, assuming the form of acoustic waves with frequencies in a range of 10–300 MHz were recently found to be capable of driving novel drop and film wetting dynamics [156, 6, 194, 126, 36, 162, 164] distinct from that excited by their lower frequency counterparts [21, 175, 145, 9, 38, 18, 121, 24, 26, 52, 27]. In low frequency studies, usually at frequencies comparable to the natural oscillation frequency of the liquid body ($\sim$ 10 Hz–10 kHz), the liquid generally responds through the generation of a predominantly convective (potential) flow in the bulk [184, 210]. This leads to shape oscillations of the liquid body modulated by the restoring force imposed by its surface tension, which leads to the generation of subharmonic (and also superharmonic) capillary waves via parametric excitation [17, 215], manifesting as patterns on the free surface of liquid films [21, 175, 145, 146, 18]. In addition, the shape oscillations can cause displacement of the three-phase contact line in sessile drops that, in turn, results in a change in the contact angle beyond its hysteresis range, rendering periodic stick-slip contact line motion [48, 79, 78, 52] and enabling drop translation [38, 26, 27].

Such vibrational excitation also invokes a viscous-dominant periodic vortical flow field in a thin region adjacent to the surface with a thickness characterised by a viscous penetration length $\beta^{-1} = (2\mu/\rho\omega)^{1/2}$, where μ and ρ denote the liquid viscosity and density, respectively, and ω the angular frequency of excitation; for water, $\beta^{-1} \approx 10$–$100\ \mu$m in the low frequency excitation range, suggesting that the effective thickness of the viscous boundary layer, whilst large with respect to the characteristic submicron length scales over which capillary and molecular forces shape the three-phase contact line region [40], is typically small compared to the dimension of the liquid body that is excited, typically on the order of millimetres. This periodic boundary layer flow, first examined by Stokes for simple in-plane periodic substrate motion (see, for example, Batchelor [14]), was subsequently extended by Schlichting (hence the flow being commonly referred to as Schlichting boundary layer flow or Schlichting streaming) and others to account for more complicated forms of excitation [172, 147, 117, 81, 165, 186, 176, 166, 167, 168, 173, 207, 201], and, recently, to allow for generalised two-dimensional substrate excitation in the form of Surface Wave (SW) that propagate on a solid surface [127].

Whilst high frequency vibrational excitation has received considerable attention of late due to its utility for manipulating flow at microscale and nanoscale dimensions for a variety of microfluidic applications [222, 58, 114], little is yet understood concerning the mechanisms describing how such vibration influences the dynamics of liquid drops and thin films. The distinct behaviour observed in high frequency vibrational excitation appears to arise primarily due to the dominance of the same viscous-dominant periodic flow, but which at high frequencies above 1–10 MHz, is confined within a region whose thickness $\sim \beta^{-1}$ is typically below 1 μm. Thus, in contrast to low frequency substrate excitation, β^{-1} is now becomes of the same order as the long-range molecular interactions between the solid and the liquid associated with the contact line region and therefore could potentially influence the dynamics of the contact line to a considerable extent.

This was first realised for sessile water drops on slightly hydrophilic substrates excited by bulk pistonlike vibration [126]. Owing to the relatively large contact angles (at least, initially, prior to the drop spreading under the influence of the applied vibration), the viscous boundary layer flow in the vicinity of the contact line was assumed to be spatially unbounded to leading order, i.e., $h \to \infty$. The net momentum associated with the exponentially-decaying (in height away from the substrate) periodic viscous flow field in the boundary layer then yields a steady Reynolds stress at the interface, which was shown to be localised within a small region at the contact line given that β^{-1} is asymptotically small compared to the drop height h. Consequently, the interfacial stress averaged over this region yields an equivalent point force F at the contact line that modifies the equilibrium contact angle of the sessile drop. Importantly, we note that $F \sim 1/\beta^{-1}$ such that the higher the applied frequency and thus the smaller the viscous penetration length, the greater the influence of the substrate vibration on the contact angle and hence the spreading of the drop. Similar inverse dependence on the viscous penetration length was consistently observed in other high frequency vibration systems independent the nature of the vibration or the liquid geometry employed, for example, where Rayleigh surface acoustic waves (SAWs) were used in place of the bulk pistonlike vibration in which it was observed that water menisci could be drawn out from paper-based substrates [36].

The same dependence is also obtained for the spreading of thin films comprising low surface tension liquids such as silicone oil where the liquid forms small contact angles with the solid substrate. However, in this case of spreading on high surface energy substrates wherein the film thickness h becomes comparable to β^{-1} in the contact line region owing to the small contact angles, the viscous-dominant periodic flow field generated in the film is no longer strictly a boundary layer flow due to the enclosing free liquid boundary, i.e., the flow is now spatially-bounded. Further, since β^{-1} is no longer asymptotically small compared to h, the net momentum arising from the viscous-dominant periodic vortical flow excited by the substrate vibration can no longer be coarse-grained to produce a microscopic point force at the contact line; instead we will show below that the slender film geometry allows for an asymptotic solution of the flow field to produce a steady convective drift within the liquid film, akin to the Stokes drift [173], that drives the film to spread.

Interestingly, under Rayleigh SAW excitation, these oil films exhibit a curious thickness-dependent double flow reversal phenomenon.

Thin submicron and micron order ultra-thin films that initially spread *along* the propagation direction of the SAW were observed to reverse their direction above a critical film thickness $\mathcal{H}_{c_1}$ such that films of intermediate thickness, called thin films in this thesis, and typically several microns to tens of microns in thickness, spread in the direction *opposing* that of the SAW propagation (Fig. 2.1(a)). Increasing the film thickness further beyond a second critical value $\mathcal{H}_{c_2} \sim \lambda_l$, however, triggered a second flow reversal where submillimetre thick films and sessile drops were observed to translate again *along* the SAW propagation direction (Fig. 2.1(b)) [162, 164].

As an aside, we note that both observations for the high frequency vibration-induced spreading of sessile water drops and thin oil films above are analogous to electrowetting—wetting phenomena under the influence of electric fields. The former is not unlike the equilibrium contact angle change due to a singular point Maxwell force at the contact line described by the Lippmann condition in static electrowetting, and the latter akin to spontaneous electrowetting films arising from the negative Maxwell pressure gradient imparted along the free surface of the liquid film [219, 220]. Unifying these observations across both *bulk* pistonlike and *surface* wave (e.g., Rayleigh SAW) vibrations is the existence of an intense viscous-dominant periodic flow field, constrained in a thin layer whose thickness β^{-1} in the high frequency regime is sufficiently small, typically submicron in dimension, such that the momentum transferred from the vibrating surface into this viscous penetration layer is concentrated in the vicinity of the three-phase contact line, thus generating a sufficient localised stress or convective drift that renders the liquid to spread.

In this chapter, we begin by demonstrating the experimental setup in §2.2, followed by a unified theory that universally describes the dynamic spreading behaviour of liquid films atop high surface energy substrates excited by high frequency vibration in the form of generalised travelling SWs, which include, but are not merely limited to Rayleigh SAWs. We begin in §2.3 by formulating the equations governing the conservation of mass and momentum subject to the relevant boundary conditions for the vibrating substrate and the free surface of the film to derive a generalised film spreading equation that describes the spatiotemporal evolution of the film. This is then simplified in §2.4 to first analyse ultra-thin films whose thicknesses are comparable to β^{-1}, from which we show that the ultra-thin film spreads along the direction of the convective drift that arises, which is in the same direction as the SW excitation that produces it. Subsequently, we examine the role of the acoustic radiation pressure to investigate the film stability in §2.5, wherein we observe that the thin films which are

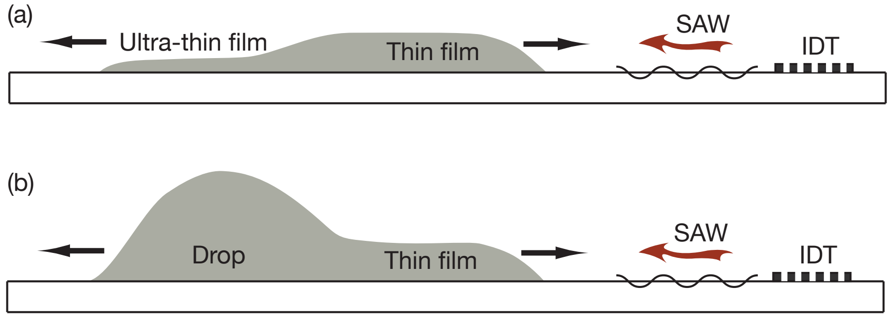

Figure 2.1: Schematic illustration of the spreading observed for liquids on high surface energy substrates vibrating at high frequencies under Rayleigh SAW excitation. (a) Thin submicron films spread along the propagation direction of the SAW whereas films of intermediate thicknesses spread in the other direction, opposing that of the SAW propagation. (b) Sessile drops (or thick submillimetre films), on the other hand, advance along the SAW propagation direction. Note the different behaviour in both cases is due to the amount of fluid displaced on the surface, in case of (a) only a thin film was deposited while in (b) a sessile drop was placed on the surface. The wetting properties were identical for both cases.

stable at sufficiently small thicknesses become periodically unstable at larger thicknesses. For stable films of intermediate thicknesses, the description for their spreading in §2.6 is observed to produce a reversal in the spreading direction such that they propagate in a direction that opposes the drift and hence the SW propagation direction. The film interface subsequently suffers a unique instability, akin in appearance to viscous fingering, due to the SAW diffraction as explored in §2.7. As the films grow further in thickness, Eckart streaming—the bulk long-range vortical flow that arises from the viscous attenuation of the acoustic wave generated in the liquid upon leakage of the SW energy from the substrate into the liquid [49, 147, 111]—becomes appreciable to drive film/drop translation in the SW propagation direction, as explored in §2.8 and followed by a unique example and threshold for the dominance of Eckart flow in the appearance and translation of soliton-like wave pulse as shown in §2.9. This is followed by concluding remarks in §2.10.

2.2 EXPERIMENTAL PROCEDURE FOR DOUBLE FLOW REVERSAL

The substrate material consisted of a 0.5-mm-thick 127.68° Y-rotated, X-propagating lithium niobate single crystal piezoelectric wafer (Roditi Ltd., London, UK), diced into 18 × 12 mm chip-scale devices, on which interdigitated transducers (IDTs) comprising 42 straight interleaved electrode pairs of 175 nm gold and 5 nm chromium layers were patterned using standard photolithography techniques and a photo of the chip is shown in Fig. 2.2(a). The SAW is then generated by applying an

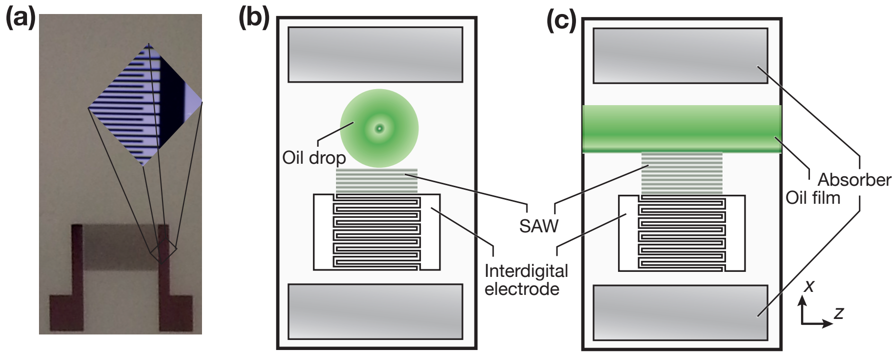

Figure 2.2: (a) Image of the SAW device used in the film spreading experiments that comprises a lithium niobate substrate on which IDT finger electrode pairs (magnified in the inset) are patterned. Also shown are schematics illustrating the placement of (b) an oil film of predetermined initial thickness, and, (c) a 3 $\mu\ell$ sessile oil drop, prior to application of the substrate vibrational excitation, i.e., the SAW.

AC electrical signal between 9–24 V using a signal generator (Rhode & Schwarz SML01, North Ryde, NSW, Australia) and amplifier (Amplifier Research 10W1000C, Souderton, PA, USA) to the IDTs at a frequency associated with the resonant frequency of the IDTs, as determined by the sound speed of the SAW in the substrate and its wavelength, i.e., $\lambda_{\text{SAW}} = 4w$, where w denotes the width of the finger electrodes as well as the gap between them. Here, the SAW frequencies used are 50, 32.7, 19.5, or 15.3 MHz. The SAW that was generated was characterised using a combination of digital oscilloscopes (Tektronix TDS4012B, Beaverton, OR, USA) and current and voltage probes for measurement of the electrical input power, together with a laser Doppler vibrometer (Polytec GmBH UHF 120, Waldbronn, Germany) to visualise the waves as well as to measure the surface displacement amplitudes U in (4.1). Absorbent gel (Geltec Ltd., Tokyo, Japan) was placed around the edges of the device to minimise wave reflections. The working fluid in the experiments consisted of silicone oil (Sigma-Aldrich Pty. Ltd., North Ryde, NSW, Australia) with viscosity $\mu =$50,100 and 500 mPa·s, density $\rho =$1000 kg/m^3 and surface tension $\gamma =$0.021 N/m at 25ºC.

The first set of experiments involved the use of a 3$\mu\ell$ sessile oil drop (as shown in Fig. 2.2(b) and Fig. 2.3) was pipetted onto the lithium niobate surface, where intermediate (also named 'thin' in this thesis) counter-propgating films were explored in detail [162].

The silicone oil drop experiments were followed by a thorough study of different film thickness using a thin oil strip of predetermined thickness was 'written' across the lithium niobate surface using a 0.5-mm-wide polyethylene strip dipped in a reservoir filled with oil and subsequently clamped onto a moving stage whose translation speed determined the resulting film thickness. The later set of experiments

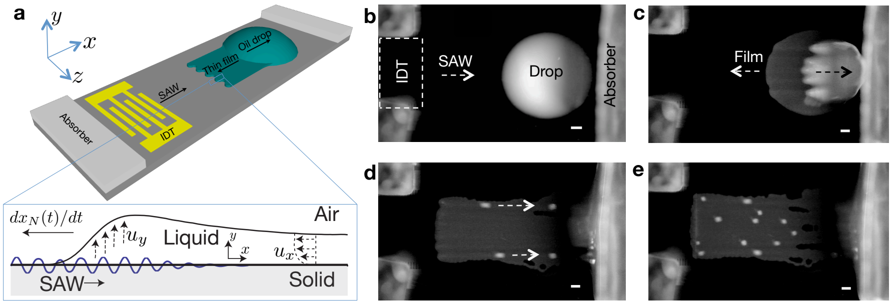

Figure 2.3: (a) Schematic illustration of the experimental setup depicting the emergence of a thin film from a sessile oil drop under the influence of a propagating SAW. The inset is a side view sketch of the film's leading edge, advancing with velocity $dx_N(t)/dt$; $x_N(t)$ is the position of the film front as it advances with time t and the characteristic flow field in the film is denoted by (u_x, u_y). The panel on the right depicts a sequence of top-view images of the drop, fluorescently labelled to aid visualisation,(b), in its initial state, that, (c), upon subsequent excitation with the SAW, is displaced along the SAW propagation direction while forming a 20 μm thick film that advances in the opposite direction. (d), This film later suffers from a transient instability that gives rise to the formation of fingering patterns. 'Soliton-like' wave pulses subsequently appear above the fingers and translate away in the SAW propagation direction, first along the side edges of the film, and then, (e), across the entire film. The scale bars denote lengths of $\approx$ 1 mm and the bright corners at the left side of the images are the electrical connections to the IDT.

revealed a double flow reversal mechanism [164] as alluded earlier and will be discussed in details later, and shown in figure 2.4; a collage showing the thickness-dependent spreading behaviour of the oil film with the critical height for reversal explained in the caption and later in this chapter. In either cases, for a drop or a film, we placed the entire initial film/drop on the substrate away from the IDT and edges, but within the IDT aperture, which was varied between 4 and 7 mm, as illustrated in Figs. 2.2(b) and 2.2(c). To capture the film spreading, we use a digital SLR camera fitted with a 60 mm F/2.8 focal length macro lens (Canon EOS 550D and EF-6, Utsnomiya, Japan) or a 30 frame/s digital video camera (AnMo Electronics Corp. AM4023 Dino-Eye, Taipei, Taiwan) attached to an epifluorescent stereomicroscope (Olympus BX-FM, Tokyo, Japan). Film thickness measurements were inferred from the distance between adjacent fringes that formed under incident light through the film and the transparent lithium niobate substrate, which we filter using a 550±10 nm optical notch filter (ThorLabs FB550–10, Newton, NJ, USA) [196]. As shown below, a rigorous mathematical derivation describing the dominant forces, relevant to the used high frequency vibration and their interactions with microfluids, at different length scales, is derived.

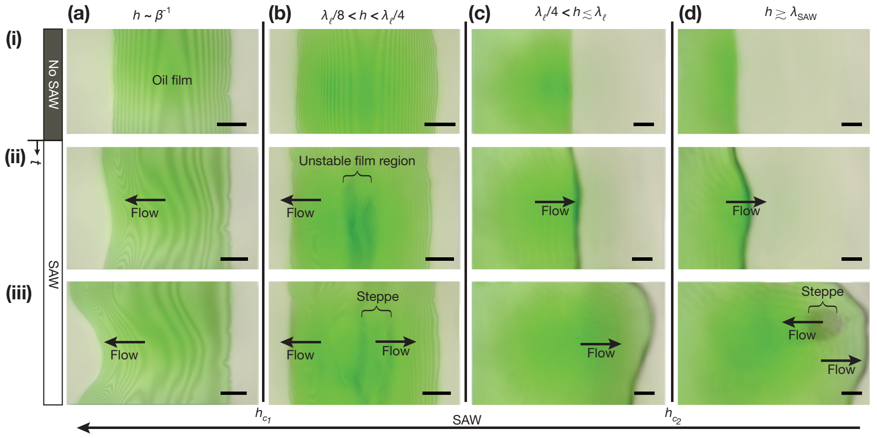

Figure 2.4: Sequential images of the double flow reversal phenomenon over time (along the vertical axis (i,ii,iii)) for different initial film thicknesses (individual columns a–d) placed as illustrated in Fig. 4.10. The SAW propagates from right to left as indicated at the bottom of the images. Row (i) is without SAW, and rows (ii,ii) illustrate the film development due to the SAW. If the film's maximum thickness is (a-i) less than or comparable to the viscous penetration length ($h \sim \beta^{-1}$), the film will move in the direction of the SAW (a-ii,a-iii). If the film is (b) slightly thicker ($\lambda_\ell/8 < h < \lambda_\ell/4$), the thicker portions of the film are unstable (b-ii) and grow to form steppes of thickness $h > \lambda_\ell/4$ that move in opposition to the SAW (b-iii). The regions surrounding these steppes decrease in thickness below $\lambda_\ell/8$ to conserve mass and move along the SAW propagation direction (b-iii). As the overall film thickness (c-i) exceeds this unstable region yet remains less than one sound wavelength in the film ($\lambda_\ell/4 < h \sim \lambda_\ell$), it continues to flow in opposition to the SAW but in a stable manner (c-ii,c-iii). Where (d) the film thickness generally exceeds the SAW wavelength $h\lambda_{\text{SAW}}$, as shown by the steppe in the bottommost image (d-iii), the flow direction reverses again, now in the same direction as the SAW. There are critical transition film thicknesses at which both the first and second flow reversals occur; these are denoted by h_{c_1} and h_{c_2}, respectively. All scale bars are ~100 μm.

2.3 GENERALISED FILM SPREADING EQUATION

We consider a two-dimensional liquid film of thickness $h(x,t)$ that spreads atop a horizontal solid substrate; the coordinates x and y are measured along and transverse (normal) to the solid/liquid boundary, respectively, and t denotes time. As illustrated in Fig. 2.5, the substrate undulates due to vibration imposed in the form of a propagating harmonic SW, such as Lamb and flexural bulk waves, or Rayleigh and Sezawa SAWs, for example. The motion of the two-dimensional SW comprises both longitudinal and transverse surface velocity (along and normal to the substrate surface) with usually similar amplitudes χU and U, respectively, that differ in time by a phase difference φ. The SW, propagating along the x coordinate along the substrate surface $y = 0$, is further defined by a wavenumber k, an angular frequency ω,

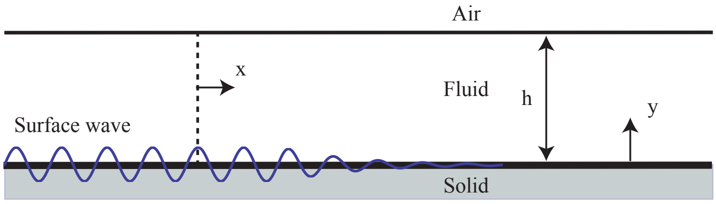

Figure 2.5: Schematic of the two-dimensional liquid film under excitation by surface waves propagating along the solid substrate.

and an amplitude attenuation coefficient α, and can be described in general form as follows:

$$\begin{pmatrix} u_x \\ u_y \end{pmatrix}_{y=0} = \begin{pmatrix} \chi U e^{i(\omega t - kx) - \alpha x} \\ U e^{i(\omega t - kx + \varphi) - \alpha x} \end{pmatrix}, \qquad (2.1)$$

the real part of which describing the actual physical SW.

The SW propagation at the solid/liquid boundary then gives rise to a predominantly viscous periodic flow, penetrating into the liquid over a distance characterised by the viscous penetration length β^{-1} while supporting a weak convective drift that possesses a steady component. For $h \gg \beta^{-1}$, this flow attenuates in the bulk of the liquid and takes the form of a boundary layer flow [127]. On the other hand, it shall be seen that interactions between this flow, invoked by direct contact between the SW and the liquid, in the presence of the free surface associated with the film constitutes the primary mechanism for its spreading when $h \sim \beta^{-1}$. Further, energy from the SW leaks into the fluid at the Rayleigh angle $\theta_R = \sin^{-1} k/k_l$, measured from the positive y-axis, resulting in the generation of longitudinal compressional acoustic waves (i.e., sound waves) in the liquid with wavelength λ_l and corresponding wavenumber k_l [58, 199]. Should the film thickness be larger than or comparable to the acoustic wavelength in the liquid, i.e., $hk_l^{-1} \gg \beta^{-1}$, these acoustic waves impinge on the free surface, generating a net acoustic radiation pressure [95, 35, 58]. Additionally, attenuation of the acoustic waves propagating in the liquid renders an effective body force that invokes Eckart streaming [49, 147, 111]. Both Eckart streaming and acoustic radiation pressure contribute to the multiple phenomena associated with spreading of films under high frequency vibration, as will be shown in §2.8 and §2.6.

In this section, we however first consider films where $h \sim \beta^{-1}$. The dominant flow in the film that arises, which is confined from below by the solid substrate along which the SWs propagate and from above by the free surface of the film, is governed by conservation equations similar to the classical boundary layer flow equations, noting that these have been used to model the convective dynamics in thin films elsewhere [19, 97, 37]. We will therefore delay an extension of the analysis to film thicknesses that approach the acoustic wavelength in the liquid—usually large with respect to the viscous penetration length ($\beta^{-1} \ll k_l^{-1}$)—where Eckart flow is dominant till §2.8.

For thin films with thicknesses on the order β^{-1}, the appropriate scaling for the variables associated with the flow field in the film are then

$$t \to \omega t, \qquad (x, y, h, \alpha^{-1}) \to k^{-1}(x, \eta y, \eta h, \alpha^{-1}),$$
$$\psi \to k^{-1}\eta U\psi, \qquad (p, p_r, \Pi) \to \eta k\gamma(p, p_r, \Pi), \qquad \mathtt{A} \to \eta^4 k^{-2}\gamma\, \mathtt{A}, \tag{2.2}$$

where $\eta \equiv \beta^{-1}/k^{-1}$ and ψ is a streamfunction satisfying $\mathbf{u} = (u_x, u_y) = ({}_y\psi, -{}_x\psi)$; γ is the interfacial tension, $\mathtt{A}$ is the Hamaker constant, and, p, p_r and Π are the hydrodynamic pressure, acoustic radiation pressure, and disjoining pressure, respectively. Unless otherwise stated, we proceed henceforth with the formulation in terms of dimensionless quantities. The relevant boundary conditions comprise that which describes the SW motion on the substrate $y = 0$ given by (4.1) and that embodying the tangential stress balance and normal stress jump at the free surface of the film $y = h\,(x, t)$:

$$\begin{pmatrix} u_x \\ u_y \end{pmatrix}_{y=0} = \begin{pmatrix} \chi e^{i(t-x)-\alpha x} \\ e^{i(t-x+\varphi)-\alpha x}/\eta \end{pmatrix}, \tag{2.3}$$

and

$$\begin{pmatrix} \partial_y u_x \\ \partial_y u_y \end{pmatrix}_{y=h} = \begin{pmatrix} 0 \\ (\eta/2\mathtt{Ca})\,(p + 2\kappa + p_r - \Pi) \end{pmatrix}, \tag{2.4}$$

respectively, where $\kappa = \partial_{xx}h/2 + \mathcal{O}\left(\eta^2\right)$ is the mean curvature of the film and $\mathtt{Ca} \equiv \mu U/\gamma$ is the capillary number. Mass and momentum conservation further require [167, 168]

$$\partial_y^4\psi/2 = \partial_t\left(\partial_y^2\psi\right) + \epsilon\left[\partial_y\psi\,\partial_x\left(\partial_y^2\psi\right) - \partial_x\psi\,\partial_y\left(\partial_y^2\psi\right)\right] + \mathcal{O}(\eta^2), \tag{2.5}$$

in which ω/k and $\epsilon \equiv Uk/\omega$ represent the phase velocity and the Mach number of the SW propagating in the solid, respectively.

Two naturally small parameters, $\eta \ll 1$ and $\epsilon \ll 1$, are observed to appear in (2.3) and (2.5). It is further reasonable to require $\epsilon \ll \epsilon/\eta \ll 1 \ll 1/\eta$ given common values for the SW velocity amplitude $U \sim \mathcal{O}(0.01 - 1\mathrm{m/s})$ under high frequency excitation [127], in particular,

$\omega/2\pi \approx 30$ MHz which is the typical frequency of the Rayleigh SAWs used, for which $\varphi = 3\pi/2$. It then follows that $\omega/k \approx 4 \times 10^3$ m/s, $\chi \approx 1$, and, $U \approx 0.1$ m/s, which, together with typical values characteristic of silicone oil, i.e., $\mu \approx 10^{-1}$ Pa·s, $\rho \approx 10^3$ kg/m^3, and $\gamma \approx 10^{-2}$ N/m, gives $\mathtt{Ca} \approx 1$, $\eta \approx 0.5 \times 10^{-1}$, $\epsilon/\eta \approx 0.5 \times 10^{-3}$ and $\epsilon \approx 2.5 \times 10^{-5}$.

We proceed by asymptotically expanding the flow variables using the following ansatz:

$$u_x = \sum_{n=-1}^{\infty} f_n u_{x,n}, \qquad u_y = \sum_{n=-1}^{\infty} f_n u_{y,n}, \qquad \psi = \sum_{n=-1}^{\infty} f_n \psi_n, \tag{2.6}$$

in which $f_{n+1} \ll f_n$ and $g_{n+1} \ll g_n$, and in which u_{xn}, u_{yn}, ψ_n, and h_n are $\mathcal{O}(1)$. The transverse and longitudinal SW components given by (2.3) determine the magnitude of the leading order velocity field $f_{-1} = 1/\eta$ and the next order correction $f_0 = 1$. Equating $\mathcal{O}(1/\eta)$ terms then specifies the leading order streamfunction equation and boundary conditions:

$$\partial_y^4 \psi_{-1}/2 = \partial_t \left(\partial_y^2 \psi_{-1} \right), \tag{2.7}$$

$$\begin{pmatrix} u_{x,-1} \\ u_{y,-1} \end{pmatrix}_{y=0} = \begin{pmatrix} 0 \\ \mathrm{e}^{i(t-x+\varphi)-\alpha x} \end{pmatrix}, \tag{2.8}$$

$$\begin{pmatrix} \partial_y u_{x,-1} \\ \partial_y u_{y,-1} \end{pmatrix}_{y=h} = \begin{pmatrix} 0 \\ 0 + \mathcal{O}(\eta^2 \mathtt{Ca}^{-1}) \end{pmatrix}. \tag{2.9}$$

Further equating $\mathcal{O}(0)$ terms gives the next order correction:

$$\partial_y^4 \psi_0/2 = \partial_t \left(\partial_y^2 \psi_0 \right), \tag{2.10}$$

$$\begin{pmatrix} u_{x,0} \\ u_{y,0} \end{pmatrix}_{y=0} = \begin{pmatrix} \chi \mathrm{e}^{i(t-x)-\alpha x} \\ 0 \end{pmatrix}, \tag{2.11}$$

$$\begin{pmatrix} \partial_y u_{x,0} \\ \partial_y u_{y,0} \end{pmatrix}_{y=h} = \begin{pmatrix} 0 \\ 0 + \mathcal{O}(\eta \mathtt{Ca}^{-1}) \end{pmatrix}. \tag{2.12}$$

It then follows that (2.7)–(2.9) are satisfied by a unidirectional periodic flow field:

$$\psi_{-1} = -\frac{1}{i+\alpha} \mathrm{e}^{i(t-x+\varphi)-\alpha x}. \tag{2.13}$$

Should the film be sufficiently thick, surpassing that of the boundary layer thickness, such that acoustic waves of wavelength k_l^{-1} generated due to leakage of the SW energy from the substrate can be sustained, this flow field then describes the propagation of such waves through the liquid. On the other hand, (2.10)– (2.12) are satisfied by the viscous-dominant periodic vortical flow field

$$\begin{aligned} \psi_0 \;=\; & \chi \left(-\frac{1}{4}+\frac{i}{4}\right) \sinh^{-2}\left[\left(\frac{1}{2}+\frac{i}{2}\right) h\right] \mathrm{e}^{i(t-x)-\alpha x} \times \\ & \left\{-\sinh\left[\left(1+i\right)\left(y-h\right)\right] - \sinh\left[\left(1+i\right) h\right] + \left(1+i\right) y\right\} \end{aligned} \tag{2.14}$$

As noted previously in Manor et al. [127], (2.14) satisfies only the $\mathcal{O}(1)$ longitudinal velocity of the solid surface and is independent of the $\mathcal{O}(1/\eta)$ transverse motion. Periodic flow to this order may thus be represented as a superposition of the unidirectional and vortical flow fields given by (2.13) and (2.14), respectively, regardless of their magnitude. This was also hinted in a recent generalised study of vibration-induced flow [199], in which a similar assertion was made by decomposing the flow field to its potential and solenoidal components.

We now show that the next correction to (2.13) and (2.14), of magnitude $f_1 \equiv \epsilon/\eta$ and emerging from weak convective interactions between the two abovementioned leading flow fields, comprises a steady component that dominates over long times. Following a procedure employed earlier [172, 186, 167, 168, 127], we decouple the velocity field to its transient and quasisteady components and time average the latter over the fast time scale ω^{-1}; physically, this is equivalent to the periodic and linear component of the flow, which alternates at a frequency $\omega/2\pi$ times every second, and their corresponding harmonics, naturally vanishing at the much slower hydrodynamic time scales over which the flow is observed.

Equating the $f_1 \equiv \epsilon/\eta$ magnitude terms, while using the momentum equation to simplify the normal stress condition [19, 150, 37], then gives, after time averaging, the following quasisteady nonvanishing components of the streamfunction equation and boundary conditions:

$$\partial_y^4 \left\langle \psi_1 \right\rangle /2 = -\left\langle \partial_x \overline{\psi}_{-1} \partial_y^3 \overline{\psi}_0 \right\rangle, \tag{2.15}$$

$$\begin{pmatrix} \langle u_{x,1} \rangle \\ \langle u_{y,1} \rangle \end{pmatrix}_{y=0} = \begin{pmatrix} 0 \\ 0 \end{pmatrix}, \tag{2.16}$$

$$\begin{pmatrix} \partial_y \langle u_{x,1} \rangle \\ \partial_{yy} \langle u_{x,1} \rangle \end{pmatrix}_{y=h} = \begin{pmatrix} 0 \\ -\left(\eta^4/\epsilon\mathtt{Ca}\right)\left(\partial_{xxx} h + \partial_x p_r - \partial_x \Pi\right) + \mathcal{O}(\eta^2) \end{pmatrix}, \tag{2.17}$$

where $\overline{\zeta}$ and $\langle\zeta\rangle$ above refer to the real component of the arbitrary function ζ and its time average, i.e., $\langle\zeta\rangle \equiv (1/2\pi)\int_0^{2\pi} \zeta \, dt$. (2.15)–(2.17) are satisfied by a long analytical solution for the streamfunction that we omit here given that it has no particular significance in the present analysis other than to note that at $f_1 = \epsilon/\eta$, it assumes the leading order nonvanishing flow field at long times, and therefore gives rise to the following expression that specifies the nondimensional, nonvanishing, leading order volume flux in the film:

$$Q = \frac{\epsilon}{\eta}\chi \mathrm{e}^{-2\alpha x} f(h(x);\varphi) + \frac{\eta^3}{3\mathtt{Ca}} h^3 \left(\partial_{xxx} h + \partial_x p_r - \partial_x \Pi\right) + \mathcal{O}\left(\frac{\epsilon}{\eta}\right), \tag{2.18}$$

wherein

$$\begin{aligned} f(h(x);\varphi) \quad \equiv \quad & \frac{1}{2\left(\cos h - \cosh h\right)^2} \times \{ \sin\varphi \left(\cos h - \cosh h\right)^2 \\ & + h\left(\cos h - \cosh h\right)\left[\sin h\left(\sin\varphi + \cos\varphi\right) + \sinh h\left(\sin\varphi - \cos\varphi\right)\right] \\ & + h^2\left(\sin\varphi \sin h \sinh h - \cos\varphi \cos h \cosh h + \cos\varphi\right) \} \,. \end{aligned} \tag{2.19}$$

The first term on the right hand side of (2.18) quantifies contributions to the volume flux from the steady component of the SW-induced flow (i.e., the convective drift) and the second term incorporates contributions from capillary forces, the acoustic radiation pressure, and the disjoining pressure invoked by intermolecular forces such as van der Waals and electrical double layer forces. Contributions from Eckart streaming due to attenuation of the acoustic wave that is generated when energy from the SW leaks into the liquid do not appear in (2.18) and will be discussed subsequently in §2.8.

The volume flux in (2.18) can then be employed to derive the requisite relationship that describes the dynamics of the liquid film under high frequency SW excitation. Given that the spreading occurs on hydrodynamic time scales, which is significantly longer than that associated with the period of forcing, i.e., $k^{-1}/U \gg \omega^{-1}$, we rescale time by

$$t \rightarrow \frac{1}{\chi}\frac{\eta}{\epsilon}\frac{k^{-1}}{U}\,t, \tag{2.20}$$

in place of the scaling presented earlier in (2.2), whilst retaining all other transformations for the rest of the variables. The kinematic condition

$$\partial_t h + \frac{1}{\chi}\frac{\eta}{\epsilon}\left(u_x \partial_x h - u_y\right) = 0 \qquad \text{at } y = h, \tag{2.21}$$

subject to continuity

$$\partial_x u_x + \partial_y u_y = 0 \tag{2.22}$$

and the homogeneous boundary conditions at the liquid/substrate interface in (2.16) then lead to the familiar integral mass conservation relationship

$$\partial_t h + \frac{1}{\chi}\frac{\eta}{\epsilon}\partial_x Q = 0, \tag{2.23}$$

which, together with (2.18) and (2.19), gives the following redimensionalised film spreading equation

$$\partial_t h - 2\alpha \mathrm{e}^{-2\alpha x} f + \mathrm{e}^{-2\alpha x}\partial_h f \partial_x h + \frac{2\Lambda}{3\chi}\partial_x\left[h^3\left(\partial_{xxx}h + \partial_x p_r - \partial_x \Pi\right)\right] = 0, \tag{2.24}$$

in which

$$\Lambda \equiv \left(\frac{\beta^{-1}}{k^{-1}}\right)^2 \mathrm{We}. \tag{2.25}$$

Here, $\mathrm{We} \equiv \rho U^2 k^{-1}/\gamma$ is the Weber number that describes contributions to the film dynamics from the SW-induced convective drift and from capillary forces.

(2.24) is therefore a generalised relationship that describes the different contributions to the film spreading dynamics, whose transient nature is captured by the first term to the left of the equation. The second and third convective terms capture SW contributions to the film dynamics through the drift flow it invokes: the former capturing contributions arising from viscous attenuation of the SW, and the latter accounting for contributions arising from the film profile. The last term on the left in (2.24), on the other hand, captures contributions from capillary, acoustic radiation pressure, and molecular forces. We note that (2.24) is governed by the dimensionless group Λ specified by (2.25) in which we observe the role of the SW-induced convective drift to become increasingly dominant as the viscous penetration length decreases in magnitude, consistent with that discussed in §2.1. Subsequently, we consider the spreading dynamics of liquid films governed by (2.24) wherein convective effects within the film are assumed to dominate capillary effects near the contact line (i.e., $\Lambda < 1$).

2.4 ULTRA-THIN $(h \sim \beta^{-1})$ FILM SPREADING

We now proceed to apply the generalised film spreading equation in 2.24 for the case of thin films: films whose thicknesses are too small to sustain the formation of acoustic waves within it due to SW energy leakage from the substrate, i.e., $h \sim \beta^{-1} \ll k_l^{-1}$, such that effects due to the acoustic radiation pressure and Eckart streaming—phenomena that are a direct consequence of the generation of acoustic waves in the liquid—are weak and can therefore be ignored. In these cases, the attenuation of the SW itself can also be neglected. This is because in the absence of acoustic waves in the thin film, the leakage of SW energy through the momentum transfer given by (2.13) which causes its attenuation occurs effectively into the air phase above the film. For example, the attenuation coefficient for Rayleigh SAWs, $\alpha \approx \rho k_f^{-1} / \left(2\pi\rho_s k^{-2}\right)$, ρ_s being the density of the solid substrate and k_f the wavenumber of the acoustic wave in the fluid phase above the substrate, for a thin film is small, typically 2×10^{-4} mm^{-1}, compared to the case of thicker films which support the formation of acoustic waves within (i.e., films where $h \gg k_l^{-1}$) where $\alpha \approx 1$ mm^{-1} [10]. For SWs in the form of propagating bulk waves, the attenuation length is even longer given the distribution of its mechanical energy throughout the solid substrate. Whichever the case, given that the SW attenuation length scale under thin films is thus much larger than the substrate length itself, it is therefore not unreasonable to assume $\alpha \to 0$ together with negligible effects due to the acoustic radiation pressure, i.e., $p_r \approx 0$.

Expanding (2.18) for small h then yields the following simplification for the volume flux expression:

$$Q = \frac{\chi\eta}{\epsilon}\left[\frac{\cos\varphi}{4}h^2 - \frac{\sin\varphi}{72}h^4 + \mathcal{O}\left(h^6\right)\right] + \frac{\eta^3}{3\mathrm{Ca}}h^3\left(\partial_{xxx}h - \partial_x\Pi\right). \quad (2.26)$$

If, for example, the film is excited by SWs in the form of Rayleigh SAWs with phase difference $\varphi = 3\pi/2$, the expression for the volume flux in 2.26 for the convective drift that is induced further simplifies to

$$Q = \frac{\chi\eta}{\epsilon}\left[\frac{h^4}{72} + \mathcal{O}\left(h^8\right)\right] + \frac{\eta^3}{3\mathrm{Ca}}h^3\left(\partial_{xxx}h - \partial_x\Pi\right). \tag{2.27}$$

The leading equation governing the dynamic spreading of the thin film in (2.24) then becomes

$$\partial_t h + \frac{1}{18}h^3\partial_x h + \frac{2}{3\chi}\Lambda\left[3h^2\partial_x h\left(\partial_{xxx}h - \partial_x\Pi\right) + h^3\left(\partial_{xxxx}h - \partial_{xx}\Pi\right)\right] \approx 0. \tag{2.28}$$

Considering earlier work on the inertial spreading of films [19], it is clear that the positive convective component (second term on the left hand side of (2.28)) drives the film to spread *along* the the SAW propagation direction.

For convenience, we rescale time again by $t \to 18t$ to further simplify (2.28) to

$$\partial_t h + h^3\partial_x h + \Lambda'\left[3h^2\partial_x h\left(\partial_{xxx}h - \partial_x\Pi\right) + h^3\left(\partial_{xxxx}h - \partial_{xx}\Pi\right)\right] \approx 0, \tag{2.29}$$

such that the SAW-induced spreading dynamics is governed by a single dimensionless parameter $\Lambda' \equiv 12\Lambda/\chi$. $\Lambda' \ll 1$ infers the case of convective film dynamics in which the spreading is governed by the second term on the left hand side of (2.29) that includes contributions arising from the SW excitation. $\Lambda' \gg 1$, on the other hand, encompasses the case in which the film dynamics is governed by capillary forces and intermolecular forces described by the third term on the left hand side of (2.29).

To further elucidate the case of convective film dynamics, we examine the limiting case in which the film spreading is solely induced by the SW by assuming the singular limit $\Lambda' \to 0$ such that (2.29) reduces to [164]

$$\partial_t h + h^3\partial_x h \approx 0. \tag{2.30}$$

We further constrain the film by requiring the conservation of its volume, i.e.,

$$\int_{x=0}^{x_1(t)} h\,dx = \text{constant}, \tag{2.31}$$

where $x = x_1(t)$ is the front position of the spreading film. A similarity solution for the above equations can then be obtained by introducing the following similarity transformation:

$$\xi \equiv x/t^a, \qquad H \equiv h/t^b, \qquad t = \tau, \tag{2.32}$$

which, upon substitution, render (2.30) and (2.31) time independent, i.e., $\partial_\tau H = 0$, when $3b - a + 1 = 0$ and $a = -b$. It then follows that $a = 1/4$ and $b = -1/4$ such that the leading edge of the film spreads as

$$x_1 \sim t^{1/4}, \tag{2.33}$$

whilst the film decreases in height as

$$h(x) \sim t^{-1/4}, \tag{2.34}$$

eventually approaching a singularity as the rear of the film catches up with its advancing front, leading to a steepening of the slope near the advancing front where the influence of capillary and intermolecular forces, though assumed insignificant to begin with, becomes sufficiently strong to overcome the assumed initial dominance of the convective term in (2.29).

To further support the postulated mechanism and spreading dynamics, experimental and numerical investigations were carried out. For experiments, the corresponding plot for the film flow in the SAW propagation direction is shown in figure 2.4(a) and the variation in the position of the advancing film front as a function of time, seen in Fig. 2.6, shows that the film advances self-similarly as $t^{1/4}$, as predicted by (2.33)—not unsurprisingly, given that the experimental parameters render $\Lambda' \approx 0.00014$ in (2.29) such that the spreading resembles the dynamics of inertially-driven films. This is further verified by numerical simulations in which (2.29) is solved using the Numerical Method of Lines [171] subject to no-flux boundary conditions

$$\partial_x h|_{x\to\pm\infty} = 0, \qquad \partial_{xxx}|_{x\to\pm\infty} = 0, \tag{2.35}$$

and the following initial condition:

$$h|_{t=0} = \sinh^{-1} x. \tag{2.36}$$

In the numerical scheme, fourth-order centered differences were employed for the discretisation of spatial derivatives whereas Gear's method was used for advancing the solution in time. The parameters used for the simulation are f = 19.5 MHz, μ = 50 mPa.s, $A = 10^{-19}$, Λ

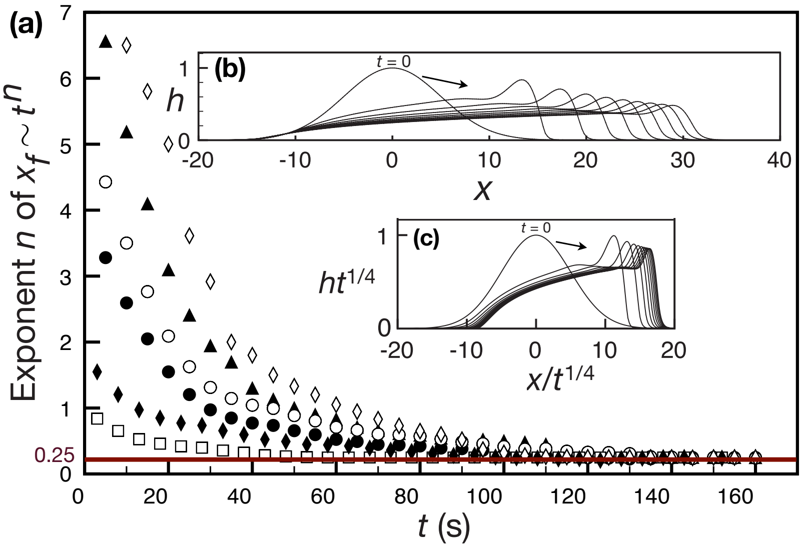

Figure 2.6: Position of the advancing front of very thin ($\sim$1 μm) silicone oil films x_1 as a function of time t. The circles are experimental points and the squares are those predicted by numerical simulations, both of which indicate that the film spreads in a self-similar fashion as $x_1 \sim t^{1/4}$ Also shown in the inset are the spatiotemporal evolution profiles of the spreading film, obtained from the numerical simulation. Experimental parameters were f = 19.5 MHz, μ = 50 mPa.s, $A = 10^{-19}$ and Λ = 0.00014

= 0.00014 over maximum spatial domains of 600 k^{-1} dimensionless units and times of 0.1610^{-5} dimensionless units, with 4500 grid points; convergence was obtained by refinement of the mesh.

2.5 ACOUSTIC RADIATION PRESSURE AND FILM STABILITY

As explained earlier in §2.4 for ultra-thin films, they move along the SAW propagation direction as shown in the time sequence images in fig. 2.4(a) and 2.7 (a, i), as long as their thickness is $\sim \beta^{-1}$. As the film thickness was experimentally increased, the films were observed to experience bizarre instability where the thicker portions of these films were observed to 'pop' and grow to a thicker stable state and then move in a direction opposite to the SAW propagation direction, shown in the time sequence column in fig. 2.4(b) and the phase map in fig. 2.7 (a, ii) to (iii). As the film was increased in thickness, it moved stably opposite to the SAW propagation direction as seen in fig. 2.4(c) and in fig. 2.4(iii). The physics governing the film instability and flow in opposite direction to SAW is explained below in the light of thickness dependent radiation pressure as seen in fig. 2.7 (b) and linear stability analysis. We also note that even thicker films (called thick films in this thesis) were observed to reverse flow direction, again, but due to sound attenuation in the fluid, known as Eckart streaming, as we shall explain in §2.8.

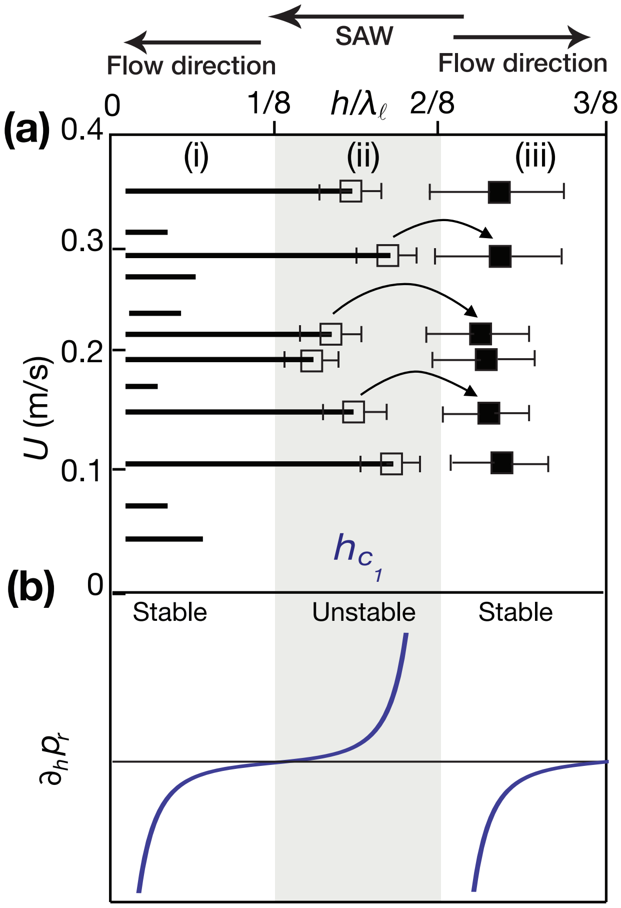

Figure 2.7: The experimental behavior of the spreading film is illustrated through (a) a phase plot of the vibration velocity of the substrate, U dependent upon the normalized film thickness, h/λ_ℓ, using different starting film thicknesses, oil viscosities μ = 50,100 and 500 mPa·s; and SAW frequencies 19.5, 32.7, and 48.5 MHz; for clarity, the distinction between individual parameter choices in the figure is not illustrated. The solid horizontal lines on the left in region (i) indicate the thickness range of stable films observed to move along the SAW propagation direction, as indicated by the arrow on the top of the figure and shown in Fig. 4.10(a). The solid horizontal lines terminating at the white squares with min-max error bars ($n = 5$), are for films with portions having thicknesses greater than $h/8\lambda_\ell$. These portions are unstable according to linear stability theory, as shown in Fig. 4.10(b): positive values of $\partial_h p_r$ correspond to an unstable film, consistent with experimental observations. Acoustic radiation pressure acts to rapidly thicken these portions of the film to a new stable thickness, a steppe, from the white squares; before SAW is applied) to the black squares; after SAW). The film takes heights either in regions (i) or (iii) with a pronounced gap in region (ii), between the upper limit of the thinner film (white squares), and the steppe regions' thicknesses (black squares). The portions of the film in region (i) move with the SAW, the portions of the film in region (iii) move against it.

2.5.1 *Acoustic radiation pressure*

In anticipation of our analysis in §2.8 for the spreading of thick films, i.e., films with sufficient thickness ($hk_l^{-1} \gg \beta^{-1}$) to support the leakage of the SW energy into the fluid, we now turn to a discussion on the acoustic radiation pressure and how it could potentially affect the stability of the film. Owing to the large difference in acoustic impedance (density times the speed of sound) across the free surface, the transfer of momentum associated with the generation of acoustic waves in the liquid upon leakage of the SW energy into the liquid from the substrate produces a net steady force on the free surface over long times ($t \gg 1/\omega$). This is known as the acoustic radiation pressure [95, 35, 73, 23, 58] and takes the generalised form

$$p_r = (p\mathbf{I} \cdot \mathbf{n}) \cdot \mathbf{n} + (\langle \rho \mathbf{u}\mathbf{u} \rangle \cdot \mathbf{n}) \cdot \mathbf{n}, \tag{2.37}$$

where $\mathbf{I}$ and $\mathbf{n}$ are the identity tensor and the unit outward normal vector to the free surface, respectively. In particular, we examine acoustic radiation pressure effects along the nearly flat portion of the free surface of the film away from its advancing front in the vicinity of the contact line. It shall be shown that these nearly flat free surfaces serve as a near-ideal reflector (as a consequence of the large jump in the acoustic impedance across the free surface) of the acoustic waves that form in the liquid due to leakage off the SW energy, and gives rise to acoustic resonances and anti-resonances within the film, thus leading to appreciable acoustic radiation pressure effects at specific film thicknesses.

More specifically, the acoustic waves propagating in a liquid can be described predominantly by a potential flow field generated by the normal component of the SW velocity u_y in (4.1), whose local form, we assume, for simplicity, resembles a completely in-phase vertical substrate motion of a pistonlike acoustic wave transducer—not unreasonable given $h/k^{-1} \sim 1$. It then follows that the parallel acoustic waves generated from such pistonlike motion of the substrate produces an acoustic radiation pressure at the free surface of the form [36]

$$p_r \approx \mathtt{We}_a \frac{\mathrm{e}^{-2\alpha x}}{\cos^2\left[(k_l/\beta)\,h\right] \sin^2\left[(k_l/\beta)\,h\right]}. \tag{2.38}$$

$\mathtt{We}_a \equiv (1 + B/2A)\rho_{air} U^2 k^{-1}/8\eta\gamma$ is an acoustic Weber number that describes the relative magnitudes of the acoustic radiation and capillary pressures acting at the free surface, in which B and A are the Fox and Wallace coefficients [35] and ρ_{air} is the density of the air

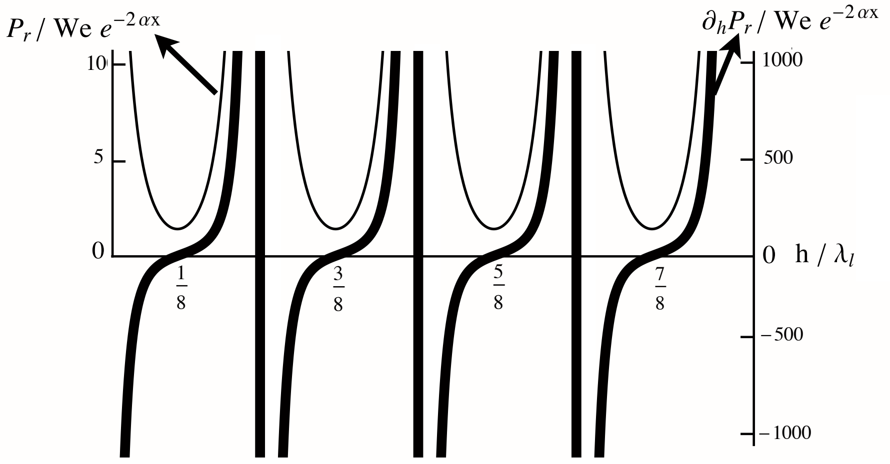

Figure 2.8: Dimensionless acoustic radiation pressure and its gradient as a function of the scaled film thickness.

phase above the liquid film. It can then be seen from Fig. 2.8 that p_r decays to negligible values at the vicinity of each of its minima at $h/2\pi k_l^{-1}\beta = (1+2i)/8$ $(i = 0, 1, 2, \ldots)$ and becomes singular at $h/2\pi k_l^{-1}\beta \to 2i/8$ $(i = 0, 1, 2, \ldots)$, suggesting that the film, being nearly flat, may only assume stable quantum thickness values, consistent with that observed in previous experiments [36]. In particular, low surface energy oil films were found to spread with a characteristic film thickness corresponding to $i = 3$ [162] while high surface energy water films were found to form with a quasisteady film thickness corresponding to $i = 7$ and to undergo further transient plateaus formation that span a variety of thicknesses corresponding to $i > 7$ [36].

We however note that the $hk_l^{-1} \gg \beta^{-1}$ constraint for (2.38) suggests that the singular result for small h, i.e., $h \sim \beta^{-1} \ll k_l^{-1}$, is therefore not valid given that p_r diminishes to leading order. More specifically, p_r is linearly proportional to the average excess acoustic energy in the film, i.e., $p_r \propto \langle E \rangle$, where along the path of the acoustic waves emitted by the SW [35],

$$E = \frac{\omega}{2k_l}\frac{\rho^L - \rho}{\rho} + \frac{\rho u_y^{L2}}{2}; \tag{2.39}$$

the right hand side of the equation describing the Lagrangian excess potential and kinematic energies with respect to the normal SW velocity arising from the deviation of the Lagrangian density and normal velocity fields, ρ^L and $u_y^L = u_y - \mathrm{e}^{i(t-x+\varphi)-\alpha x}/\eta$, from their equilibrium values, ρ and $u^L = 0$, respectively. For sufficiently thin films of thicknesses $h \sim \beta^{-1} \ll k_l^{-1}$ which do not permit the generation of acoustic waves in the liquid, the flow in the film is strictly the unidirectional flow field in (2.13), which, together with $u_y^L = 0$ and

$\rho^L = \rho$ that causes the excess energy in the film in (2.39) to vanish, leads to

$$p_r \approx 0. \tag{2.40}$$

For thicker liquid films that are able to sustain the generation of acoustic waves in the liquid, the leading approximation to the actual transverse flow component (2.13) can be used in place to calculate the effect due to the acoustic radiation pressure on the spreading, which we shall consider in §2.8.

2.5.2 *Linear Stability*

We now turn our attention to the instability apparent in experiments on films with thicknesses $\lambda_\ell/8 < h < \lambda_\ell/4$ while exposed to the SAW (Fig. 4.10(b-ii)), corresponding to region (ii) in the phase plot given in Fig. 2.7(a). The instability appears to be driven when the acoustic radiation pressure imparted on the free surface of the film, which forces it upwards such that the film thickness is increased to an extent that it can no longer be balanced by restoring capillary forces. This is because while radiation pressure is negligible in a sufficiently thin film ($h \sim \beta^{-1}$), causing it to spread solely due to the drift flow along the direction of the SAW as governed by Eq. (2.29), an increase in the film thickness into the range $\lambda_\ell/8 < h < \lambda_\ell/4$ (Fig. 4.10(b)) leads to significant acoustic radiation pressure on the film, overwhelming the restoring capillary forces, in turn driving the observed instability in the film thickness.

We now consider a linear stability analysis to obtain a theoretical prediction for this observed unstable film thickness range and hence the critical film thickness at which the transition occurs h_{c_1}. Briefly, we linearize the film evolution equation given by Eqs. (2.29) far from the contact line, retaining effects due to the acoustic ÃŁradiation pressure but excluding the relatively weak contributions arising from the disjoining pressure

$$\partial_t h \approx -\frac{U^2}{18\omega}\frac{h^3}{\beta^{-4}}\partial_x h - \frac{1}{3\mu}\partial_x\left[h^3\left(\gamma\partial_{xxx}h + \partial_x p_r\right)\right]. \tag{2.41}$$

Introducing a periodic disturbance to the film thickness

$$h(x,t) = h_0 + \delta g(x,t), \tag{2.42}$$

in which $\delta/h_0 \ll 1$ and $g(x,t) = C\exp\left(inx + \sigma t\right) \sim \mathcal{O}(1)$, where h_0, C, n and σ are the base state film thickness, an arbitrary constant, the disturbance wavenumber, and the corresponding growth rate of the film thickness, respectively. Omitting complex and small $\mathcal{O}(\delta^2)$ contributions then simplifies Eq. (2.41) to the $\mathcal{O}(\delta)$ linear equation

$$\partial_t h \approx -\frac{h_0^3}{3\mu}\left(\gamma\partial_{xxxx}h + \partial_h p_r|_{h=h_0}\partial_x h\right) + \ldots, \tag{2.43}$$

from which we obtain the real disturbance growth rate coefficient

$$\sigma = -\frac{n^2 h_0^3 \gamma}{3\mu}\left[n^2 - \frac{1}{\gamma}\,\partial_h p_r|_{h=h_0}\right], \tag{2.44}$$

indicating that capillary forces act to stabilize the film ($\sigma < 1$) while the radiation pressure p_r acts to destabilize it ($\sigma > 1$) when σ increases with increasing h.

Substituting for p_r in Eq. (2.44) using Eq. (2.38) then reveals that the film is stable only over specific thicknesses in the range $2j\lambda_\ell/8 < h < (1+2j)\lambda_\ell/8$ $(j = 0, 1, 2, \ldots)$. This behavior is represented in part by the solid horizontal lines in Fig. 2.7(a), the range of stable film thicknesses found in the experiment. It can be seen that these primarily reside in region (i) when $h < \lambda_\ell/8$, consistent with the range predicted above with $j = 0$ and corresponding to the films whose behavior is exemplified by Fig. 4.10(a). In region (ii) in between the predicted $j = 0$ and $j = 1$ stable regions, as illustrated by the shaded region in Fig. 2.7(b), however, the film tends to rapidly form thicker plateaus under the action of the acoustic radiation pressure, scavenging fluid from adjacent regions to reduce the thickness of those regions, and altogether remaining within the stable thickness ranges. This is seen by the truncation of the solid horizontal lines by the squares () in Fig. 2.7(a), with the curved arrows in the plot indicating the jump in the film thickness to the points indicated by the filled squares () in the next stable region, region (iii) in Fig. 2.7(a) corresponding to the next predicted stable region $j = 1$, associated with the formation of the steppes.

In reality, the experimental data denoted by the solid horizontal lines in Fig. 2.7(a) indicate that the film remains stable even into region (ii), the region of instability predicted by linear stability theory. This is likely due to the omission of azimuthal γ/h curvature effects from the capillary stress term in Eq. (2.44) in the linear stability analysis, as demonstrated in examining a dominant balance between the azimuthal curvature and the time-averaged Reynolds stress ρU^2 that gives rise to the acoustic radiation pressure. Imposing volume conservation of the film $hL \sim 1$ in the resultant relationship $h \sim L\mathrm{We}^{-1}$, where L is the characteristic film length scale and $\mathrm{We} \equiv \rho U^2 L/\gamma$ is an acoustic Weber number, explains the $h \sim 1/U$ scaling of the experimental data

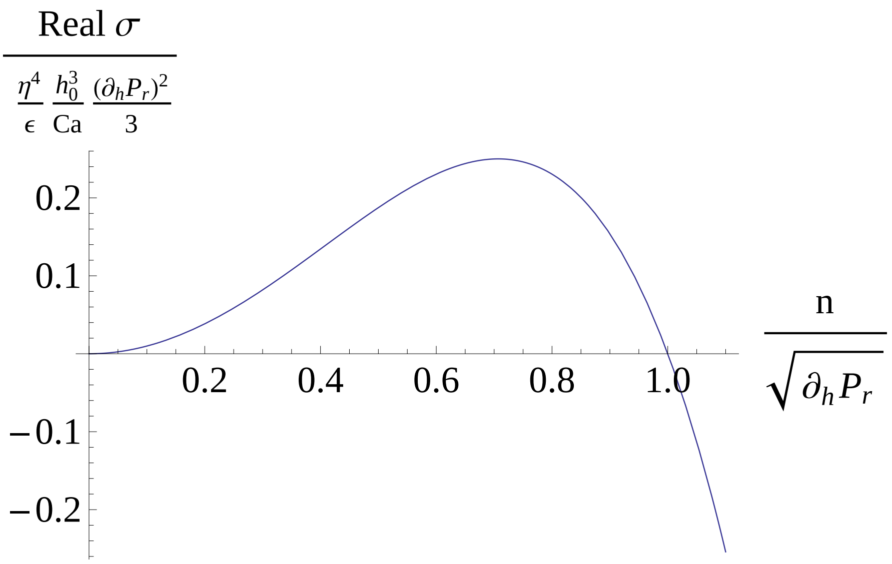

Figure 2.9: Eigenvalues of the real component of the instability growth rate Re[σ] as a function of the disturbance mode n, showing that the film is always stable for $\partial_h p_r < 0$ and unstable for long wavelengths, i.e., short wavenumber modes below $n = \partial_h p_r$.

in Fig. 2.10 for the threshold film thickness h_{c_1} beyond which the film becomes unstable in region (ii) of Fig. 2.7.

2.6 INTERMEDIATE STABLE FILMS

We now turn our attention to an analysis of the spreading dynamics of these stable intermediate (also called thin in this thesis) films, shown in figure 2.1 (b) and (c), 2.4(c) and 2.7 (a, iii)—films whose thicknesses $hk_l^{-1} \gg \beta^{-1}$ are sufficiently large to permit appreciable generation of acoustic waves in the film as a consequence of energy leakage from the SW on the substrate into the liquid. Under these circumstances, contributions to the spreading dynamics due to the acoustic radiation pressure, SW attenuation and Eckart streaming, whose effects were negligible in the thin film limit in §2.4, need to be taken into account. In §2.6, we, however, first consider films of intermediate thicknesses on the order k_l^{-1} (typically 10–100 μm for common liquids for the system parameters specified in §2.3) in which only the first two contributions are dominant, and defer the introduction of effects due to Eckart streaming in very thick films and sessile drops ($h \gg k_l^{-1}$) to §2.8.

The considered stable intermediate films here with thicknesses comparable to the acoustic wavelength in the liquid, $hk_l^{-1} \gg \beta^{-1}$, that, under high frequency SW excitation (Fig. 2.11), satisfies the periodic stable film thickness constraint in with the exception of the region next to the three-phase contact line. The larger thicknesses of such films, however, means that there is now appreciable SW energy leakage

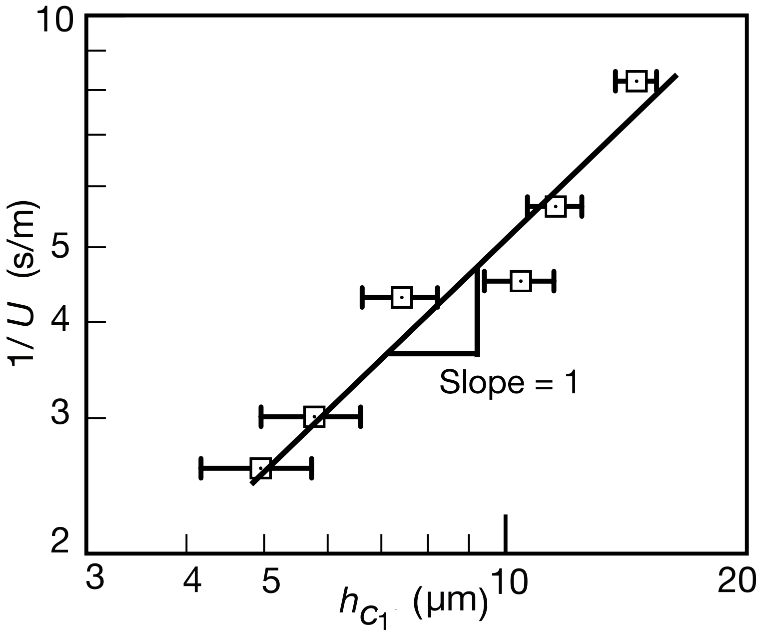

Figure 2.10: Correcting the linear stability prediction by accounting for the azimuthal curvature of the film in the capillary stress term of Eq. (2.44) is seen to improve the prediction of the onset of fluid instability in region (ii) of Fig. 2.7(a).

from the substrate which, in turn, generates acoustic waves in the liquid, therefore supporting the attenuation of the SW along its propagation axis as well as the generation of an acoustic radiation pressure at the free surface of the film. Ignoring edge effects and adopting a similar approach to the linearisation in §2.6, the film thickness can be assumed to approach a stable nominal value h_0—considered large with respect to the viscous penetration length since $\beta^{-1} \ll k_l^{-1}$ (i.e., $h_0 \gg 1$) [165, 186, 199]—thus relegating any small deviations from the equilibrium film thickness to the dominant balance between the capillary and acoustic radiation pressures considered earlier. To leading order, intermolecular forces can be neglected and since the acoustic radiation pressure is satisfied by the capillary pressure, the volume flux in (2.18) for the stable, nearly flat film can thus be approximated by

$$Q|_{h \gg 1} \rightarrow \frac{\epsilon}{\eta} \frac{\chi \mathrm{e}^{-2\alpha x}}{2} \left(\cos\varphi - \sin\varphi\right) h. \tag{2.45}$$

From (2.23), the generalised film spreading equation (2.24), to leading order, then takes the form

$$\partial_t h = -\partial_x \left[\frac{\chi \mathrm{e}^{-2\alpha x}}{2} \left(\cos\varphi - \sin\varphi\right) h \right], \tag{2.46}$$

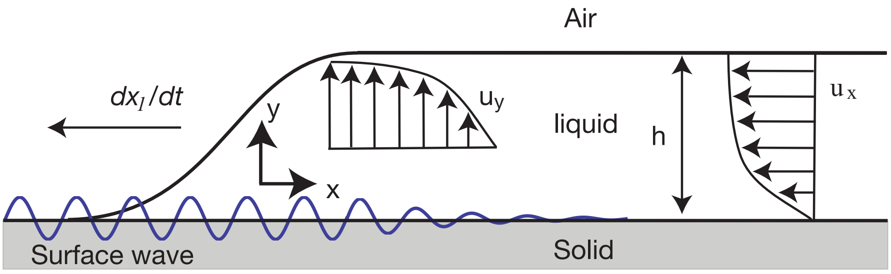

Figure 2.11: Schematic of the leading edge of a film of intermediate thickness where the SW penetrates the liquid and is attenuated. The Eulerian film spreading velocity is denoted by dx_1/dt.

subject to the approximated film profile

$$h/h_0 \approx 1 \qquad 0 < x < x_2(t), \tag{2.47}$$

where $x = 0$ is the position of the film front where the liquid first meets the propagating SW and $x = x_2(t)$ is the position of the film's rear edge; for simplicity, the film is assumed to terminate sharply at these positions. In contrast to the case of thin films in §2.4, we retain the term that accounts for the exponential decay of the SW under the liquid for the case of Rayleigh SAWs since there is a loss in the momentum of the SAW, generated at $x \to -\infty$, once it penetrates the film at $x = 0$ and leaks its energy into the liquid, generating acoustic waves in the liquid as a result.

The nearly constant thickness $h \approx h_0$ associated with the nearly flat stable film, which is a consequence of the leading order balance between the capillary and acoustic radiation pressures, nevertheless, does not permit the usual Lagrangian treatment of the film spreading dynamics in which the advancing film front, in a reference frame that moves with the front, thickens to satisfy the flow into the contact line region (in this case, the convective drift generated by the SW vibration) whilst the trailing edge of the film thins to conserve the overall mass of the film. Instead, the film thickness away from the advancing front remains relatively constant ($h \approx h_0$) and any small deviation from the stable thicknesses is suppressed due to capillary forces. Mass conservation of the film then requires its free surface to be 'displaced' in the direction opposing that of the SW-induced drift given by (2.18). For SWs whose propagation results in the retrograde trajectory of the solid particle elements along the substrate, such as that in Rayleigh SAW, $\varphi = 3\pi/2$ and hence the convective drift, from (2.18), is in the same direction as the SW propagation direction. On the other hand, SWs whose propagation results in the prograde trajectory of the solid particle elements along the substrate, such as that in Sezawa SAW, $\varphi = \pi/2$ and hence the drift is in the direction opposite to that of the SW propagation. In the case of the Rayleigh SAW, therefore, the spreading of films of intermediate thicknesses occur in the direction that opposes that of the SAW propagation in the Eulerian framework, in contrast to the case of the co-propagating thin films in §2.4 which are not subject to acoustic radiation pressure effects and hence the constant thickness constraint (Fig. 2.1(a)).

Thus, reverting to an Eulerian framework using the coordinate transformation $(x^{\mathrm{E}}, y^{\mathrm{E}}) = (x + x_1(t), y)$ and $\partial_t = \partial_{t^{\mathrm{E}}} + (dx_1/dt)\partial_{x^{\mathrm{E}}}$, (2.46) can be written as

$$\partial_{t^{\mathrm{E}}} h + (dx_1/dt)\,\partial_{x^{\mathrm{E}}} h = -\partial_{x^{\mathrm{E}}}\left[\frac{\chi \mathrm{e}^{-2\alpha\left(x^{\mathrm{E}} - x_1(t)\right)}}{2}(\cos\varphi - \sin\varphi)\,h\right], \tag{2.48}$$

where $x_1(t)$ is the position of the advancing film front in the Eulerian framework where the SW penetrates the liquid. Upon spatial integration over the film and using Leibniz's rule, (2.48) then becomes

$$\begin{aligned}\partial_{t^{\mathrm{E}}} \int_{x_1}^{x_2} h\,dx + h\left(\frac{dx_1}{dt} - \frac{dx_2}{dt}\right) + \frac{dx_1}{dt}\int_{x_1}^{x_2} \partial_{x^{\mathrm{E}}} h\,dx = \\ -\frac{\chi h}{2}(\cos\varphi - \sin\varphi)\left[1 - \mathrm{e}^{-2\alpha(x_2(t) - x_1(t))}\right].\end{aligned} \tag{2.49}$$

Assuming that the mass of the spreading film does not change significantly over time, the first term in (2.47) can be omitted and hence we obtain

$$\frac{dx_1}{dt} - \frac{dx_2}{dt} = -\frac{\chi}{2}(\cos\varphi - \sin\varphi)\left[1 - \mathrm{e}^{-2\alpha(x_2(t) - x_1(t))}\right]. \tag{2.50}$$

Physically, this implies that while the stable film thickness is governed by a balance between acoustic radiation pressure and capillary stress, the SW-induced volume flux in the film must be balanced by a complementary volume flux, invoked by the displacement of the film's edges, i.e., the spreading of the film front, in order for mass to be conserved.

When the film is drawn out from a large fixed reservoir, such as a large sessile drop whose volume is significantly greater than that of the film, $dx_2/dt \approx 0$ and the SW essentially attenuates completely underneath the film and in the reservoir so that $\alpha(x_2(t) - x_1(t)) \gg 1$. In this case, (2.50) can be simplified to

$$\frac{dx_1}{dt} = -\frac{\chi}{2}(\cos\varphi - \sin\varphi), \tag{2.51}$$

or, in dimensional form,

$$\frac{dx_1}{dt} = -\frac{\chi}{2}\frac{\epsilon}{\eta}U(\cos\varphi - \sin\varphi) = -\frac{\chi}{2}\frac{U^2}{\omega\beta^{-1}}(\cos\varphi - \sin\varphi), \tag{2.52}$$

which describes the dynamic spreading of the film's leading edge. For SWs in the form of Rayleigh SAWs ($\varphi = 3\pi/2$), film spreading occurs in the direction opposing that of the SW propagation, consistent with that alluded to above.

Parenthetically, we note that the mechanism introduced here is equivalent to the Rayleigh streaming induced spreading discussed in a different work we derived [162]. The difference in the prefactor to (2.51), i.e., $1/2$ as opposed to $1/6 \log 2$ in the other result, simply arises due to the different boundary conditions employed. Here, the normal stress jump in (2.9) accounts for the balance in capillary and acoustic radiation pressures at the free surface, whereas in the other work, a stress-free condition for the normal stress at the free surface in the large capillary number limit was assumed, that gave rise to the 1/6 factor multiplied by the curvature, resulting in the $1/\log 2$ prefactor. Comparison of both theories to the experimental results nevertheless suggests that both approximations are in good agreement with that observed.

When, for example, the $1/6 \log 2$ prefactor solution is scaled with SAW wavelength λ_{SAW}, the position of the advancing film front x_N as a function of time t reads

$$x_N(t)/\lambda_{\mathrm{SAW}} \approx -\left(1/6 \log 2\right)\left(t/t_c\right), \tag{2.53}$$

where $t_c \equiv \mathrm{Re}_s^{-1/2} \left[\lambda_{\mathrm{SAW}} / \left(U^3/c_{\mathrm{SAW}}\right)^{1/2}\right] = (2\pi/\epsilon)(\beta^{-1}/U)$ is a characteristic spreading time scale, in which $\epsilon \equiv U/c_{\mathrm{SAW}}$ is the Mach number in the solid and $\beta^{-1} \equiv (\mu/\pi\rho f)^{1/2}$ is the viscous penetration length. ρ and μ are the fluid density and viscosity, respectively, U is the substrate (SAW) displacement velocity amplitude, c_{SAW} is the propagation speed of the SAW of frequency f, and $\varphi = 3\pi/2$ is the phase difference between its longitudinal and transverse components, which have roughly the same amplitude. We note that the streaming Reynolds number $\mathrm{Re}_s \equiv \rho U \lambda_{\mathrm{SAW}}/4\pi\mu$ is small, indicating that the spreading of the film is driven by a weak convective mechanism—*Stokes drift*—invoked by the viscous-dominant Rayleigh streaming in the film. Not only is the linear relationship in equation (2.53) in qualitative agreement with the experimental observations presented in Fig. 2.12 (a), there is also very good quantitative agreement between our theoretical prediction and the experimental results (see Fig. 2.12a inset), remarkably in the absence of any empirical fitting parameters. This inspires confidence in the proposed *Rayleigh streaming* theory as the underlying film spreading mechanism. Further comparison between the theoretically predicted and experimentally measured film velocities over a range of SAW amplitudes and frequencies, and fluid viscosities is given in Figs. 2.12 (b) and (c).

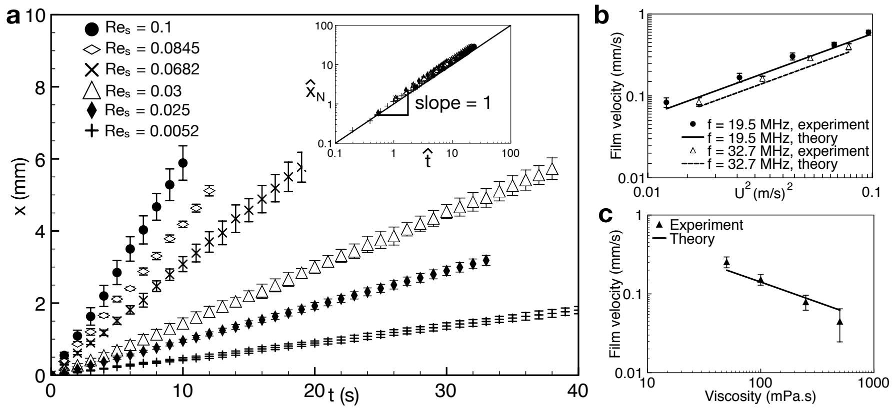

Figure 2.12: (a) Displacement of the advancing film front x_N with time t as a function of the substrate (SAW) displacement velocity U, fluid viscosity μ and frequency f, parameterised by the streaming Reynolds number Re$_s$. The same experimental data is replotted in dimensionless form in the inset by normalizing x_N and t with the scaling apparent in equation (2.53), i.e., $\hat{x} \equiv x_N/\lambda_{\mathrm{SAW}}$ and $\hat{t} \equiv -(1/6\log 2)\, t/t_c$, where λ_{SAW} is the SAW wavelength and t_c is the characteristic spreading time scale; the collapse of the data with the universal spreading law derived indicates the excellent agreement between the theoretical prediction and experimental observations. Legend: $+$: $U = 0.16$ m/s, $\mu = 500$ mPa.s, $f = 19.5$ MHz (Re$_s$ $= 0.0052$, $\beta^{-1} = 1.14 \times 10^{-6}$ m); : $U = 0.13$ m/s, $\mu = 50$ mPa.s, $f = 32.7$ MHz (Re$_s$ $= 0.025$, $\beta^{-1} = 2.78 \times 10^{-7}$ m); $\triangle$: $U = 0.185$ m/s, $\mu = 100$ mPa.s, $f = 19.5$ MHz (Re$_s$ $= 0.03$, $\beta^{-1} = 5.1 \times 10^{-7}$ m); $\times$: $U = 0.21$ m/s, $\mu = 50$ mPa.s, $f = 19.5$ MHz (Re$_s$ $= 0.0682$, $\beta^{-1} = 3.6 \times 10^{-7}$ m); : $U = 0.26$ m/s, $\mu = 50$ mPa.s, $f = 19.5$ MHz (Re$_s$ $= 0.0845$, $\beta^{-1} = 3.6 \times 10^{-7}$ m); ●: $U = 0.31$ m/s, $\mu = 50$ mPa.s, $f = 19.5$ MHz (Re$_s$ $= 0.1$, $\beta^{-1} = 3.6 \times 10^{-7}$ m). β^{-1} is the viscous penetration length. Two distinct devices were used to generate the two SAW frequencies reported in the data set. The subfigures on the right portray the variation in the velocity of the advancing film front with (b) the substrate (SAW) displacement velocity amplitude U, and, **c**, the fluid viscosity, showing the comparison between the experimental data and the theoretical prediction given by equation (2.53). In the former, the fluid viscosity is held constant at 100 mPa.s and in the latter, U = 0.185 m/s. The SAW frequency is fixed at 19.5 MHz in the latter case. In all cases, error bars denote the standard error for $n = 3$ runs for each data set.

2.7 FINGERING INSTABILITIES DUE TO FRESNEL DIFFRACTION

As shown in Fig. 2.3, the interdigital transducer (IDT) electrode comprises 42 interdigitated finger pairs of finite aperture, the center of each pair being placed one SAW wavelength away from the center of the adjacent pair. Each interdigitated electrode pair is modelled as a one-dimensional linear 'slit' with length L equal to the IDT aperture, emitting a SAW directed normal to the 'slit' in both the positive and negative x_0 directions, in analogy to the identical effect seen in optics in light propagating from finite width slits. Ignoring reflection of the SAW upon contact with subsequent electrode pairs, the effects of the metallisation ratio, and other nonlinear effects that are not direct contributors to the Fresnel diffraction, we model the mutual SAW signal from the 42 interdigitated electrode pairs as a superposition of the SAW signal emitted from the same number of one-dimensional 'slits', each 'slit' separated from its neighbour 'slit' by one SAW wavelength. The spatial intensity of the SAW produced by one 'slit' is then given by the Kirchhoff integral and is approximated here by a Fresnel integral of the form

$$A_n(x_{0,n}, z_0) = \frac{1}{\sqrt{2}} \int_{N^-}^{N^+} \mathrm{e}^{-i\pi\zeta^2/2} d\zeta, \tag{2.54}$$

where

$$N^{\pm} \equiv \frac{x_{0,n} \pm L/2}{\sqrt{\lambda_{\mathrm{SAW}} z_0/2}}. \tag{2.55}$$

In the above, $x_{0,n} = x_0 - n\lambda_{\mathrm{SAW}}$ and z_0 are Eulerian spatial coordinates tangent to the solid surface, along and transverse to the SAW propagation axes, respectively, with their origin located at the center of 'slit' n. $z_0 = \pm L/2$ are the transverse coordinates representing the edges of the 'slit'. The spatially superimposed absolute SAW intensity produced by the IDT is then given by the summation rule

$$A(x_0, z_0) = \sum_n A_n(x_{0,n}, z_0). \tag{2.56}$$

For convenience, we model the SAW diffraction by setting the origin of the Eulerian coordinate x_0 in equation (2.56) at the outer IDT 'slit' first encountered by the liquid film. Considering comparisons between theory and experiment in earlier work[36–38], the agreement obtained between the predictions obtained from equations (2.54)–(2.56) with the experimental results is fairly reasonable with deviations isolated to the mid-section of the SAW beam, as observed in Fig. 2.13. These deviations can possibly be attributed to the simplifying approximation of a simple 'slit' from which a sound beam is emitted to model the Rayleigh wave SAW beam generated when each IDT pair operates out-of-phase with the other, the omission of wave reflections on contact with subsequent electrode pairs, the high SAW energy density that gives rise to second order nonlinear effects in its transmission path, and, to a lesser degree, the use of a theory for homogenous substrates (i.e., the speed of sound is identical in all directions) to model SAW diffraction atop the lithium niobate substrate, which is weakly-heterogeneous, at least along the surface in the present crystal cut.

The images in Figs. 2.3(d) and 2.13 show the transverse fingering instability that subsequently develops along the advancing film front. Laser Doppler vibrometer (LDV) scans of the substrate displacement velocity directly beneath the fingers in Fig. 2.13a reveal the existence of transverse variations in the SAW amplitude. Agreement between the LDV measurements with predictions based upon a Fresnel integral diffraction model (see Supplementary Information for further details of the model), as seen in Fig. 2.13(a), then suggests that the transverse SAW amplitude variation arises as a consequence of Fresnel diffraction due to the finite aperture of the interdigital transducer (IDT) electrode; a modest quantitative discrepancy is present, common in the modelling of Fresnel diffraction phenomena. Given the dependence of the wetting speed of the advancing film front on the SAW amplitude U, apparent from equation (2.53), such transverse variations in U impose a corresponding fluctuation in the wetting speed across the leading edge of the film, and drives a transverse instability that results in the fingering patterns observed in Figs. 2.3(d) and 2.13(a).

This is further corroborated by favourable comparisons between the fingering patterns and the Fresnel diffraction distribution at progressively longer distances from the IDT along the SAW propagation direction (Fig. 2.13(b)). The coarser appearance of the fingering fascinatingly corresponds to the broader, longer wavelength features of the Fresnel diffraction the further away the comparison is made from the IDT that generates the SAW. Curiously, and in further support of Fresnel diffraction as the mechanism responsible for driving the fingering instability, the finger spacing was found to be linearly dependent on the wavelength of the SAW, yet insensitive to changes in the SAW aperture and the 'gap' between the individual IDT finger tips and the adjacent bus bar (Fig. 2.14).

2.8 THICK FILMS: EFFECT OF ECKART STREAMING

Finally, we consider films or sessile drops that are sufficiently thick ($h \gg k_l^{-1}$) that Eckart streaming—the bulk vortical flow that arises as a result of the net volume force generated as the acoustic wave intensity in the liquid decays due to viscous dissipation or due to the attenuation of the SW—can no longer be neglected. As the film thickness increases beyond a critical value, Eckart streaming becomes the dominant flow within the film/drop, overwhelming the convective drift invoked by direct contact between the SW and the liquid that we have considered to this point, and consequently driving the film to spread or sessile

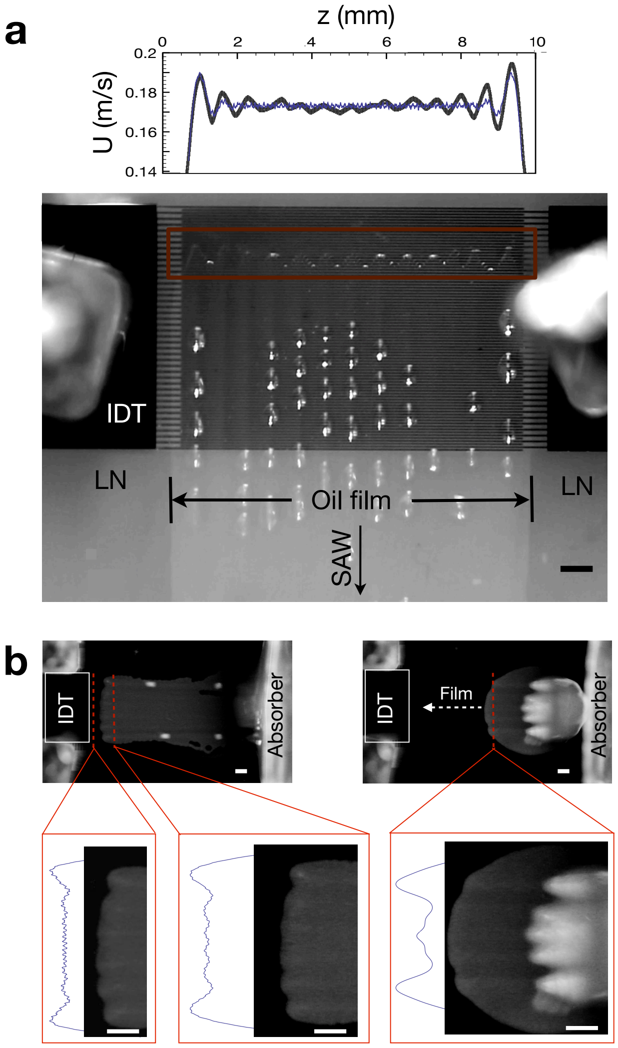

Figure 2.13: (a) Magnified image of the advancing film front showing the fingering instability triggered by transverse Fresnel diffraction of the underlying SAW directly above the IDT, as measured via a LDV scan of the substrate displacement beneath the fingers (see bold grey line in the inset above the image). Also shown by the thin blue line in the inset is the displacement predicted by the Fresnel diffraction model, which agrees well with the LDV results. The LDV data is provided as the root-mean-square displacement velocity amplitude U along the transverse z-direction. The scale bar denotes a length of ≈ 1 mm. (b) Similar images of the fingering patterns at positions λ_{SAW}, $10\lambda_{\mathrm{SAW}}$ and $35\lambda_{\mathrm{SAW}}$ (left to right) from the edge of the IDT, respectively, along the SAW propagation axis; λ_{SAW} is the SAW wavelength and the scale bars denote lengths of ≈ 1 mm. A magnified image of the finger patterns for each location is shown below together with the corresponding transverse displacement velocity amplitude U predicted by the Fresnel diffraction model, again showing good qualitative agreement.

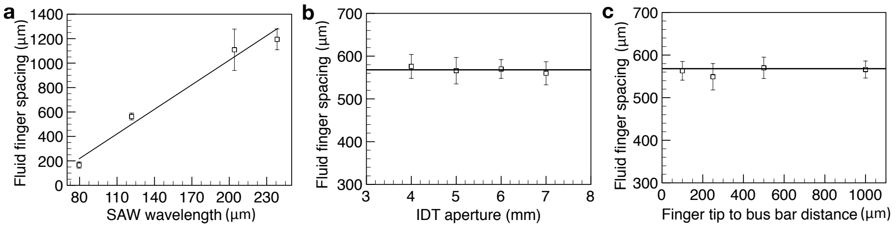

Figure 2.14: Dependence of the characteristic spacing of the fingering patterns on **a,** the SAW wavelength (and hence frequency), **b,** the IDT aperture, and, **c,** the 'gap' between the IDT finger tip and bus bar. The measurement is made when the advancing front of the film where the finger patterns develop reaches the middle of the IDT. When not varied, the SAW frequency, IDT aperture and distance between the IDT finger tip and bus bar are held constant at 32.7 MHz, 7 mm and 500 μm, respectively. It can be seen that the fluid finger spacing is almost linearly dependent ($R^2 = 0.98$) on the SAW wavelength but is independent of the IDT design. The error bars denote the standard error for $n = 10$ finger patterns for each point.

drops to translate in the direction of the SW propagation—that drops translate along the SW propagation direction under Eckart streaming is well known (see, for example, Tan et al. [191], Brunet et al. [28], Friend and Yeo [58]) and shown in Fig. 2.15.

As a first approximation to the acoustic beam, consisting of compressional acoustic waves that propagate through the liquid as energy from the attenuating SW leaks into the liquid, we consider an acoustic field in a half-space of liquid, generated by similar excitation to that in (4.1). Ignoring the viscous attenuation of the acoustic beam close to the substrate boundary, which is typically weak compared to the attenuation of the SW [181], this satisfies [31]

$$\begin{pmatrix} u_x \\ u_y \end{pmatrix}_{y>0} = \begin{pmatrix} U e^{i(t\omega+\varphi)-(\alpha+ik)(x+\xi y)} / \xi \\ U e^{i(t\omega+\varphi)-i(k-i\alpha)(x+\xi y)} \end{pmatrix}, \tag{2.57}$$

where $\xi = \left[(k_l/k)^2 - 1 \right]^{1/2}$. The dimensional volume force along the solid surface, i.e., along the x-coordinate, that is generated by the SW described by (2.57) can then be written as [181]

$$F_x = (\rho \mathbf{u} \cdot \nabla \mathbf{u} + \mathbf{u} \nabla \cdot \rho \mathbf{u}) \cdot \hat{\mathbf{x}} \approx \rho \alpha U^2 \left(\frac{1+\xi^2}{\xi^2} \right) + \mathcal{O}(\alpha k^{-1}), \tag{2.58}$$

where $\hat{\mathbf{x}}$ is the unit vector along x; here, both x and y are assumed to scale with k^{-1}. In search of the viscous volume flux associated with (2.58), we seek a solution for the streamfunction ψ_{E} that satisfies the no-slip boundary condition at the solid/liquid boundary $\partial_y \psi_{\mathrm{E}}|_{y=0} = 0$, the stress-free condition along the tangent to the free surface of the film $\partial_{yy}\psi_{\mathrm{E}}|_{y=0} = 0$, and a volume force F_x of the dimensional form $\partial_{yyy}\psi_{\mathrm{E}} = -F_x/\mu$. Dimensionally, this reads

$$\psi_{\mathrm{E}} = \frac{\alpha\left(\xi^2+1\right)\rho U^2 y^2(3h-y)}{6\mu\xi^2}. \tag{2.59}$$

The corresponding volume flux (also dimensional) is then

$$Q_{\mathrm{E}} = \frac{\alpha h^3\left(\xi^2+1\right)\rho U^2}{3\mu\xi^2}. \tag{2.60}$$

Equating the volume flux imposed by SW induced drift in §2.6, i.e., $Q \approx h\,(dx_1/dt)$ wherein dx_1/dt is obtained from the expression in (2.52), and for Eckart streaming in (2.60) then leads to

$$\left|\frac{Q}{Q_{\mathrm{E}}}\right| \approx \frac{3\chi}{4}\frac{\alpha^{-1}\beta^{-1}}{h^2}\left|\cos\varphi - \sin\varphi\right|\left|1-(k/k_l)^2\right|. \tag{2.61}$$

It is interesting to note that the volume flux ratio in (2.61) is independent of the SW velocity amplitude U. Further, we observe that h is naturally scaled by the mean of the viscous penetration length β^{-1}, which is the characteristic scaling for the viscous flow layer Rayleigh streaming invoked directly by the SW motion, and the SW attenuation length α^{-1}, which is the characteristic scaling for the Eckart streaming.

For Rayleigh SAWs where $\varphi = 3\pi/2$, requiring $|Q/Q_{\mathrm{E}}| < 1$ in (2.61) for Eckart streaming to dominate at the onset of the flow reversal ($h \sim \mathcal{H}_{c_2}$) and matching the parameter values used in the experiments, i.e., $\mu = 10^{-1}$ Pa·s, $\rho = 10^3$ kg/m^3, $U = 10^{-1}$ m/s, $\omega/k = 4\times10^3$ m/s, $\omega/k_l = 1.5\times10^3$ m/s, $\alpha = 10^3$ m^{-1}, $\chi \approx 1$ and $\omega/2\pi = 30\times10^6$ Hz, then leads to $\mathcal{H}_{c_2} \approx 90$ μm, which is in approximate order-of-magnitude agreement with the critical heights h_{c_2} obtained experimentally (Fig. 2.4(d) and later in Fig. 2.17.

2.9 SOLITON-LIKE WAVE EMERGENCE AND PROPAGATION

The finger formation is followed by the emergence of wave pulses (see Figs. 2.3(d) and (e) and 2.13(a), that, from Fig. 2.16, appear to grow mainly from the capillary ridges above the advancing film front and eventually translate away in the direction reverse to that of the film spreading (i.e., along the SAW propagation direction), exhibiting soliton-like behaviour and maintaining a constant volume. The dimensions of the wave pulses were found to be insensitive to the SAW power and fluid properties, only depending on the wavelength of the SAW. We attribute the initial growth of the film (Fig. 2.16(a) and (b) to the continued flow into the capillary ridge as the film spreading is arrested at a specific location along the IDT.

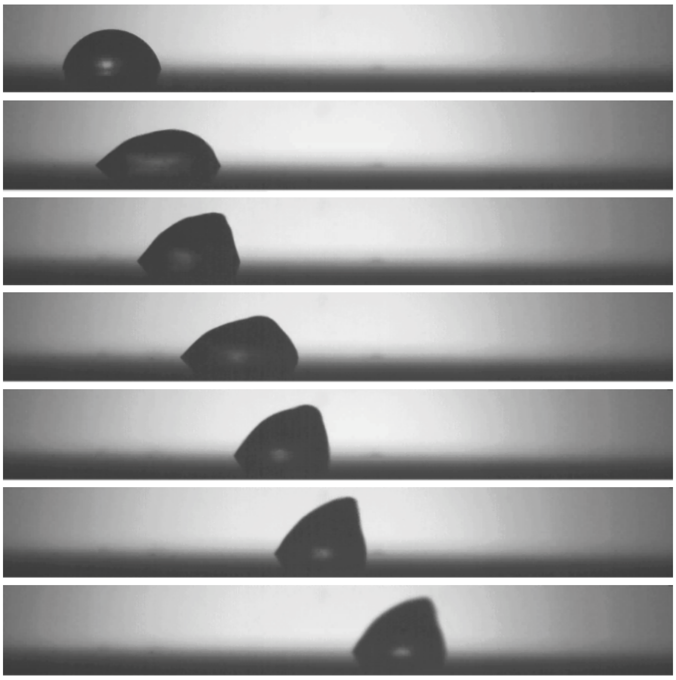

Figure 2.15: Snapshots for drop translation under Eckart dominant flow, where the drop dimension is many times larger the acoustic wavelength. Time difference between each image is 0.01s.

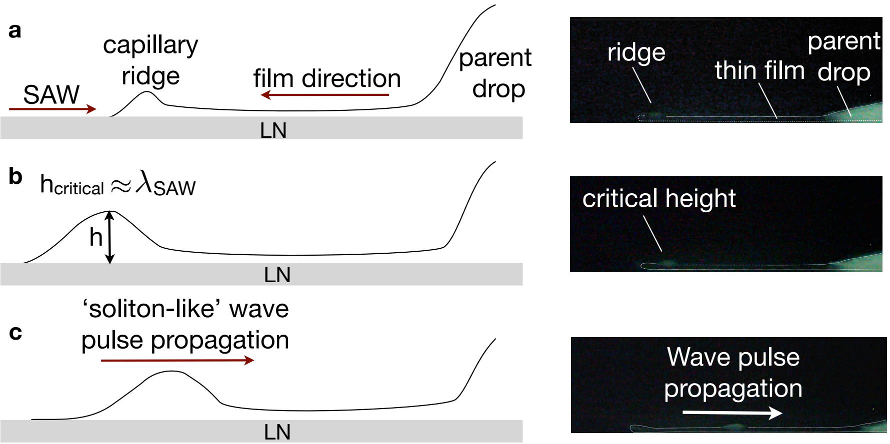

Figure 2.16: Schematic (left) and fluorescent images (right) showing **a,** the capillary ridge at the leading edge of the advancing film front pulled out from the parent drop in the direction opposing that of the SAW propagation. **b,** The capillary ridge subsequently grows when the film is prohibited from spreading further to form **c,** a 'soliton-like' wave pulse that propagates away in the direction opposite to that of the film spreading once the film height h reaches a threshold value $h_{\text{critical}} \approx \lambda_{\text{SAW}}$ at which point Eckart streaming begins to dominate; λ_{SAW} being the SAW wavelength. Dashed lines were added to aid visualisation of the thin film.

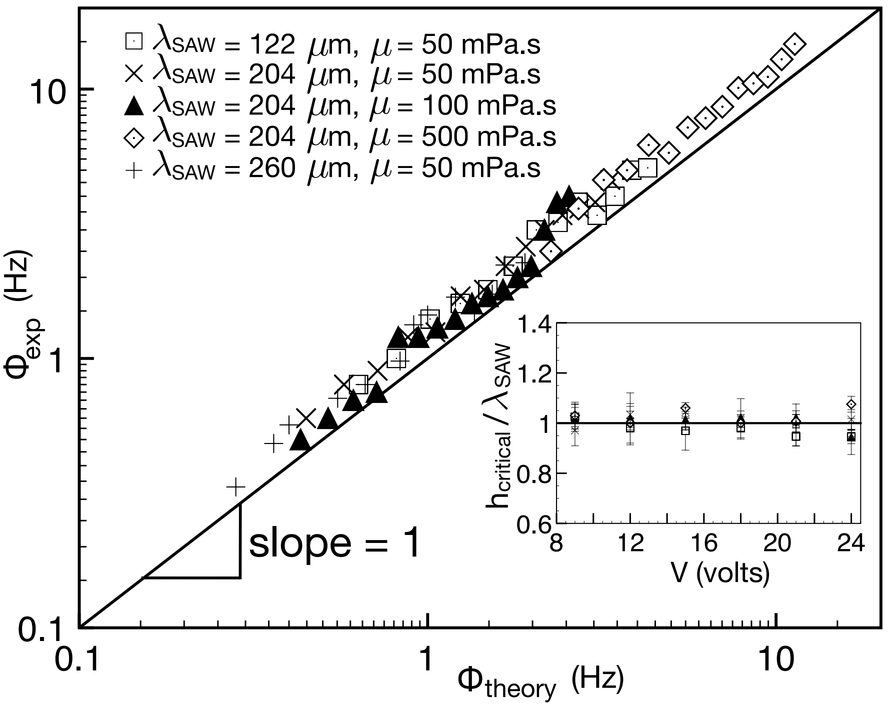

[H]

Figure 2.17: Comparison between the frequency Φ at which the wave pulses are generated, predicted by applying volume conservation across a control volume around the capillary ridge region, with experimentally measured data. The inset shows the critical height h_{critical} (normalised by the SAW wavelength λ_{SAW}) to which the capillary ridge (wave pulse) grows before it translates away under Eckart flow. This is measured as a function of the applied power for different frequencies and liquid viscosities. The error bars are the standard errors for $n = 5$ wave pulse size measurements for each point.

More specifically, the growth of the capillary ridge to form a solitary wave-like structure can be attributed to continued inflow into the nose of the film due to Rayleigh streaming, as long as the film front is prohibited from further spreading and as long as there is no mechanism for outflow away from the ridge region. The former occurs because the SAW is partially composed of a standing wave within the IDT and assumes a complete standing wave form at some location along the IDT. The latter is true as long as the height of the film and ridge remain sufficiently small such that the confinement provided by their thicknesses prohibit sufficient pathlength to attenuate the energy leaked into the fluid by the SAW to drive Eckart streaming. Given that the dominance of Rayleigh streaming over Eckart streaming begins to wane as the ridge (wave pulse) thickness h exceeds λ_l, it is reasonable to assume that the ridge (wave pulse) grows to this critical threshold height $h_{\text{critical}} \sim \lambda_{\text{SAW}} > \lambda_l$ before being transported away in the opposing direction due to the now dominant Eckart flow. This is verified by experimental measurements of h_{critical}, which appear to strongly correspond to λ_{SAW} irrespective of the viscosity, frequency, or input voltage (see Fig. 2.17 inset).

Volume conservation applied over a control volume around the capillary ridge region then permits an estimation of the rate at which these wave pulses appear since the rate at which each capillary ridge (wave pulse) height grows must equal the volumetric inflow rate into the capillary ridge region. Given that the latter can be estimated from the velocity (equation (2.53)) and film thickness (≈ 20 μm), the rate at which these wave pulses are generated can then be predicted if it is assumed that the capillary ridge grows to h_{critical} before translating away. The close agreement in Fig. 2.17 not only verifies the postulated reason for the existence and transport of the wave pulses but also supports the proposed mechanism underpinning the spreading dynamics which forms the basis on which equation (2.53) is derived.

2.10 CONCLUDING REMARKS

In this work, we have derived a generalised model that governs the dynamic spreading behaviour of liquid films on substrates under high frequency (MHz order) vibration in the form of propagating SWs. In contrast to low frequency (Hz to kHz order) excitation, the viscous penetration length β^{-1}, which scales inversely with one half the excitation frequency, becomes sufficiently thin at high frequencies, to the point at which it is then effectively comparable to the capillary–molecular length scale characteristic of the contact line region such that it exerts a considerable influence on the contact angle, thus triggering the spreading of the film. In particular, the film spreading is driven by the invocation of a dominant viscous periodic flow, which supports a weak convective and steady contribution in the form of a confined Reynolds stress that may translate into an effective surface force or an equivalent convective drift near the contact line region. In fact, the role of β^{-1} is prevalent and appears throughout the expressions governing the spreading in various cases, be it in the point surface force that arises due to the coarse-grained Reynolds stress on the interface in the case of low surface energy substrates where the initial contact angles are large [126], or in the velocity of the advancing front in (2.52) for films of intermediate thicknesses on high surface energy substrates [162]: the smaller the value of β^{-1} as the excitation frequency is increased, the larger the force or the velocity. Both directionality and phase of the substrate excitation are also found to play an important role, influencing the direction along which the film spreads: spatially-isotropic vibration on the substrate was found to render axisymmetric spreading in all directions whereas directionally-propagating SWs were found to render spreading along a specific direction, influenced by the phase of the SW between its longitudinal and transverse component.

The diversity of height scales that a liquid body can assume relative to the viscous penetration length β^{-1} then yields various scenarios for the spreading film as uncovered in recent experiments. This is captured through the generalised film spreading equation derived in (2.24), particularly for thin and intermediate films whose spreading is solely due to the convective drift generated by the dominant viscous periodic flow arising directly from the interaction of the undulating substrate boundary as the SW traverses it with the liquid in the film immediately adjacent to the substrate over a length scale described by the viscous penetration length β^{-1}. For sufficiently thin films ($h \sim \beta^{-1} \ll k_l^{-1}$) which are not able to support the propagation of acoustic waves into the liquid due to the leakage of SW energy from the substrate, the acoustic radiation pressure acting on the interface is negligible; the convective drift generated by this dominant viscous periodic flow described by (2.28) is then the primary mechanism that drives the spreading of these thin films in the same direction of the drift, which, in turn, is along the propagation direction of the SW for the case of Rayleigh SAWs. In the inertial limit in which the convective drift dominates the film dynamics over capillary effects, the film is observed to spread self-similarly as $t^{1/4}$, consistent with that observed in the experiments. Films of intermediate thicknesses ($hk_l^{-1} \gg \beta^{-1}$), on the other hand, permit the leakage of the SW energy from the substrate to produce acoustic waves in the liquid, and are therefore influenced by an additional stress mechanism, namely, the acoustic radiation pressure, leading to stable and unstable films (or regions within a film), in addition to the drift flow, which together, impose a volume flux that causes the film to spread with constant velocity according to (2.52) in the opposing direction to that of the drift, and, in the case of Rayleigh SAWs, opposite to the SW propagation direction, consistent with that observed experimentally. For thick films and sessile drops whose characteristic thickness $h \gg k_l^{-1}$ is sufficient to permit an adequate path length for the viscous attenuation of the acoustic wave generated in the liquid through leakage of the SW energy from the substrate, long-range vortical Eckart streaming dominates and drives the film/drop to translate in the direction of the SW propagation. As such, two critical film thicknesses exist, associated with the transitions at which the film spreading reverses its direction as the film thickness is increased beyond the range over which each phenomenon dominates.

3

FLUID PUMPING AND MIXING ON PAPER-BASED MICROFLUIDICS DRIVEN BY SAW

Our thorough understanding of films and how different streaming phenomena dominate at different length scales is implemented here in the use of Eckart streaming — which dominates at fluid length scale larger than λ_{SAW} — to drive atomisation at a paper-based microchannel's tip, which in turn pulls and mixes fluids along a Y-channel structure. The mixing induced by the 30 MHz acoustic waves is shown to be consistent and rapid, overcoming several limitations associated with its capillary-driven passive mixing counterpart wherein irreproducibilities and nonuniformities are encountered in the mixing along the channel. Capillary-driven passive mixing offers only poor control, is strongly dependent on the paper's texture and fibre alignment, and permits backflow, all due to the scale of the fibres being significant in comparison to the length scales of the features in a microfluidic system. Using a novel hue-based colourimetric technique, the mixing speed and efficiency is compared between the two methods, and used to assess the effects of changing the input power, channel tortuousity and fibre/flow alignment for the acoustically-driven mixing. The hue-based technique offers several advantages over grayscale pixel intensity analysis techniques in facilitating quantification without limitations on the colour contrast of the samples, and can be used, for example, for quantification in on-chip immunochromatographic assays.

3.1 INTRODUCTION

The increasing costs of in-patient healthcare compounded by the chronic shortage of medical professionals in many developed nations underlie a need to shift diagnosis from the hospital to the patient at home or in the physician's office to facilitate prevention or early detection and timely treatment of disease. Widespread implementation of point-of-care testing, however, requires portable, inexpensive and reliable diagnostic technologies for which microfluidics has become a key area of research[223]. Nevertheless, few microfluidic diagnostic devices have been commercially successful, due to their complexity, difficulty in integration, and especially the cost of producing them in large quantities. Paper-based microfluidics offer an exciting alternative to standard polymer and integrated circuit substrate materials, potentially lowering the mass production costs of even complex microfluidics devices to serve the needs of healthcare systems in developed nations, and perhaps even to the point where the technology becomes an affordable solution to the unfortunate lack of even basic medical equipment or medical expertise in developing nations [216, 133].

In their simplest form, paper-based microfluidic diagnostics are based on lateral flow immunochromatographic assays (a well-known example being the home pregnancy test strip) where the physiological sample is drawn through a paper strip via capillary action to regions where antibodies specific to the detection protocol are immobilised. An absorbent pad placed at the waste end of the strip is often used to aid in drawing sufficient volume of the sample across the antibodies. Creative microfabrication and microfluidic strategies have recently been proposed to advance this simple technology beyond the one-dimensional lateral flow strip to allow for multiplex operation or multianalyte detection and to enhance detection sensitivity and quantification, whilst minimising the costs associated with producing these test kits [130, 1, 129, 53, 61, 62].

The ability to use paper in place of soft lithography polymer materials and especially silicon, glass and other such materials typically employed for integrated circuit fabrication is justifiable on more than cost alone, given the convenience of working with it. Hydrodynamic focusing, dilution, mixing and separation schemes have been developed that employ capillary wetting, an attractively simple transport mechanism that eliminates the pumps and active mixing devices typical of standard microfluidics[151].

Unfortunately, capillary wetting offers only rudimentary control over these processes. Moreover, irregularities in the porosity as well as the anisotropy and irregularity of the fibre orientation and length in paper altogether leads to nonuniformity and unpredictability in the capillary flow through the paper compared to flow in channels made from silicon, glass, or polymers in conventional microfluidic devices, especially for dynamic operation. When controllability and uniformity of the flow are important, an alternative to capillary flow is worth considering: active transport mechanisms through external forcing, e.g., with electric or acoustic fields [183, 223]. Whilst the introduction of such microfluidic actuation schemes appears contrary to the principle of simplicity and the inexpensive nature of paper-based devices, the advantages of controllability and uniformity help offset this concern, especially given recent developments in surface acoustic wave (SAW) microfluidic transport [222, 58, 204] that may be driven by inexpensive, miniature battery-powered circuits (see, for example, Ref. [157]) which can thus be integrated with the paper-based device.

In particular, SAWs have been shown to provide a useful means to extract bioanalyte molecules from paper substrates via atomisation for further analysis [158], for example, using mass spectrometry [76, 77]. Whilst this work focussed on the *post-atomisation* integrity of the molecular structures as they are transported through and *out* of the paper network [158, 77], we demonstrate here the possibility of extending the fast atomisation-induced fluid transport through paper to facilitate uniform mixing of two fluids *within* the paper structure, in particular, for the purpose of enabling low cost point-of-care paper-based diagnostics in a portable integrated device. Although the method is reminiscent of evaporative-driven transport inspired by transpiration in plants [142], atomisation[156] does not rely on phase change, which is difficult to control and often requires stringent temperature regulation [226], which can be costly and impractical in paper-based microfluidic devices. Moreover, the flow velocities generated using SAW atomisation, even in paper-based channels, are at least one to two orders of magnitude larger than the ultra-low flows in evaporative-driven transport in microfluidic channels or passive capillary-driven flows through paper channels. Further, the SAW mechanism is shown in this work to promote fast, uniform and consistent mixing in paper networks compared to that obtained via capillary action.

In quantifying the mixing performance, we introduce an alternative colourimetric technique employing the hue instead of the intensity (or brightness), enabling the use of multiple colours in a manner not possible with traditional methods that employ grayscale [115, 185, 93] or a specific colour channel, for example, the red component of the RGB colour space [30]. In addition, the method provides the ability to dynamically track the progression of the colour change both in space and time without requiring a large colour contrast as is required using grayscale analysis. Moreover, in contrast to grayscale methods which are based on intensity and hence sensitive to the illumination consistency across runs, the hue method is robust under different lighting conditions through normalisation by exploiting the property that hue values vary linearly with the colour scale. This also allows the method to easily be extended to include more than two colours. Finally, this quantitative technique can be employed to provide quantitative analysis and hence extend currently available immunochromatographic assays that are, at present, limited to visual qualitative tests [135], such as the duplex test for influenza type A and type B antigens and triplex tests for HIV–1 and hepatitis B and C viruses [44].

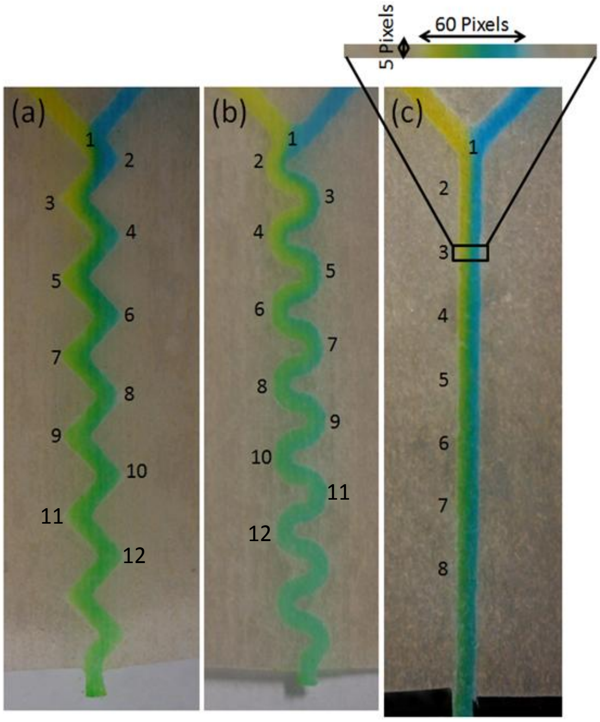

Figure 3.1: Different channel branch configurations and the mixing effect within: (a) zigzag , (b) curved, and (c) straight. The numeric labels indicate the locations at which the quantification is carried out.

3.2 MATERIALS AND METHODS

3.2.1 *Paper Channels*

Y-shaped flow channels with two inlets merged to form a single outlet channel were created in paper using a similar protocol to FLASH (Fast Lithographic Activation of Sheets) [131]. The outlet channel was either patterned as a straight, curved in a serpentine fashion, or fabricated in a zigzag pattern with straight-line sections joined by sharp corners, as shown in Fig. 3.1. First, polyester-cellulose clean room paper (Lym-Tech, Chicopee, MA, USA) was soaked into a photoresist mixture (56.3% by volume SU8–25 + 37.5% by volume PGMEA + 6.2% by volume triarylsulfonium hexafluorophosphate salts (photoacid)) for 20–30 minutes to allow the paper to fully absorb the photoresist. After removing the paper from the solution and draining off excess photoresist, the paper was baked at 70°C for several minutes until a semi-dry surface was obtained. The paper was then covered with an inexpensive polyester plastic film photomask for negative tone exposure (the channels were black at 4000 DPI resolution), exposed to UV flood lighting for 30 minutes and subsequently baked for 5–6 minutes until the surface became dry. The unexposed regions of the photoresist were then removed from the paper by immersing it in acetone for 1–2 minutes.

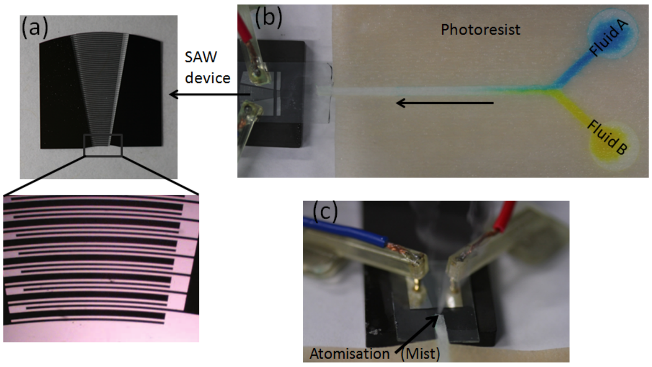

Figure 3.2: (a) Image of the focused SPUDT across which an oscillating RF signal is applied to generate the SAWs that act to draw flow through the paper microfluidics device. (b) The end of the flow channel at the edge of the paper is placed at the focal point of the SAW such that (c) the atomisation of the fluid out of the channel at the paper edge draws liquid through the Y-channel from its two reservoirs.

Although a variety of channel widths can be patterned, we demonstrate the technique with 2-mm wide channels. Narrower channels improve mixing, though at the cost of our ability to quantify the mixing—as the colour is assessed across the width of the channel in our structure that stretches over a length of 5 cm, even high resolution cameras are unable to accurately resolve the mixing with channels 1 mm in width or narrower whilst maintaining a field of view that encompasses the entire channel length. Though it is possible to zoom in to particular locations or use several cameras, the speed of the flow under certain conditions and the simple aim of the study in comparing behaviour between capillary- and SAW-driven mixing both suggest that, for now, a simple approach is best. Fluids were introduced onto the paper by first horizontally suspending two pippettes, each containing 10 $\mu\ell$ of coloured dye. To ensure that equivolumes of both fluids were deposited onto the paper at approximately the same time and location in both reservoirs, the pipette tips were then placed just above the paper surface and the plungers simultaneously pushed with equal displacements using a flat backing piece that spanned both plungers.

3.2.2 *SAW Device*

Using standard UV lithography, chromium–aluminium elliptical SPUDT electrodes were patterned on a 127.86^o y-x rotated single crystal lithium niobate (LN) piezoelectric substrate (Fig. 4.9(a)) [222]. The gap and width of the interleaving electrode fingers were patterned to produce focused SAWs with 132 μm wavelengths, corresponding to a resonant frequency of 30 MHz. Applying a sinusoidal electrical signal at this frequency then generates a Rayleigh SAW propagating from the SPUDT towards a focal point on the substrate. The end of the paper channel is placed at this point (Fig. 4.9(b)). As depicted in Fig. 4.9(c), the fluid in the paper channel is drawn out to form a meniscus which subsequently atomises at the edge of the LN substrate, thereby resulting in a negative pressure gradient that draws fluid through the channel. For this method to work best in the paper microfluidics application, the channel structure must be pre-wetted. In the case of aqueous reagents, the channel can be pre-wetted using organic liquids given that these can still be atomised using the SAW.

3.2.3 *Colourimetric Analysis*

Fluid mixing in microchannels is commonly quantified using grayscale techniques, either involving the standard deviation from a reference value or the mean value of the pixel intensity [115, 144]. Both methods, however, require two fluids with a strong contrast in intensity between them—in other words, the grayscale technique works best when one fluid is bright and the other is dark in intensity in response to transmitted or reflected light. This often means that one fluid needs to be fluorescent and the other colourless to enable good quantification of their mixing. What this typically means is that the analysis is not just limited to the mixing of two fluids—the limitation also extends to the type of fluids that can be used since a colour difference between the fluids alone is rarely sufficient for quantification. Moreover, such limitation in grayscale techniques also place severe restrictions on the quantification of immunochromatographic assays in practical diagnostic tests, and the detection of most colour *changes* in chemical reactions.

To the best of our knowledge, only one colourimetric technique has been proposed to date for quantifying the mixing intensity[30]. In this technique, the red component of the RGB colour space was used to quantify the mixing of a small quantity of red dye agitated in a transparent fluid container. As with grayscale models, this technique is limited to two fluids, one with a primary colour (red, green or blue) and the other colourless. Often, however, the analysis is restricted to the samples that are to be assessed and hence the choice of colour (or absence of colour, for that matter) is not always available, especially in practical diagnostic assays that may exhibit changes in colours over time or location without significant change in intensity.

To circumvent these limitations, we propose the *hue* as an independent means to quantify mixing. Every colour, independent of intensity (and hence the method and consistency of illumination), has a base hue value (see the colour bar in Fig. S1 in the ESI). As the colour shade varies upon mixing, the hue values change correspondingly and can be tracked both spatially and temporally. For simplicity and to demonstrate the concept, we mix two aqueous solutions of different coloured food dyes from two separate reservoirs as they are drawn from the side Y-branches connecting the reservoirs into a single channel with the SAW. One reservoir contained a blue solution with hue $H_{\text{blue}} \approx 210$ and the other contained a yellow solution with hue $H_{\text{yellow}} \approx 50$, such that they form a green solution with a hue value $H_{\text{green}} \approx 130$ when mixed in equal amounts and concentrations. More specifically, upon mixing two 10 $\mu\ell$ drops of the two coloured solutions, the hue changes to a value described fairly well by linear interpolation between the hues of the original solutions, using the ratio of the blue and yellow dye concentrations 3.3.

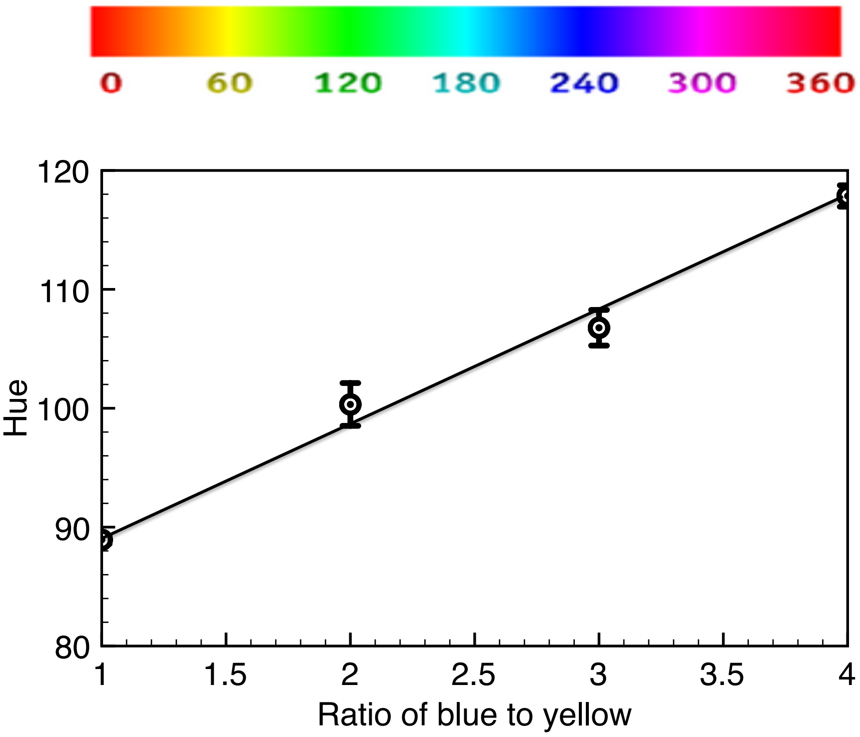

Figure 3.3: Hue values for different colours (top) and that of a mixture of two 10 $\mu\ell$ drops containing varying concentrations of blue and yellow dye (bottom). The data was linearly fitted with $R^2 = 0.989$ ($n = 5$).

A digital SLR camera (EOS 550D, Canon, Utsnomiya, Japan) fitted with a macro lens (EF-S, 60 mm focal length, F/2.8, Canon, Utsnomiya, Japan) for high resolution imaging was used to photograph the fluid channel region in 0.5 second intervals, as shown in Fig. 3.1. Each image was processed to recover channel cross-sections 60 pixels wide by 5 pixels tall at specific locations along the channel's path length, taking into account their tortuousity. The hue values of the pixels were *normalised* as follows:

$$H_{\text{blue/yellow}} = \frac{H - H_{\text{green}}}{H_{\text{blue/yellow}} - H_{\text{green}}}; \tag{3.1}$$

a *mixing index* can then be obtained by averaging this normalised hue value over the 300 pixels in each channel cross-section at steady-state. Each run was performed three times to assess the variability in the results; the reported data is thus the statistical result of all three runs. Due to the way the normalisation is performed, either unmixed blue or yellow will give a normalised hue value of 1, while a fully mixed combination of equal parts of blue and yellow to give green will result in a normalised hue value of 0. For each of the positions along the microfluidic path, the average normalised hue value can also be determined as a function of time, as shown in Fig. 3.4 for the curved channel in Fig. 3.1(b).

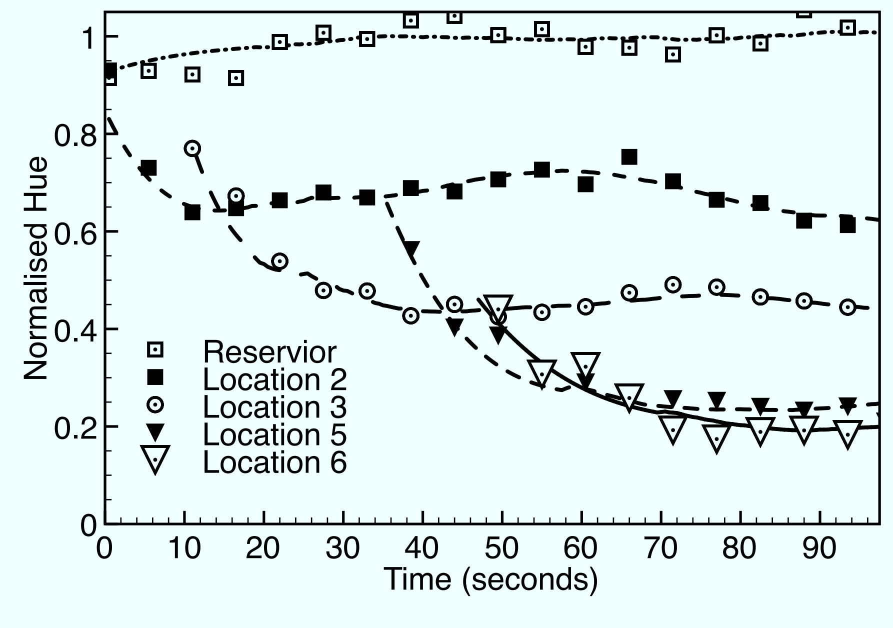

Figure 3.4: Mixing intensity (the normalised hue value given in averaged across the pixels in a cross-section of the channel at several predetermined locations) as a function of time for the curved channel shown in Fig. 3.1(b). The normalised value of the fully unmixed (blue or yellow) states is 1 and approximately 0 for the fully mixed (green) state. We note that there is a slight increase in the hue value at the beginning of the experiment due to the initial filling of the channel; the steady hue values in the reservoirs, on the other hand, are accounted for in the normalisation of Eq. (3.1).

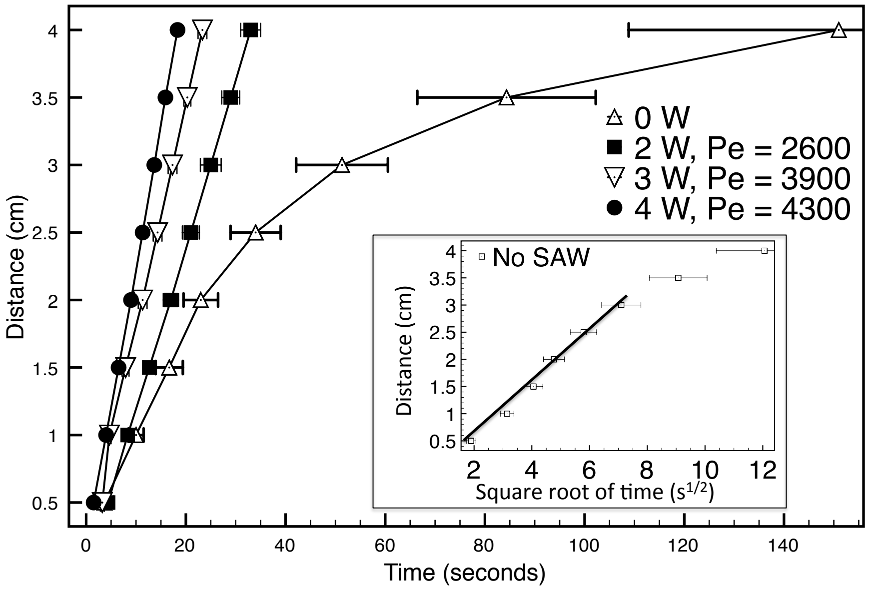

Figure 3.5: A comparison of the wetting speed through the paper channel for capillary- and SAW-driven transport (with various input power levels) indicates the nearly constant velocity flow induced by the SAW and the recovery of the Washburn model prediction for capillary-driven fluid transport. The former is substantially faster for channels longer than about 2 cm. The inset shows a rescaling of the data for the capillary-driven flow (0 W), indicating that the flow eventually slows beyond the predicted rate of the Washburn model due to evaporation.

3.3 RESULTS AND DISCUSSION

3.3.1 *SAW-Driven Flow Compared to Capillary-Driven Flow*

Figure 3.5 shows a comparison between the wetting speeds due to pure capillary action in which fluid is *pushed* through the channel and that due to the SAW in which fluid is *pulled* through the channel. It is clear that the mechanism by which fluid is transported along the paper channel using SAW is somewhat different to capillary imbibition through the paper pores, predicted by the Washburn scaling $x \sim t^{1/2}$ (x being the length along the channel traversed by the advancing fluid front and t being time)[205, 153, 63] that arises from a balance between the viscous and capillary stresses that dominate the flow behaviour. Over longer periods of time, evaporation causes the flow to deviate from the Washburn model, as shown in the inset of Fig. 3.5—such behaviour was also observed elsewhere.[11] In contrast, the negative pressure gradient generated within the paper channel due to the SAW atomisation at the edge of the channel drives flow within the channel which can be characterised by a balance between the dynamic pressure and capillary stress, yielding $x \sim t$ in agreement with the linear response exhibited in Fig. 3.5. This indicates a dominant convective mechanism in which fluid is transported *over* the paper surface rather than *through* the pores of the paper. It is worth emphasising that the above mentioned linear scaling with SAW is valid even when longer channels are employed due to the constant atomisation rate which is the mechanism that drives the flow within the channels.

The SAW-driven convective transport of the fluid over the paper nevertheless provides more than merely higher flow speeds (and hence reduced assay times, thereby reducing problems due to evaporation and dryout in paper-based assays). The SAW-driven flow is observed to be more uniform and predictable compared to its capillary-driven counterpart, in which inconsistencies in the flow behaviour are commonly observed due to irregularities in the fibre alignment and length—the source of the large error bars in Fig. 3.5 and the poor behaviour observed in the mixing experiments we describe below (see, for example, Fig. 3.6(a))—this despite the higher quality and more expensive clean room paper used in this study. Even if the fibre orientation could be controlled, the scale of the fibres is significant in comparison to most *micro*fluidic structures, and anisotropy exists in the wetting characteristics between the direction along the fibres to across them, both of which also lead to irregularity in the flow.

Another advantage of SAW transport is the elimination of backflow, where capillary flow from one inlet reservoir travels down to the Y-junction and both down the outlet leg as well as up the inlet leg of the other reservoir (Fig. 3.6(b)). This can occur if a fluid is not present at the Y-junction or if there is an imbalance between the capillary pressures of the two fluids. Such backflows can significantly affect the downstream channel behaviour (and hence the mixing in the experiments to be described subsequently), where one fluid reaches the junction before the other, causing a partial blockage in which the section of the channel available for the second fluid to flow is reduced (Fig. 3.6(a)). Backflow can also lead to wastage, which is a concern if expensive reagents or samples are involved.

3.3.2 *Mixing Performance*

These undesirable effects in capillary-driven flow translate to irregularities when mixing is attempted in paper microfluidics. The image at 40 s in Fig. 3.6(a) illustrates the effect of one Y-branch of the channel being partially blocked by fluid from the other Y-branch due to backflow as a consequence of an imbalance of the capillary pressure between both reservoirs (we note that this effect appears to be random and cannot be attributed to the faster mobility of, in this case, the blue dye in the paper over the yellow dye—reversing the dyes resulted

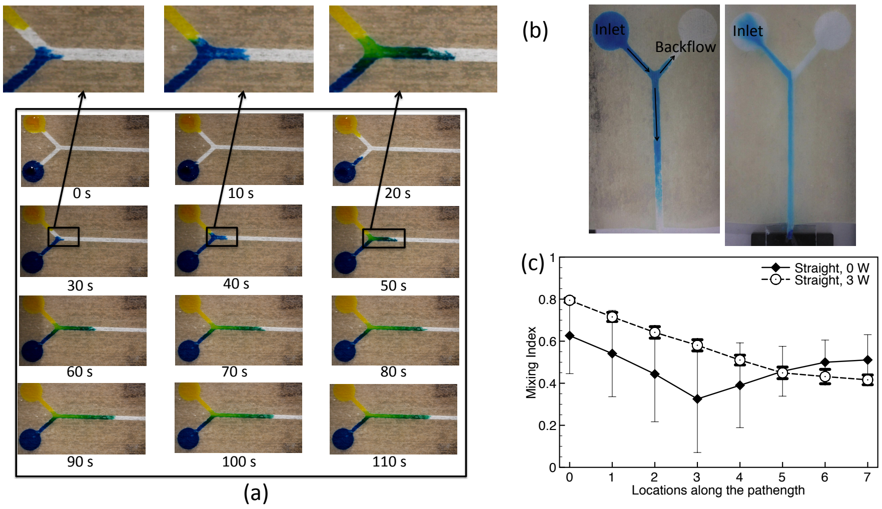

Figure 3.6: (a) Time series of images showing the mixing of two coloured solutions in a straight Y-channel (Fig. 3.1(c)) when driven by pure capillary wetting through the paper. The enlarged images above show an example of backflow of one solution from one Y-branch into another due to the imbalance of capillary pressures between the two reservoirs. As a consequence, the capillary wetting front suffers from irregularities and the subsequent mixing appears to be nonuniform. Good mixing is observed at the Y-junction but deteriorates downstream due to wetting irregularities and blockages in the flow. The mixing index in panel (c) quantifies this behaviour. (b) Capillary-driven fluid transport showing backflow arising when a fluid is placed in one inlet (left), while transport using the SAW pulls the fluid from the inlet towards the outlet without backflow (right). It is worthwhile noting that three times as much volume of the sample fluid had to be placed in the capillary-driven system to fill the identically sized channel to the same extent. (c) Comparison of the mixing performance between capillary and SAW-driven flows in the straight channel. The large error bars for capillary-driven mixing arise due to poor repeatability, a consequence of the paper's nonuniformity.

in equally random behaviour, which arises due to the irregularities in the paper structure). We observe not only the advancing front to be irregular but also the mixing to be erratic and nonuniform along the channel length. Good mixing is observed to appear, for example, at the junction where the branches intersect followed by poorer mixing downstream in the straight channel. The mixing performance thereafter recovers at some downstream location only to deteriorate once again. The mixing nonuniformity can be more clearly seen in the large error bars as well as the dip (location 4) and subsequent rise in the mixing index associated with the data for capillary-driven mixing (0 W) in Fig. 3.6(c). The large variation in the data arises as a consequence of inconsistent runs. In comparison, the mixing in the same straight channel (Fig. 3.1(c)) generated by the SAW appears to be considerably more uniform, with little variation in the mixing intensity for each of the measured locations from run to run. Such repeatability in the results can often be an important consideration in practical diagnostic devices, especially for quantitative tests, and hence the advantage of using the SAW to achieve such repeatability could in these circumstances outweigh the cost of the inclusion of an active transport mechanism.

In addition to more uniform and predictable mixing, we also note enhancement in the mixing performance. This can be seen more evidently by comparing the transverse concentration profile across the paper channel with that predicted by a steady convective-diffusive model, which, in dimensionless form, reads

$$\mathrm{Pe}\frac{\partial c^*}{\partial x^*} = \frac{\partial^2 c^*}{\partial x^{*2}} + \frac{\partial^2 c^*}{\partial y^{*2}}, \tag{3.2}$$

wherein the asterisks (*) denote dimensionless quantities: the axial and transverse coordinates are scaled with the channel width, i.e., $(x^*, y^*) \equiv (x, y)/W$, and the concentration is scaled with the initial concentration, i.e., $c^* \equiv c/c_o$. In this case, we take c to be the concentration of the blue dye; c_o is hence the concentration in the reservoir. Pe $\equiv UW/D$ is the Péclet number, which captures the relative contributions between convective and diffusive transport. D is the diffusivity and U is the average velocity at which the SAW pulls the fluid through the channel, which, from Fig. 3.5 can be assumed constant; from our experimental observations, it is also not unreasonable to assume that U is uniform across the channel cross-section. At the inlet to the straight channel $x^* = 0$, the initial unmixed condition requires $c^* = 1$ for $0 \leq y^* < 0.5$ and $c^* = 0$ for $0.5 \leq y^* \leq 1$, whereas a no-flux condition $\partial c^*/\partial x^* = 0$ can be imposed at the outlet ($x^* \to \infty$, $0 \leq y^* \leq 1$). Further, we assume that the channel sidewalls are impermeable, i.e., $\partial c^*/\partial y^* = 0$ at $y^* = 0, 1$ for all x^*. Equation (3.2), subject to these boundary conditions, has an analytical solution of the form[213]

$$c^*(x^*, y^*) = 0.5 + \frac{2}{\pi}\sum_{n=1}^{\infty}\frac{\sin\,(n\pi/2)}{n}\cos(n\pi y^*) \exp\left(-\frac{2n^2\pi^2 x^*}{\mathrm{Pe} + \sqrt{\mathrm{Pe}^2 + 4n^2\pi^2}}\right). \tag{3.3}$$

Figure. 3.7 shows the concentration profile predicted by Eq. (3.3) and that obtained from the experiment for an input power of 2 W, which given $U = 1.33 \times 10^{-3}$ m/s, $W = 2$ mm and $D_o = 10^{-9}$ m^2/s, corresponds to Pe = 2600, at a representative location along the channel length; here, we take the position roughly corresponding to the middle of the channel length, $x^* = 10$. It can be seen that the theory considerably underpredicts the mixing compared to the experimental profile at the same location. It is nevertheless possible to capture, at least approximately, the mixing enhancement of the SAW-driven transport above that given by the standard convective-diffusive model using an effective diffusivity, D_{eff}—we observe that the analytical and experimental concentration profiles appear to roughly match when $D_{\text{eff}} = 10D_o$, corresponding to a tenfold decrease in the Péclet number (Pe_{eff} = 260).

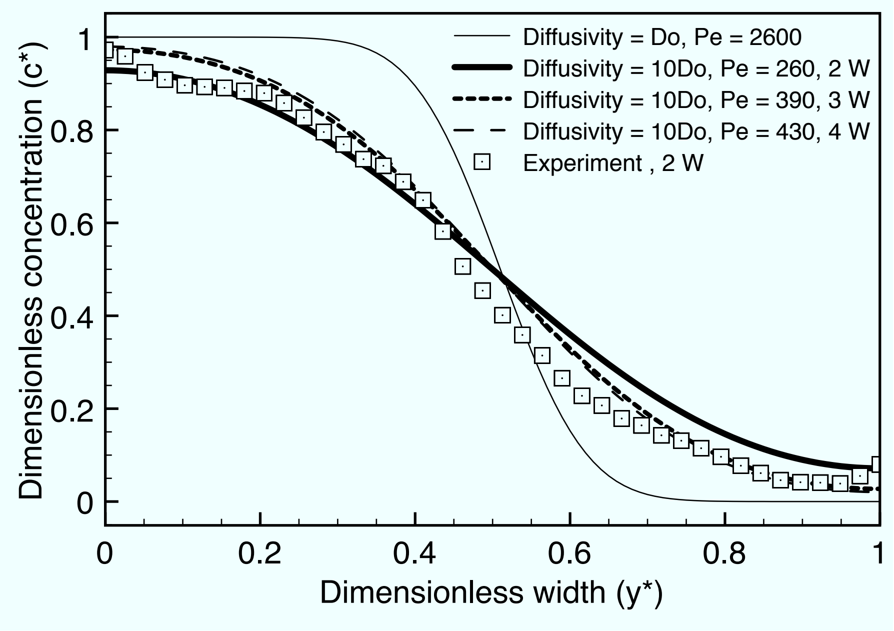

Figure 3.7: Comparison of the transverse concentration profile predicted by the standard convective-diffusive model (solid line) with that observed in the experiment (points) at a representative midpoint location along the channel $x^* = 10$. At a power of 2 W, the experimentally determined SAW-driven flow velocity U is 1.33×10^{-3} m/s in the 2 mm wide channel, corresponding to Pe = 2600. We note that the analytical prediction significantly underpredicts the mixing. To roughly quantify the mixing enhancement, we match the experimental concentration profile to the analytical solution with a modified Péclet number Pe_{eff}, which essentially corresponds to an effective diffusion coefficient D_{eff}. It can be seen that the experimental and analytical (bold solid line) profiles roughly match with a tenfold increase in the diffusivity, i.e., $D_{\text{eff}} = 10D_o$, and hence an order of magnitude decrease in Pe, i.e., $\text{Pe}_{\text{eff}} = 260$. Also shown by the dotted and dashed lines is the effect of increasing the input power of the SAW (associated with a corresponding increase in the flow velocity U), captured through an effective Péclet number in the analytical solution. In any case, the similar shaped trends between the experimental and analytical concentration profiles suggest that the mixing in the paper takes place through diffusion between the two laminar streams although we note that the interface between the streams is located at a slightly offset from the middle of the channel $y^* = 0.5$ due to slight irregularities along the paper surface.

Whilst the similar exponential trends for the analytical and experimental transverse concentration profiles indicate that the mixing in the paper channels indeed occurs via diffusion between the laminar

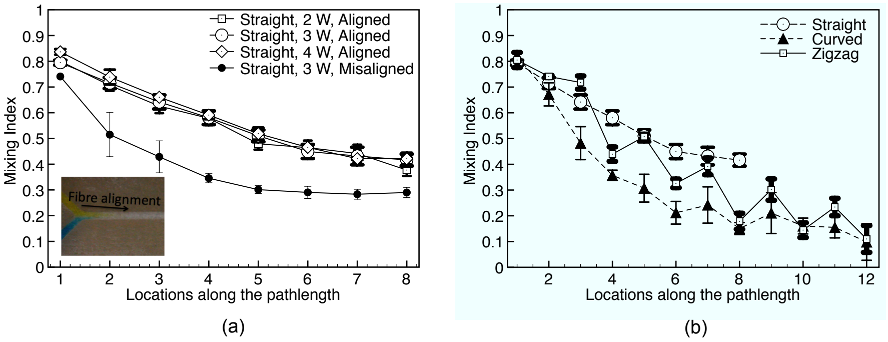

(a) (b)

Figure 3.8: (a) Effect of the input power and flow/fibre alignment on mixing performance. The inset shows the direction of the flow with respect to the fibre orientation. (b) Comparison of the mixing performance between the straight, curved and zigzag channels shown in Fig. 3.1. The straight channel gave the poorest mixing performance, taking into account the different path lengths, whilst the curved channel provides the best mixing, albeit with some minor handedness effects due to the asymmetry of the junction where the Y-branches intersect.

streams, we note that the mixing enhancement does not arise directly due to the SAW-driven convective transport along the channel (Section 3.3.1). In contrast to fast and chaotic mixing driven by SAW convection in a *sessile drop* [108, 179, 60, 120], we observe little effect of increasing the input power to the SAW (corresponding to an increase in the speed at which fluid is transported along the paper channel (Fig. 3.5) and hence the Péclet number) on the mixing performance, as seen in Fig. 3.8(a). This is confirmed by the analytical prediction in Fig. 3.7, which shows little change in the concentration profiles, for an increase in the effective Péclet number from 260 to 430 to account for the higher flow velocity as the power is increased. In fact, the faster flow leads to a slight deterioration in the mixing performance due to the reduced residence time of the fluid in the paper. The mixing enhancement also cannot be due to increased interfacial area of contact for mixing as no significant changes to the interface between the two parallel laminar streams was observed.

Another mechanism must therefore be responsible for the mixing enhancement captured through the effective diffusivity above: the obstruction to the flow posed by the paper fibres over which the fluid has to be transported—a paper analogue of the flow structures patterned in microchannels (e.g., grooves [185], slants[91] or obstacles[202]) designed to break the laminarity of the flow. This mechanism becomes clearly evident when we deliberately drive the flow at an angle to the fibre orientation (see inset of Fig. 3.8(a)) wherein the misalignment between the channel (and hence flow direction) and the fibre orientation is observed to lead to further improvement in the mixing performance, as seen in Fig. 3.8(a). This is in sharp contrast to capillary-driven flow where the fibre orientation actually governs the direction in which the fluid is transported, and random fibre misalignment often leads to irregularities in both the flow speed and mixing behaviour.

It is possible to further enhance the mixing improvement due to the presence of the fibres by increasing or spatially-varying the flow/fibre misalignment by introducing tortuousity in the channel. To illustrate this, we patterned both zigzag and curved channels, as shown in Figs. 3.1(a) and Figs. 3.1(b), in which we observe considerable improvement in the mixing performance (Fig. 3.8(b)). It should be noted that the mixing enhancement cannot not attributed to the vortical structures induced by Dean flows that was previously shown in curved microchannels [187]. Given a channel hydraulic diameter $D_{\mathrm{H}} \approx 0.002$ mm, radius of curvature of the flow path $R \approx 3$ mm, and Reynolds number $\mathrm{Re} \equiv \rho U W/\mu \sim O(1)$ (ρ and μ being the fluid density and viscosity), the Dean number $\kappa \equiv \left(\sqrt{D_{\mathrm{H}}/2R}\right) \mathrm{Re} \sim O(0.01)$ is small. This suggests that the Dean flow due to the channel curvature is weak and any mixing enhancement arising from flow vorticity can be neglected. In contrast, the mixing enhancement due to the channel tortuousity can be attributed to the amplification of the flow/fibre misalignment effect as the flow is forced to traverse the fibres multiple times as it is guided through the tortuous channel geometry. Handedness effects in the mixing are apparent though, arising from the asymmetry in the outlet channel from the Y-junction. For example, as seen in Fig. 3.1 as well as Fig. 3.8(b), there is poorer mixing on the right-hand bends at the odd-numbered locations (3, 5, 7 and 9) compared to the left-hand bends at the even-numbered locations (2, 4, 6, 8 and 10) for the zigzag and curved channels. The handedness is however more prominent in the zigzag channels due to the sharp bends.

3.4 CONCLUSIONS

Paper-based microfluidic systems offer a simple, low-cost and disposable alternative for point-of-care diagnostics. Whilst the single-strip lateral flow immunochromatographic assay is now used for a wide range of diagnostic testing, advances in paper microfluidic networks offer significant opportunity in applications beyond simple qualitative tests to multiplex, sensitive and quantitative assays not only for third-world diagnostics but also for field-use environmental monitoring, smart food labelling and drug development, amongst other applications. The obvious advantages of these paper-based systems over conventional microfluidic substrates also provide justification to broaden their functionality to replicate that of the silicon and PDMS counterparts. This, however, requires typical microfluidic operations such as flow actuation and bioparticle manipulation to be carried out on paper substrates. Here, we demonstrate the use of SAWs, powerful fluid actuation and manipulation tools already part of the microfluidic arsenal, to drive the flow and induce uniform mixing in paper-based microfluidic channels. Though at the expense of introducing external forcing, we show that nonuniformities and poor reproducibility in passive mixing in paper networks that arise as a consequence of limitations unique to capillary-driven flow in paper can be circumvented to provide faster, more uniform, repeatable and predictable mixing on paper. The expense in terms of cost, size and integrability is however minimal with SAW actuation since it has been previously shown that the highly efficient fluid-mechanical coupling allows a wide range of microfluidic operations to be carried out in an inexpensive chip-sized device at very low powers driven by a miniature battery-powered circuit that can easily be integrated. In the process of examining various parameters that control the flow speed and mixing efficiency, such as input power, channel shape/tortousity and fibre/flow alignment, we also introduce a new hue-based colourimetric technique that allows for mixing quantification without limitations on the colour and contrast of the samples.

4

BULK ACOUSTICS: SIMPLER AND CHEAPER ACTUATION SETUP AND OTHER PECUILAR FLOWS

In this chapter we show that it is possible to circumvent the necessity of costly and complex cleanroom fabrication procedures in the production of MHz-order acoustically-driven microfluidic platforms through the use of electrode strips simply cut from kitchen aluminium foil or depositing simple, large scale gold electrodes. By completely removing the high device production costs and addressing issues associated with the reliability of complicated electrode technology, this exceptionally simple and low-cost acoustofluidic platform, on which we demonstrate rapid and efficient fluid transport and manipulation, microcentrifugation, and, remarkably, even nebulisation, in both sessile drops as well as paper-based substrates, is therefore a significant step closer towards commercially-viable consumer diagnostic devices, especially for use in the developing world. At high frequency vibrations, a novel poloidal flow within a drop was observed and is explored in the second part of this chapter.

4.1 INTRODUCTION

The majority of the early work on acoustically-driven microfluidic actuation focused on the use of bulk ultrasonic transducers. These typically consisted of thin plates or membranes comprising a piezoelectric ceramic along which flexural waves (i.e., asymmetric Lamb waves) are generated; the plate/membrane thickness being a fraction of the wavelength of the flexural wave. For example, in [139, 137] silicon nitride was coated onto a ground plate, followed by the deposition of a thin zinc oxide layer and subsequently the aluminium interdigital electrodes. The bulk vibrations that ensue then drive acoustic streaming, which due to the large attenuation length for the 1 MHz order employed, extended over a long range, typically a few centimeters from the membrane [118]; as such, the device can also be used for mixing applications [218]. Nevertheless, these flexural wave pumps are not as efficient compared to the SAW fluid actuation which we discuss in the next section, with larger powers required and one to two orders of magnitude lower in velocity (typically up to 100 μm/s), even when focusing electrodes are employed [137].

In a similar manner, it is also possible to exploit substrate vibration to depin contact lines and to drive droplet motion in open microfluidic platforms. In the former, a contact line hysteresis condition for a drop subject to vibration was derived in which the depinning was dependent on the vibrational acceleration [145]; in other work, the drop can be shown to spread under 1 MHz order piston-like thickness mode vibration of the underlying substrate, which induces a boundary layer streaming flow that endows an additional surface force at the contact line [126]. In the latter, a flexurally vibrating beam was employed in [9] on which different modes were excited in order to translate the drop between nodal locations.

Ultrasound-induced bubble oscillation can also be exploited to induce oscillatory flows, particularly useful for micromixing, or to facilitate nucleic acid transfection across cell membranes (i.e., sonoporation), even to the point of cell lysis [148]. In these cases, the bubbles are sonicated at resonance (typically kHz order) to induce a strong flow known as cavitational microstreaming that arises as the sound energy is dissipated due to the fluid viscosity in a boundary layer surrounding the bubble [147]. Pumping flows of around several mm/s can be achieved, for example, with multiple bubbles housed in a cavity array and can be used to drive micromixing [197] or even cell sorting [152] . More examples of the use of bubble oscillation in microfluidics can be found in this review [74]. Whilst relatively fast flows with reasonable throughput on the order of 100 μl/min and efficient mixing can be generated using bubble-based microfluidic actuators, difficulties associated with generating, trapping and maintaining the stability of bubbles is a common problem that has yet to be adequately resolved in addition to limitations arising from molecular/cell lysis due to cavitational damage that can be undesirable in bioapplications other than gene transfection.

Much more progress has been observed on the acoustophoretic front, on the other hand, in which ultrasonic standing waves are employed to focus particles onto nodal lines for cell sorting [70], colloidal filtering [75] or particle switching [125] applications. Particles can also be separated based on size by exploiting the discrepancy in the size scaling between Eqs. 1.1 and 1.2 and hence the dependence of the particle migration time on the particle dimension (larger particles aggregate more quickly compared to smaller ones); such fractionation is more specifically known as free-flow acoustophoresis when conducted in a continuous flow system with the particles being driven orthogonal to the flow. Other design variations have also been investigated, for example flow splitting [90] and frequency switching [116]. Two vastly different particle species can also be separated given that the acoustic radiation force switches directions between positive and negative contrast factors in Eq. 1.3, a property that was exploited for separating lipids from red blood cells [154] The reader is referred to [101] for a more detailed discussion on acoustophoresis and its applications.

4.2 SIMPLE AND LOW COST ACOUSTOMICROFLUIDICS USING ALUMINIUM FOIL

The prohibitive cost (primarily associated with fabrication) and complexity of microfluidic technology are common reasons given to explain why only a very small fraction of microfluidic devices have so far successfully navigated the arduous commercial translation path to reach the vast point-of-care diagnostics market. These factors are only compounded further if the technology is aimed for use in the developing world where extremely low costs and simplicity of operation are of utmost importance. Of late, there has therefore been considerable effort aimed at making microfluidic devices simpler and cheaper in order that the technology can be made more accessible both to the developing world or to the wider consumer market. Some of the best examples of simple and low cost microfluidic platforms are paper-based [131] or even thread-based [105] systems, as well as other creative solutions that have been proposed to enable rapid and high volume production of low cost or disposable devices such as the 'Print-n-Shrink' [182] and Lab-on-a-Foil [54] technologies, amongst others [128].

We are inspired, in particular, by the imaginative use of pencil lead rubbed onto paper as a simple and low cost method for creating electrodes to drive electrokinetic flow on paper-based microfluidic substrates.[124] In this work, we demonstrate, simply by using a small strip of kitchen aluminium foil as electrodes (Fig. 4.1(a)), the possibility for circumventing the barrier associated with the signifiant costs incurred during complex cleanroom fabrication of the interdigital transducer (IDT) electrodes required to drive the high frequency acoustically-driven microfluidic devices that have recently received widespread interest given their powerful potential for a wide range of microfluidic actuation [119, 58, 113, 46, 221] for applications across drug delivery,[157] biosensing,[161] cell sorting,[57] and disease diagnostics.[25] In a manner analogous to the low-cost electrokinetically-driven paper-based microfluidic platform [124], we show in the present work that we can replicate the ability to drive microfluidic transport in paper-based substrates using surface acoustic waves (SAWs)[163]—albeit with greater simplicity and significantly lower costs—whose considerable advantages of enabling uniform flow

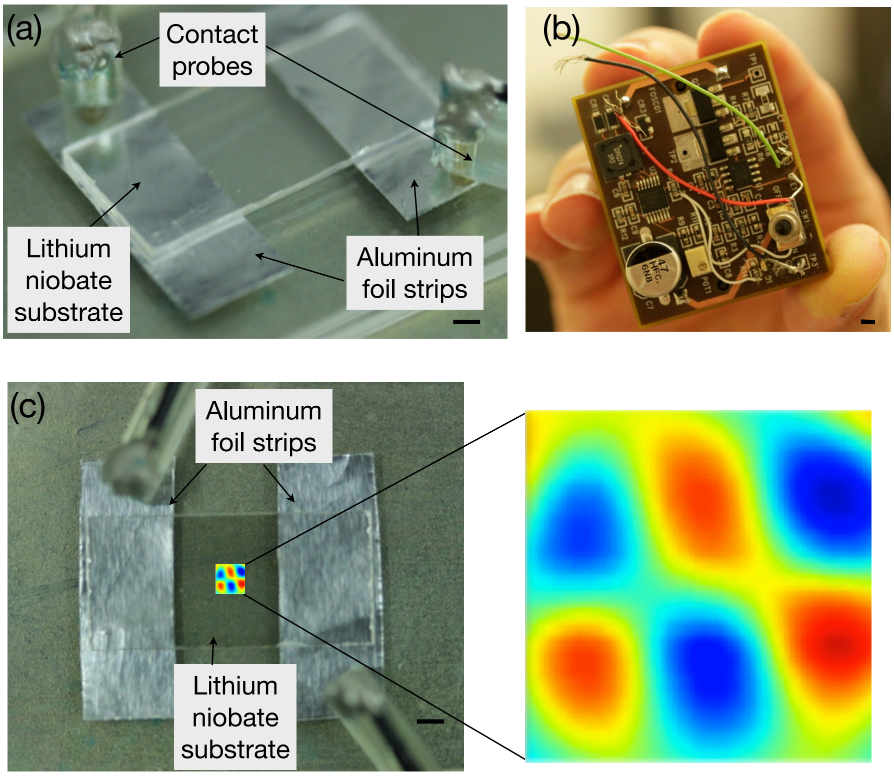

Figure 4.1: (a) Image showing the simple setup of the device which comprised the lithium niobate piezoelectric substrate placed atop two strips of aluminum foil. The aluminium foil is in contact with the lithium niobite substrate and is connected to an AC source via the contact probes. (b) Portable palmtop driver circuit used for the SAW experiments that runs on a single camera battery [222, 157]. (c) Top-down image of the device with a LDV scan of the surface displacement overlaid over the device; the inset shows a magnification of the scan showing the existence of a two-dimensional Lamb wave pattern. Scale bars $\sim$ 1 mm.

and highly reproducible mixing over passive capillary-driven paper systems was somewhat limited by the cost of fabricating the complex IDT structures on the SAW devices.

On top of the usual challenges associated with driving high frequency (MHz order) acoustofluidic actuation, the mechanism by which fluid is acoustically transported through paper predicates on the ability to nebulise the fluid from the paper[163]—which is not trivial given that nebulisation has the highest power requirement over all other microfluidic manipulations given the need to deform and eventually break up the fluid interface by overcoming the large capillary stresses, particularly that in aqueous systems [222]. As such, we require our simple design based on the aluminium foil electrodes to be sufficiently efficient in driving fluid nebulisation in order to retain the use of the low cost palmtop driver circuit previously reported [157] (Fig. 4.1(b)) in place of large, cumbersome and expensive amplifiers and signal generators—which was one of the unique advantages of the SAW technology[163] over other microfluidic actuation strategies [65].

In certain respects, these design specifications constituted somewhat conflicting requirements. On the one hand, we have shown that the SAW is by far the most efficient acoustic mechanism for microfluidic actuation, thus allowing it to be driven at sufficiently low powers to allow the use of a portable driver circuit—an advantage that cannot be replicated using all other microfluidic actuation, let alone ultrasonic, technologies. On the other, the generation of the SAW requires the patterning of IDTs on piezoelectric substrates that involve complex and costly cleanroom photolithography and wet etching procedures. Removal of this step and hence the IDTs would therefore require the generation of bulk acoustic waves that have efficiencies for microfluidic actuation that are close to that of the SAW such that nebulisation can be carried out even with the portable driver circuit running on a single camera battery (Fig. 4.1(b))—to our knowledge, this has not been possible to date. The only exception that comes remotely close to partially meeting these requirements is the use of poled lead zirconate titanate (PZT) to generate Lamb waves on a glass substrate on which drop translation and mixing was demonstrated.[206] In that work, the PZT element containing a single phase transducer, which is considerably simpler to fabricate than IDTs, was glued to the glass substrate. Nevertheless, the reduction in cost and complexity in this work came at the expense of device efficiency, and the possibility for driving 'high power' applications such as the nebulisation necessary for acoustically-driven transport through paper substrates using this setup has not been demonstrated even with conventional benchtop power supplies, let alone a portable driver circuit which has a power output limitation of approximately 1 W. Further, unlike the monolithic substrates employed in the SAW and in the present work, the PZT-based devices are not easily miniaturised given difficulties in reducing the size of the element to chip-scale dimensions without further sacrificing efficiency considerably beyond which it is no longer possible to drive microfluidic actuation.

Here, we nevertheless show that it is possible to employ an even simpler and cheaper design, without requiring any cleanroom fabrication whatsoever, but yet achieve better efficiencies through the use of lithium niobate (LN) in place of PZT and retaining the possibility for integration together with the palmtop battery-powered driver circuit into a miniaturised device commensurate with that required for point-of-care diagnostics applications. The process by which the electrodes are made is exceptionally simple. Standard aluminium foil such as that used for food preparation in home kitchens was cut into rectangular

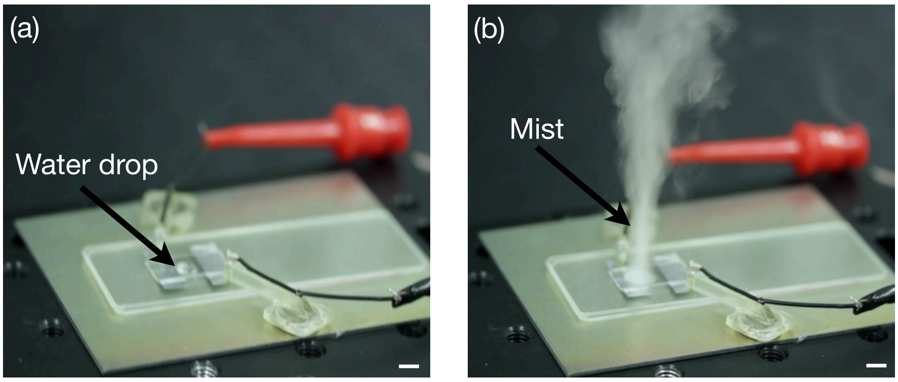

Figure 4.2: (a) A 5 $\mu\ell$ sessile water drop pipetted onto the LN substrate is (b) completely nebulised within 2 s to form a mist of monodispersed aerosol droplets 3.5 μm in diameter when Lamb waves are excited on the substrate simply by applying an AC electrical signal to the aluminium foil strip placed underneath the substrate at 3.5 MHz. The input voltage and power to the device is 20 V and 0.5 W. The device had an impedance of 48 ohms. Scale bars $\sim$ 5 mm.

strips using a pair of scissors and subsequently placed in contact with the LN substrate (Fig. 4.1(a)). An alternating current was then applied at the resonant frequency to the foil that then gave rise to Lamb waves on the LN substrate, as shown by the laser Doppler vibrometer (LDV, UHF-120, Polytec GmBH, Waldbronn, Germany) scan in the inset of Fig. 4.1(c). The resonant frequencies that gave rise to the Lamb waves are proportional to the substrate thickness, and a fundamental mode appeared at 3.5 MHz for this case where the substrate thickness was 500 μm, as verified through the LDV scan. When the substrate was lapped to 250 μm thickness, the fundamental resonant frequency was observed to double to 7 MHz. Other resonances are also observed at multiples of the fundamental frequency, although we mainly restrict ourselves to the fundamental mode (unless otherwise indicated) as this provided the most efficient fluid actuation.

Whilst the generation of Lamb waves on LN substrates has previously been reported,[88] we show here for the first time that this can be done without the need for IDTs and hence any cleanroom fabrication process. Unlike the SAW, which is localised within a thickness of several wavelengths (typically several hundred micron) on the *surface* of the substrate, the Lamb waves generated transmit through the *entire thickness* of the material. Although Lamb waves have been previously thought to be considerably less efficient than the SAW in driving fluid actuation, we show, quite remarkably, that the powers required despite the use of the aluminium foil are still low for us to retain the use of the portable driver circuit even to drive nebulisation, which was a key design requirement, by Lamb wave excitation. Moreover, the use of Lamb waves can also be advantageous in that the aluminium foil can simply be contacted from the rear face of the substrate and

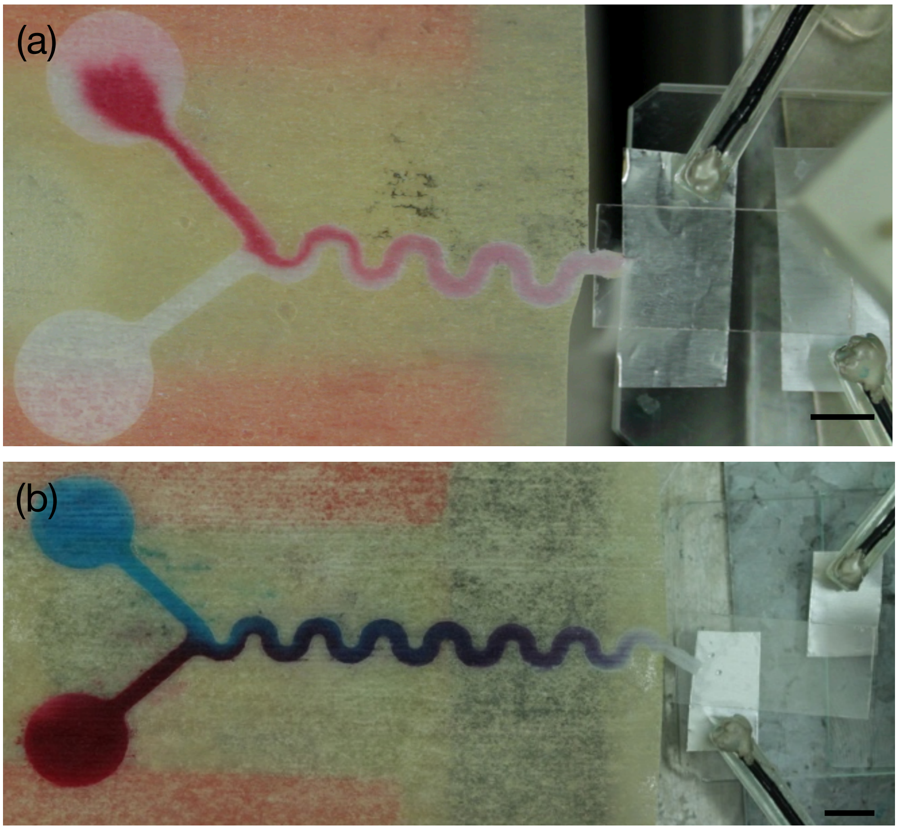

Figure 4.3: (a) Fluid nebulisation at the outlet edge of a Y-channel patterned onto paper in contact with the LN substrate, on which Lamb waves are excited, is observed to drive rapid flow through the paper without backflow into the other arm of the inlet channel. (b) Two differently dyed fluids placed in the inlet reservoirs on each arm of the Y-channel are observed to be rapidly and uniformly mixed as they are transported through the serpentine sections of the channel due to nebulisation at the outlet. The applied frequency and power to the device are 3.5 MHz and 0.95 W, respectively. Scale bar $\sim$ 5 mm.

hence is never in contact with the fluid, which is placed on the front face. This is in sharp contrast to the SAW devices wherein both IDT electrodes and the fluid are co-located on the same face, rendering SAW devices prone to short-circuiting when conductive substances such as physiological samples are used.

Figure 4.2 verifies the ability of the simple design to drive efficient nebulisation of a drop at powers from as low as approximately 0.33 W—two orders of magnitude smaller than conventional ultrasonic nebulisers and slightly lower than with the SAW, which is the reason why we are able to retain the use of the portable battery-operated driver circuit (Fig. 4.1(b)). When the device is placed in contact with the outlet of the virtual fluidic channel patterned on a paper-based substrate using a similar method to the FLASH (Fast Lithographic Activation of Sheets) protocol[131] reported elsewhere,[163] we show that we are able to replicate our results for driving rapid and uni-

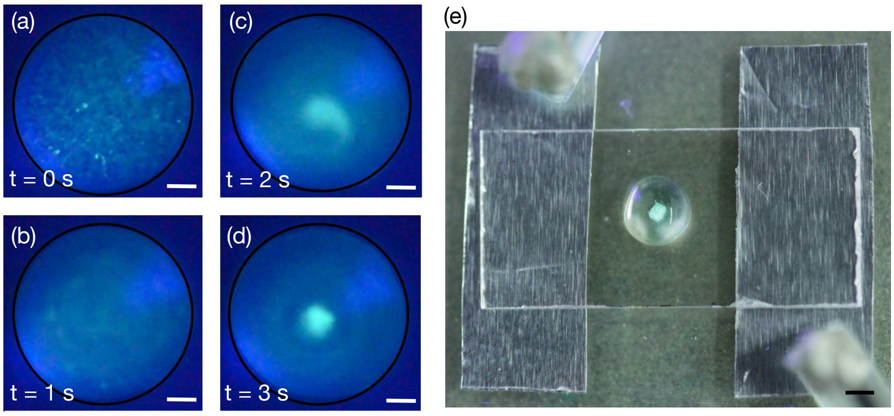

Figure 4.4: (a) Time sequence snap shots showing an initial 3 $\mu\ell$ sessile drop containing a suspension of 4.5 μm fluorescent microparticles at $t = 0$ being rapidly concentrated to its centre within 2 s due to fast azimuthal microcentrifugation flow that arises under Lamb wave excitation of the underlying substrate at a frequency of 17.5 MHz with an input power of 0.09 W. Circles that defined the edge of the drop were drawn to aid visualisation of the drop's position and the scale bar represents a length of $\sim$ 300 μm. (b) The particles are observed to remain aggregated even after the relaxation of the vibration; scale bar $\sim$ 1 mm.

form fluid transport through the paper without the disadvantages of backflow and variability associated with passive capillary-driven flow (Fig. 4.3(a)).[163] When two different fluids are placed separately in the inlet channels, fast and uniform mixing through the paper channel is achieved with the simple low-cost device (Fig. 4.3(b)), again overcoming limitations of poor reproduceability and mixing nonuniformity associated with mixing in pure capillary-driven paper devices.[163]

In addition to fluid transport through paper-based substrates, we also briefly show that the simple low-cost device is able to replicate the range of microfluidic functionality of the SAW[119, 58, 113, 46, 221] with comparable efficiencies. To illustrate, we present two demonstrative results here. By breaking the azimuthal symmetry of the Lamb wave, which can be achieved by either using an asymmetric chip geometry (for example, a triangular device instead of one that is rectangular), using asymmetric electrodes or titling one of the aluminium foil electrodes at a slight angle, colloidal particles suspended in the drop can be rapidly concentrated in a manner akin to that shown using SAW microcentrifugation.[179] Similarly, rapid mixing within a sessile drop due to chaotic acoustic streaming and the fluctuation of the drop's interface can also be induced, as shown in Fig. 4.5.

The chip had many resonant frequencies starting from 3.5 MHz, being the fundamental resonant frequency and then another strong resonance every 7 MHz. The resonant frequencies are proportional to the substrate thickness (500 μm) here and when the substrate

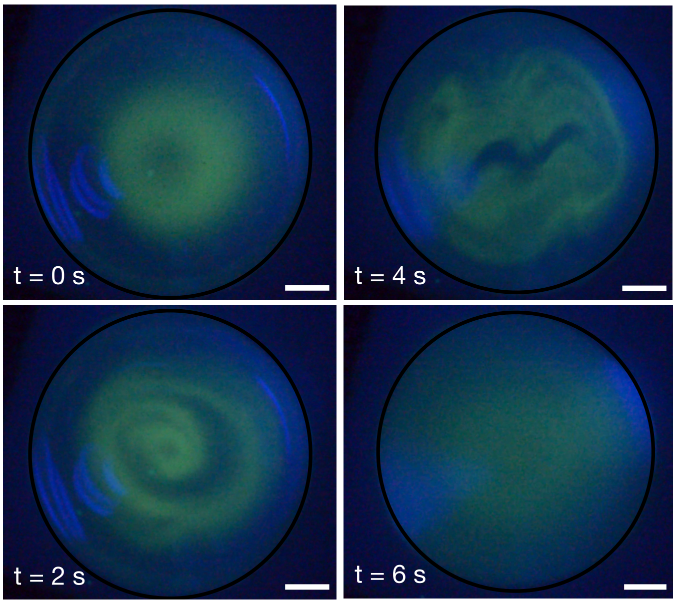

Figure 4.5: Time lapse images for the rapid mixing within a 10 $\mu\ell$ water drop to which a 1 $\mu\ell$ drop of fluorescent dye is added, the Lamb wave excitation at 17.5 MHz and an input power of 0.11 W. Circles are added at the drop's edge to guide the eye and the scale bars are $\sim$ 300 μm.

was lapped to be only 250 μm, the fundamental resonant frequency doubled, i.e. 7 MHz instead of 3.5 MHz.

A common way to compare the performance piezoelectric performance of materials and their associated waves is the use of Figure of Merit (FOM), which is the product of the quality factor (Q) and the electromechanical coupling (K), the former indicates the resonance band frequency width while the former indicates the ratio between the output mechanical energy to the input electrical energy. Contrary to common belief that Lithium niobate being unpractical for bulk and thickness vibrations, especially for microfluidic actuations, and thus SAW has been employed for over a decade now [58], we show here a very high Figure of merit of more than an order of magnitudes than typical SAW. As shown in figure 2 a, the resonance band for this setup is so small, reflecting a very high quality factor (Q) $\sim$ 16,000 in comparison to SAW in figure 2 b, with a quality factor (Q) $\sim$ 70. The electromechanical coupling coefficient, although larger for SAW (K = 3.5 %), in comparison to the Lamb waves generated here using the Aluminum foil setup (K = 0.45 %), the overall product, figure of merit is a lot larger using this simple set up.

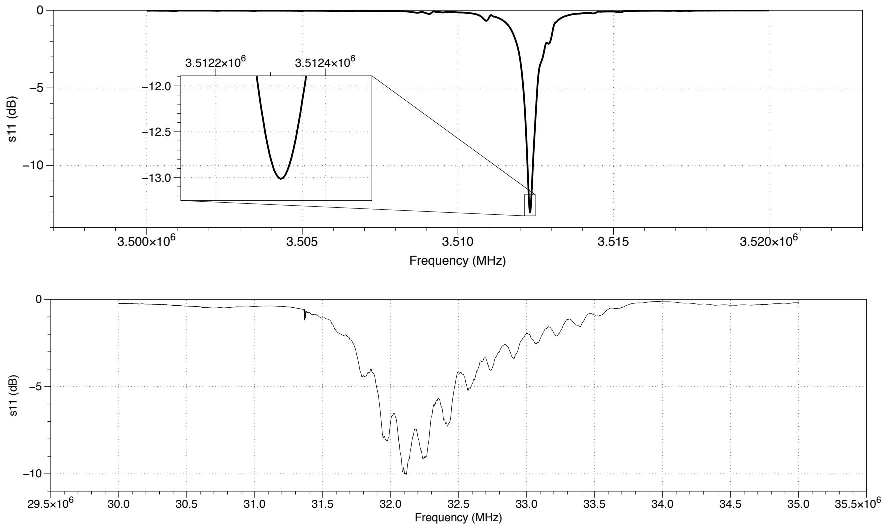

Figure 4.6: Top figure showing s11 repsonse indicating a very narrow response band which leads to a very high quality factor of $\sim 20,000$ compared to the bottom figure, for a typical SAW generated with IDTs, with a low quality factor of ~ 70.

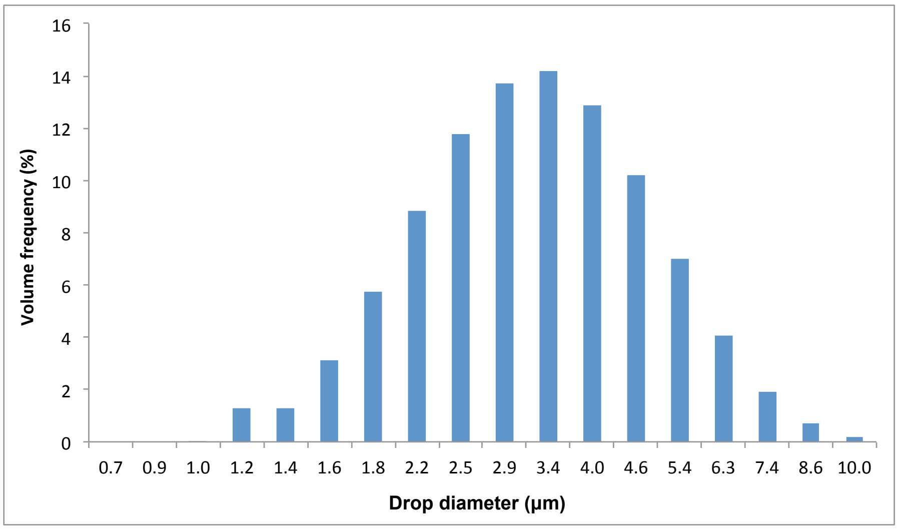

Figure 4.7: Neubilisation results measured using Spraytec, where reasonably monodispersed 3.5 μm droplets were detected.

4.3 NOVEL POLOIDAL FLOW AT HIGH FREQUENCIES ∼ 100 MHZ

Standing Lamb waves in single crystal lithium niobate, generated with a pair of L-shaped electrodes at 157 to 225 MHz, are found to form poloidal flows in a $\mu\ell$ sessile water drop: flows that possess radial symmetry about the center of the drop, propagating from the contact line along the free surface, and downwelling at the center, thus driving fluid recirculation outwards along the substrate to the drop's edge. Unlike Rayleigh surface acoustic waves, the Lamb waves propagate throughout the substrate, forming a regular standing wave pattern in three dimensions. Dependent upon the attenuation of the sound formed and transmitted in the sessile drop, the poloidal flow was found to exist over a narrow range of Lamb wave resonances from 157 to 225 MHz, but absent at lower frequencies where the attenuation was insufficient to prevent multiple sound reflections in the fluid and consequent acoustic streaming along these conflicting directions, and higher frequencies where the attenuation was so high that the core of the vortex was placed near the drop contact line and too far away from the bulk of the fluid to drive it into motion. Driven by shear-induced migration, particles suspended in the drop were found to form azimuthal rings with diameters inversely proportional to the applied frequency.

The manipulation of fluids by high frequency acoustic waves over the 1 MHz to 1 GHz range [58, 114] has recently produced many interesting phenomena that spans fluid jetting [192], fast wetting and unique fingering instabilities [162], chaotic advection [60] and self-similar surface droplet patterning [190]. Suspended particles in the fluid give rise to many other additional phenomena, from microcentrifugation and dispersion [179] and strong nonlinear aggregation [109] to unprecedentedly precise cell and particle manipulation [45].

In this second part of the chapter, we report the emergence of a unique poloidal flow—recirculatory flows about a circular locus—in a sessile drop when it is driven by high frequency acoustic wave coupling and its consequence on the unique aggregation dynamics of particles suspended in the drop into a toroidal ring; the characteristic length scale of the vortical recirculation in the poloidal plane being defined by the confinement of the fluid within the drop, as it occurs in toroidal tokamaks intended for plasma containment in nuclear fusion [83], in the confinement of the mantle between the solid core and flexible crust of the earth [55], or in spherical drops immiscibly suspended in another fluid subjected to rotation about an axis extending through its center [29]. In each case, the force or acceleration applied to the fluid has an axis of symmetry that is perpendicular to the plane of and in the center of the recirculation trajectory. Whilst acoustic waves have been known to generate *azimuthal* recirculation in fluids [179, 109], they have never been reported to form *poloidal* recirculation as found here.

A key reason for the unusual flow behavior is the form of acoustic wave propagation in the substrate. Traditionally, Rayleigh surface acoustic waves have been used in high-frequency acoustic fluid manipulation [58], though on rare occasions other forms of vibration have been attempted, including thickness-mode [217], flexural [137], and Lamb waves with either piezoelectric thin films [139] or mode conversion to a non-piezoelectric substrate [110]; modal conversion can provide effective results [80], though it often requires careful design to align the resonance frequencies of the different modes. Generally, the frequencies used for these other forms of vibration have been less than 10 MHz and the fluid flow induced by these other vibration modes has been weak (μm/s order), the probable reason for the few publications describing devices that use them. As we will show, however, under higher-order Lamb waves at 100 MHz and beyond, the induced flow is rapid due to a combination of strong sound attenuation in the fluid and relatively large acceleration due to the high frequency [42]—the essential ingredients responsible for the phenomena reported here.

Electrodes are patterned on a single-crystal piezoelectric substrate—lithium niobate (LN, 127.68° Y-rotated, X-propagating; Roditi Ltd., London UK) to be specific—using a liftoff technique with polyimide tape (Kapton; DuPont, Wilmington, DE) and the sputtering of 150 nm gold. The choice of L-shaped electrodes (Figs. 4.8(a) and 4.9(a)) is deliberate, such that two-dimensional standing Lamb waves are produced on the substrate with resonance frequencies defined by the 500 μm substrate thickness: the fundamental Lamb wave mode appears at 3.5 MHz, possessing a wavelength of 1 mm, and harmonics appear—consistently—at 7 MHz increments to beyond 250 MHz. The resonances, nature of the wave and the wavelength λ_{Lamb} at each resonance, and the absence of other, perhaps parasitic, waves were verified by measuring the vibration velocity U distribution perpendicular to the LN surface via a scanning laser Doppler vibrometer (LDV, UHF–120, Polytec GmbH, Waldbronn, Germany) and the S-parameters using a vector network analyzer (ZVA, Rhode & Schwarz Pty. Ltd., North Ryde, NSW, Australia). Perhaps surprisingly, the resonance frequencies only very weakly depended on the electrode geometry and the mounting of the LN chip. By leaving the edges of the chip free, the Lamb wave reflections were strong and a standing wave formed throughout [67], as observed in Fig. 4.9(b).

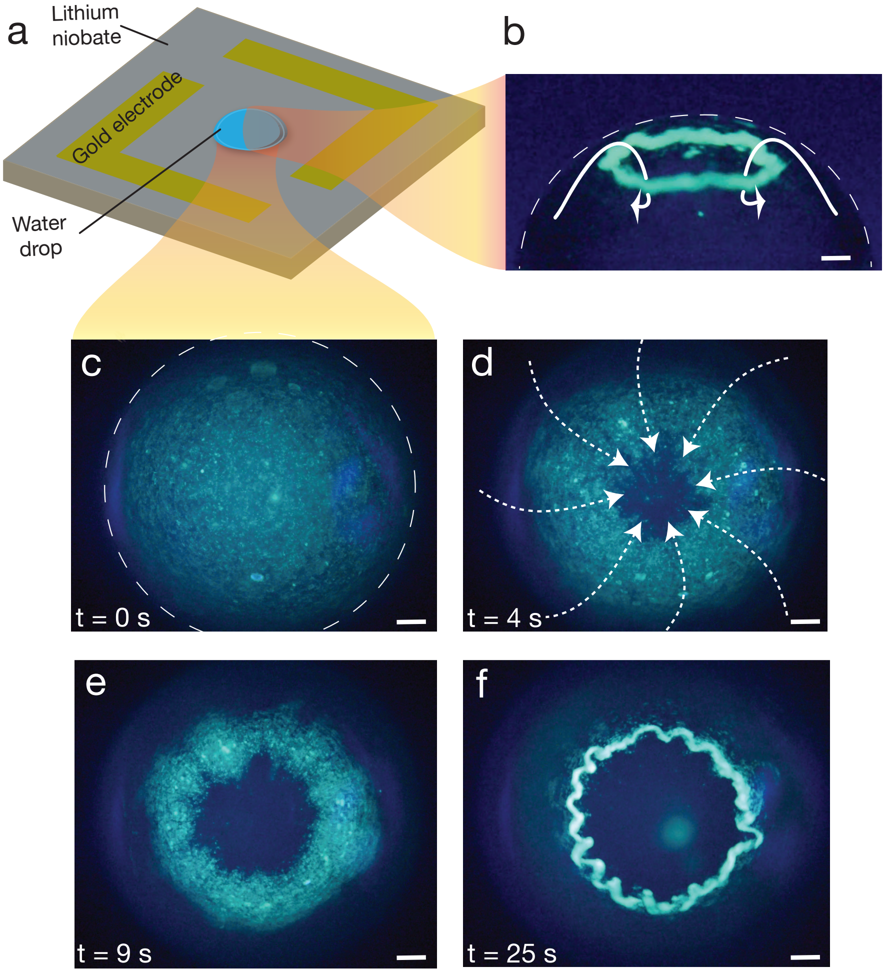

Figure 4.8: (a) A pair of L-shaped Au electrodes that provide effective piezoelectric coupling for the generation of Lamb waves across a broad range of frequencies in the 500 μm thick LN substrate, from 3.5 MHz to 225 MHz and beyond were patterned on the lithium niobate substrate on which a 3 $\mu\ell$ sessile drop was placed. (b) Side view of the sessile drop in which particles were suspended subject to two-dimensional substrate vibration at 225.3 MHz and 0.8 W power after the formation of a particle torus due to the poloidal flow helps illustrate the flow geometry, as does (c–f) the time sequence of top-view images for the same drop, showing the steps by which the torus forms due to shear-induced migration and is subject to a subsequent instability; dotted lines were added to aid visualization of the drop edges and arrows indicate the flow direction. Scale bars are $\sim$ 300 μm.

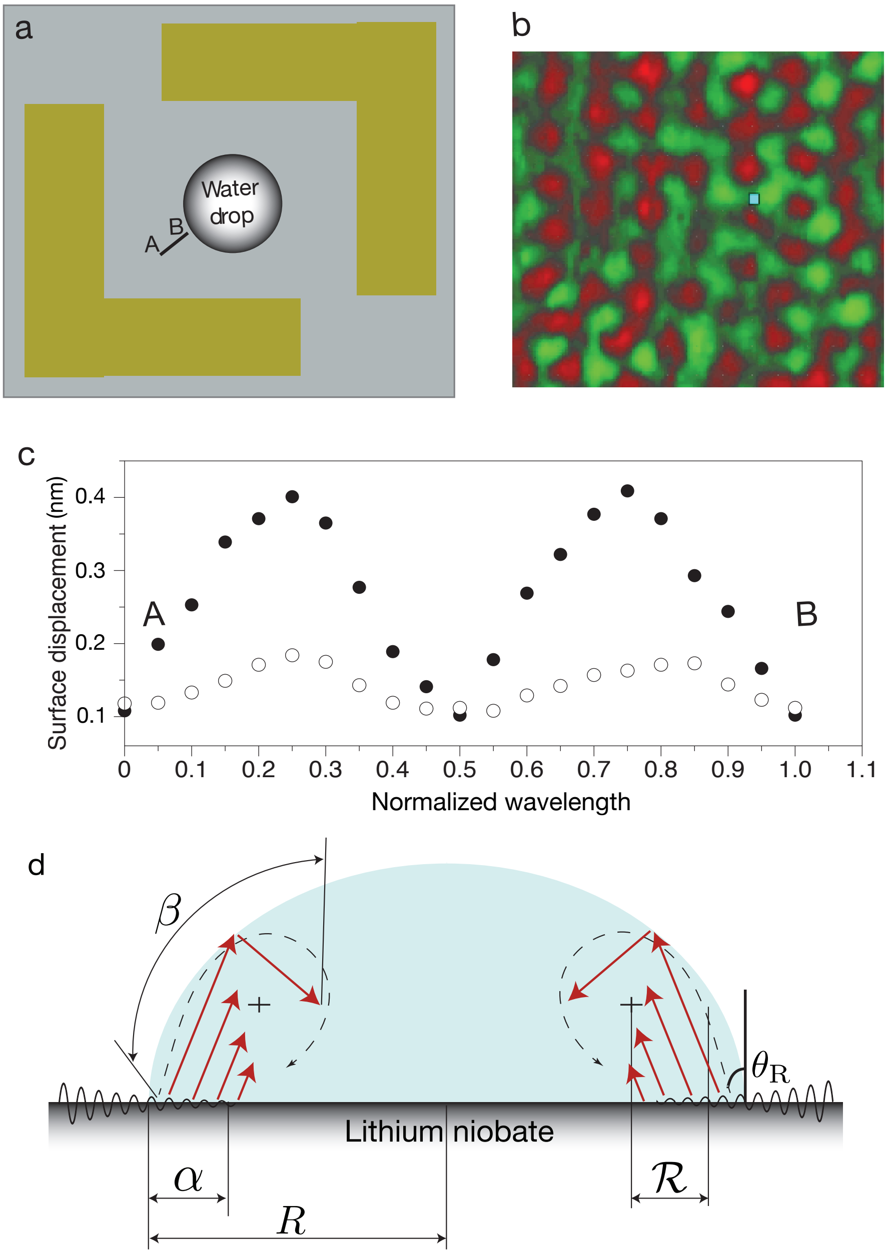

Figure 4.9: (a) Top-view sketch of the device comprising the L-shaped electrode configuration and the drop, and an indication where a line scan from A to B is carried out using the LDV before and after placing the drop. The vibration amplitude distribution across the area confined by the electrodes at 157 MHz shows the formation of a standing wave in (b), while in (c) the LDV results for the line scan A–B prior to drop placement indicates a standing wave ratio (SWR) of nearly 4 and a wavelength along both axes of $\lambda_{\text{Lamb, 157 MHz}} = 23\ \mu\text{m}$ (filled circles), and a SWR of approximately 2 in the presence of a drop, which draws acoustic energy from the substrate to leave a travelling wave on the substrate (open circles). (d) Schematic illustration of the drop across the poloidal plane indicating the characteristic length scales pertinent to the mechanism underlying the formation of the poloidal flow: the Lamb wave attenuation in the solid beneath the drop α, the sound wave attenuation within the bulk of the fluid β, the drop dimension R and the poloidal recirculation length scale $\mathcal{R}$.

For the flow experiments, water drops spanning a range of diameters (0.5 to 10 μl) were placed on the bare LN substrate after cleaning, and a signal generator (SML01, Rhode & Schwarz Pty. Ltd., North Ryde, NSW, Australia) and amplifier (10W1000C, Amplifier Research, Souderton, PA, USA) were used to provide a continuous sinusoidal electrical input at the defined frequency f. Polystyrene spherical particles with diameter $a \approx 4.5$ μm in diameter (Polysciences, Warrington, PA USA) were employed to visually track the flow in the drop; the particles are below the transition size at which direct acoustic forces influence their behavior, and hence they can be assumed to follow the trajectory of the flow via the influence of the Stokes drag. As shown in the side-view image in Fig. 4.8(b) or the time sequence top-view images in Fig. 4.8(c–f), the effective coupling of the Lamb waves into the drop at high frequency (225 MHz) is seen to drive a unique poloidal flow within the drop, which, in turn, drives the formation of a particle toroidal ring, which we shall show below, can be attributed to a shear-induced particle diffusion process.

To elucidate the underlying mechanism responsible for the generation of the poloidal recirculation in the drop, it is necessary to understand the nature by which the acoustic energy is coupled into the drop to drive the flow. In particular, we note the presence of the drop on the LN substrate on which a checkerboard standing Lamb wave pattern pre-exists due to the high frequency excitation (Fig. 4.9(b)) acts as an energy sink, weakening the standing wave toward and beneath the drop. This is evident from the decrease in the standing wave ratio (SWR) by approximately one half, as observed in Fig. 4.9(c), along the radial direction toward the center of the drop (for example, along A → B in Figs. 4.9(a) and (c)), suggesting that the energy loss from the substrate increases from 16% for Lamb wave excitation on the bare LN substrate to 44% when the drop is present. Given that the LN is otherwise nearly lossless, it is reasonable to assume that this difference (28%) is subsumed by the drop, generating a propagating sound wave in the bulk of the fluid, as a consequence, at the Rayleigh angle $\theta_{\text{R}} = \sin^{-1} c/c_{\text{Lamb}}$, as illustrated in Figs. 4.8(b) and 4.9(d); c is the speed of sound in the liquid (1482 m/s for water) and c_{Lamb} is the Lamb wave speed. Given that the latter is dependent on frequency [87]—especially in this case of a uniquely two-dimensional Lamb wave—θ_{R} is similarly frequency-dependent. For the high-order harmonics at 25 MHz and upwards, however, $c_{\text{Lamb}} \overset{\sim}{\rightarrow} 4000$ m/s [87], and hence $\theta_{\text{R}} \approx 22°$.

More specifically, the Lamb wave attenuates in the substrate beneath the fluid loading at a rate that is strongly dependent upon the chosen mode. Given the higher-order mode excitation, this can be estimated by an attenuation length (Fig. 4.9(d)) [33]

$$\alpha = \frac{\rho c}{\rho_{\mathrm{Lamb}} c_{\mathrm{Lamb}} \lambda_{Lamb}}, \tag{4.1}$$

in which ρ and ρ_{Lamb} are the liquid (998 kg/m^3) and substrate (4630 kg/m^3) densities, respectively. With $c_{\mathrm{Lamb}} = 4000$ m/s, $\alpha = 2.5$, 0.35 and 0.18 mm for 25, 175.5, and 225.3 MHz, respectively. Notably, the value of α is less than that of the drop radius $R = 1.5$ mm for the higher pair of frequencies: the acoustic wave cannot be sustained to the center of the drop in the substrate, and so any energy leakage into the drop occurs in a region that is confined by a distance of α from the contact line of the drop. On the other hand, the propagating sound wave in the fluid possesses a different attenuation length

$$\beta = \frac{4\pi^2 f^2}{\rho c^3}\left(\frac{4\mu}{3} + \mu'\right), \tag{4.2}$$

which has values of 80, 1.5, and 1 mm for 25, 175.5, and 225.3 MHz, respectively; in the above, μ and μ' are the shear and bulk viscosities, respectively. Importantly, $\beta < R$ at the higher frequencies, indicating that under these conditions and allowing for reflections at the free surface of the drop due to its curvature and the propagation of the sound wave along θ_{R} (Fig. 4.9(d)), the sound wave is likely to be completely attenuated before it reaches the center of the drop.

Both the sound attenuation behavior along the substrate and in the bulk of the fluid then suggests that a substantial portion of the drop core over a length scale given by the lesser of $R - \alpha$ and $R - \beta$ is not exposed to any acoustic radiation that is required to drive the flow, at least at sufficiently high frequencies. In contrast to the previously observed acoustic streaming behavior in drops excited at lower frequencies in which the entire bulk of the fluid in the drop recirculates (Eckart streaming [49, 28]), such confinement of the acoustic energy around the periphery of the drop over a region characterized by $\mathcal{R} \sim \min |R - \alpha, R - \beta|$ (Fig. 4.9(d)) gives rise to the poloidal flow exemplified in Figs. 4.8(b–f) and 4.10 at these high frequencies. We note that the acoustic excitation appears to remain symmetric about the z-axis along the centre of the drop despite the underlying Cartesian form checkerboard Lamb wave pattern on the substrate: there are no first-order circumferential variations in the acoustic radiation within the drop. To further confirm this hypothesis, we observed the absence of poloidal flows when R is decreased below 0.5 mm such that $(\alpha, \beta) < R$ (not shown). Similarly, the poloidal flows in the larger drops ($R \approx 3$ mm) are replaced by the usual Eckart streaming for larger α and β with a lower excitation frequency of 25 MHz (Fig. 4.10, top left image).

Further support for our postulated mechanism is supported by the very good agreement between the experimentally-observed poloidal flow, captured through the behavior of the suspended particles in the drop (the specific mechanism by which the particles assemble into toroidal rings will be discussed below), and that predicted through a numerical simulation that accounts for the acoustic wave coupling and the resultant flow field. More specifically, the numerical simulation involved a finite element analysis (850,000 node brick mesh with node separation of approximately 2 μm using ANSYS CFX 14.5 (ANSYS Inc., Canonsburg, PA)) of a single-phase water drop with a diameter of $2R = 3$ mm and an air-water interface with a shear-free boundary corresponding to the 3 $\mu\ell$ drop in the experiments. The drop was assumed hemispherical with its contact line pinned, justified through the absence of any spreading or shape variations in the experiments. Simulations were run until convergence was obtained with the momentum and mass residuals falling to a value below 10^{-6}. Laminar flow was assumed in the model due to the low Reynolds number and based on past evidence of the acoustic streaming behavior [42]; no capillary waves are expected as a consequence of the laminar flow [22], as verified using the LDV, and hence the free surface was reasonably assumed to be rigid. Ideally, a full model of the fluid and piezoelectric LN substrate would be used, but the high frequency and short wavelength analysis of such a model (forming well over 20 million elements) rendered it impossible to analyze. Instead, the fluid-substrate vibration coupling is captured through a slip boundary condition at $z = 0$ incorporating the drift flow generated by the surface wave [127]:

$$\begin{pmatrix} u_r \\ u_z \end{pmatrix} = \begin{pmatrix} (\epsilon\chi\xi U/2\eta)\,\mathrm{e}^{-2\alpha(R-r)} \\ \alpha\delta z\epsilon\chi\xi U(R-r)\mathrm{e}^{-2\alpha(R-r)} \end{pmatrix}, \tag{4.3}$$

in which r is the radial coordinate, and u_r and u_z are the radial and axial drift velocities, respectively. $\epsilon \equiv U/c$ is the acoustic Mach number; $\chi \approx 1$ is the ratio between the longitudinal and transverse velocity components of the wave, φ is the phase angle between the longitudinal and transverse velocity components of the wave, $\xi \equiv (\cos\phi - \sin\phi)$, and $\delta \equiv \sqrt{4\pi\mu/\rho f}$ is the characteristic thickness of the viscous boundary layer.

The formation of the toroidal particle ring typically exemplified in Figs. 4.9(c–f) can be attributed to the homogenization of the suspended particles that are swept by the poloidal flow trajectory into closed

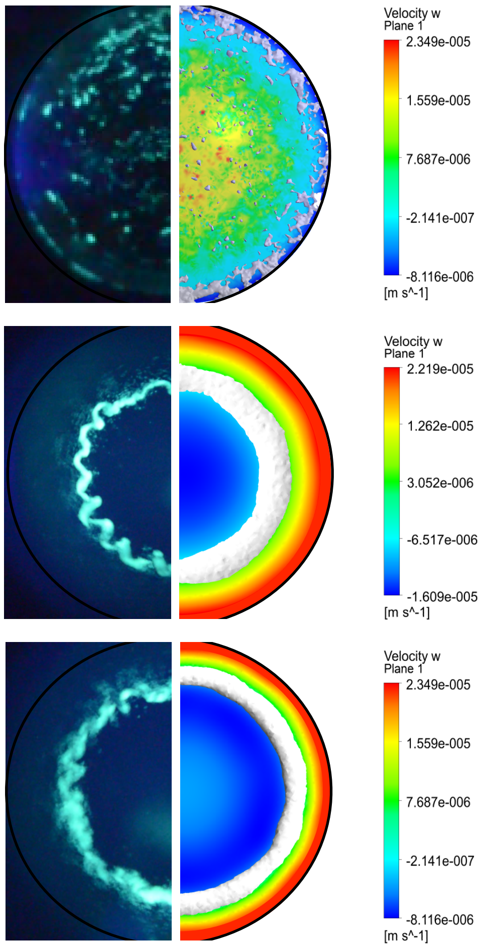

Figure 4.10: A plane cross-sectional view comparison of the particle behavior in the 3 $\mu\ell$ drop between images captured during the experiments (left) and that predicted from the finite element analysis (right). When driven at 25 MHz (top image), in which the Eckart streaming [49] is found to be dominant throughout the drop in both the experiment and analysis; instead of poloidal flow, bulk recirculation reminiscent of most acoustic drop manipulation experiments is seen [28], leading to the dispersion of the particles [179]. When driven at 157 MHz (middle image), the poloidal flow leads to the the collection of fluorescent polystyrene particles into an toroidal ring; the white region on the right represents the region of the fluid with vorticity at or greater than 0.5 s^{-1}, serving as an effective means to track the circular vortex at the core of the poloidal flow. Increasing the excitation frequency to 255.3 MHz (bottom image) produces a *larger* particle ring because of the increased attenuation of the sound wave in the substrate and fluid at this greater frequency.

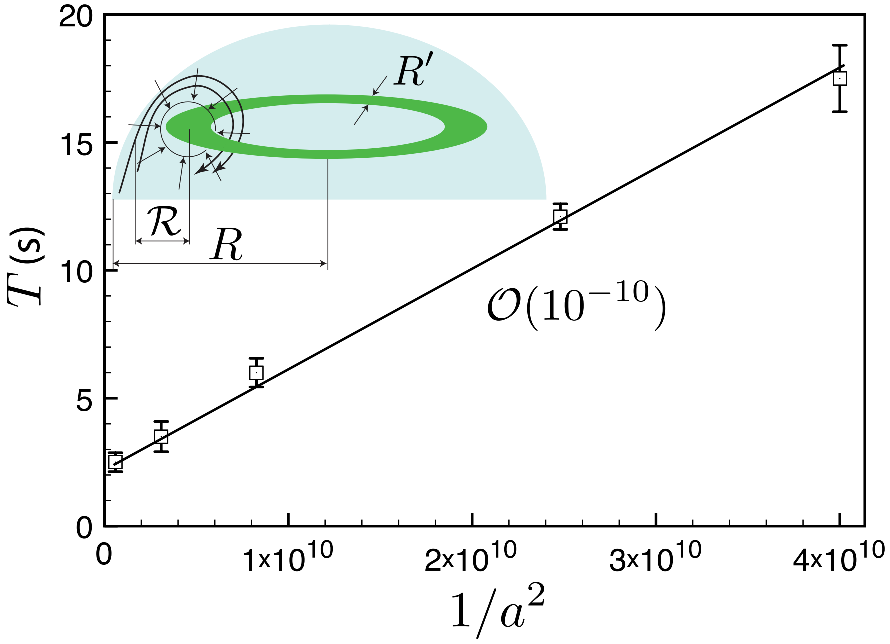

Figure 4.11: (a) Schematic illustration of the poloidal flow driven shear diffusion mechanism responsible for the formation of the toroidal particle ring, and, (b) the corresponding aggregation time T as a function of the particle size a. The initial particle concentration of the drop is 10^5 particles/mℓ and the RF power to the Lamb wave device is held constant at 0.8 W. The arrows in (a) indicate the cross-streamline transport of the particles in the poloidal plane as a consequence of shear diffusion from the high shear outer poloidal flow region to the recirculation interior, which causes them to aggregate into a torus.

streamlines of length scale $\mathcal{R}$. Due to the higher velocities along the outer streamlines, a shear gradient exists that, upon the local volume fraction of the particles along the streamline ϕ exceeding a critical value (usually corresponding to the maximum packing fraction 0.68 for hard spheres), results in cross-streamline particle transport from the high shear regions along the outer streamlines [103] to populate the low shear interior regions of the poloidal locus, as illustrated by the schematic in Fig. 4.11(a). This is verified by the particle diffusion time which scales as $1/a^2$, as shown in Fig. 4.11(b), consistent with that expected from an effective cross-streamline diffusion rate $\dot{\gamma}\phi a^2$; $\dot{\gamma}$ being the shear rate and a the particle size. This is further verified by the good order-of-magnitude agreement between the $\mathcal{O}(10^{-10})$ slope predicted for the particle aggregation time $T \simeq V^2/\dot{\gamma}\phi a^2$ with a characteristic particle aggregate dimension $R' \sim 10^{-4}$ m and $\dot{\gamma} \sim 10$ s^{-1} and that measured experimentally (Fig. 4.11(b)). To our best knowledge, this is the first time that a toroidal particle aggregate arising from a poloidal-oriented shear diffusion gradient has been reported. Further, the particle ring instability observed in Figs. 4.8(f) and 4.10, reminiscient of vortex ring instabilities [209] appears to arise possibly from azimuthal disturbances to the flow driven by small perturbations in the substrate vibration around the contact line of the drop.

4.4 CONCLUSIONS

In Conclusion, we show arguably the simplest MHz acoustics platform using a very attractive single crystal material, such as lithium noibate in this case here, which is previously believed to have weak bulk piezoelectric properties and thus rendering it unpractical for Bulk wave type vibrations, such as Lamb waves. Together with the ability to use a portable palmtop driver circuit powered by a single camera battery, we believe that the removal of the costly, complex and cumbersome fabrication procedures required for the patterning of IDTs in SAW devices simply through the use of strips of aluminium foil is a significant step that addresses issues surrounding the costs and reliability of active microfluidic actuation platforms, especially for use in consumer devices, particularly those aimed for the developing world.

In addition, we show, for the first time, 2D dimensional Lamb waves generated by a very simple setup by depositing two L-shaped large mm-scale gold or aluminium electrodes which, at high frequency ($\sim$ 100 MHz) vibration, lead to an unprecedented poloidal flow inside a drop, where, the attenuation length is smaller than the radius of the drop thus suppressing the multi-interface reflection responsible for chaotic flow at lower frequencies. Then followed by an azimuthal shear induced migration mechanism to generate a vortex ring.

5

CONCLUSIONS AND FUTURE WORK

In this final chapter we provide an overview of the work conducted in the thesis and list the key contributions made. The chapter and thesis will conclude with possible future work that could come out of the findings.

5.1 CONCLUSIONS

In this thesis we have conducted an extensive Experimental, theoretical and numerical study of films actuated by SAWs, with two newly discovered microfluidic phenomena; fingering instabilities and soltion-like wave propagation. In addition, an application for the use of the SAW for paper-based diagnostics was demonstrated by showing that SAW can drive uniform, reliable and fast mixing in paper micro channels. Furthermore, a creative cheaper and simpler design for MHz acoustomicrofluidics was considered where the piezoelectric lithium niobate was used without any costly IDT fabrication and instead simple electrodes of gold or aluminium were deposited or even in some cases kitchen aluminium foil was used instead as an electrode. Finally, the use of the these simple Lamb wave device at high frequencies of 100 MHz and beyond, has unraveled a novel poloidal flow which led to a unique ring formation within μl drop.

The chief contributions of the thesis are as follows:

- The first exhaustive study of SAW interactions with low viscosity thin oil films where a double flow reversal phenomenon was revealed; ultrthin films with a thickness comparable to viscous penetration depth were observed to flow along the SAW drift, thin films were observed to move opposite to the SAW propagation direction, while thick films and drops, revered direction again and moved along the SAWs. The thin films were also seen to develop a unique interfacial fingering instability due to the SAW diffraction pattern and and a curous soliton-like wave trains were shown to emerge and propagate on top of these thin films.

- We demonstrated the use of SAWs, powerful fluid actuation and manipulation tools already part of the microfluidic arsenal, to drive fluid flow and induce uniform mixing in paper-based microfluidic channels. Though at the expense of introducing external forcing, we show that nonuniformities and poor reproducibility in passive mixing in paper networks that arise as a consequence of limitations unique to capillary-driven flow in paper can be circumvented to provide faster, more uniform, repeatable and predictable mixing on paper. In the process of examining various parameters that control the flow speed and mixing efficiency, such as input power, channel shape/tortousity and fibre/flow alignment, we also introduce a new hue-based colourimetric technique that allows for mixing quantification without limitations on the colour and contrast of the samples.

- A simpler and cheaper design was then developed and shown to be capable of not only driving many microfluidic applications such as drop mixing mixing, particle concentration and patterning with a drop but also 'high power' applications such as drop atomisation and atomisation through a wick. Ealier work for mixing on paper using SAW-driven atomisetion of the channel's end was replicated here using the much simpler and cheaper design, where, in some configureations only kitchen aluminium foil was cut into rectangles and brought into contact with the lithium niobate.
- At even higher frequencies ($\sim$ 100 MHz) the first ever observed, to the best of our knowledge, poloidal flow within a drop was produced where a shear induced migration mechanism was shown to consequently 'collapse' the poloidal flow into one single ring. The ring dimension was observed to be inversely proportion to the applied frequency, as the attenuation length decreases with higher frequencies.

5.2 FUTURE WORK

Aspects of the work proposed in chapter 4 where aluminium foil is brought into contact with lithium niobate substrate to generate sufficient vibrations for microfluidic actuation, although, ultra-simple, reliability of use is questionable due to the different electrode size used in every experiment, in addition to the varying contact force between the aluminium film and the LN in every experiment. Therefore, a simple and cheap yet reliable electrode configuration is indeed crucial. We have developed a simple way of printing our large scale electrodes on LN by simply transferring the pattern, which is originally printed on paper, to the LN through a standard plastic laminator instrument. The LN wafer wafer needs to be pre coated with metal, which can be achieved using a bench top gold sputter - for example the one used

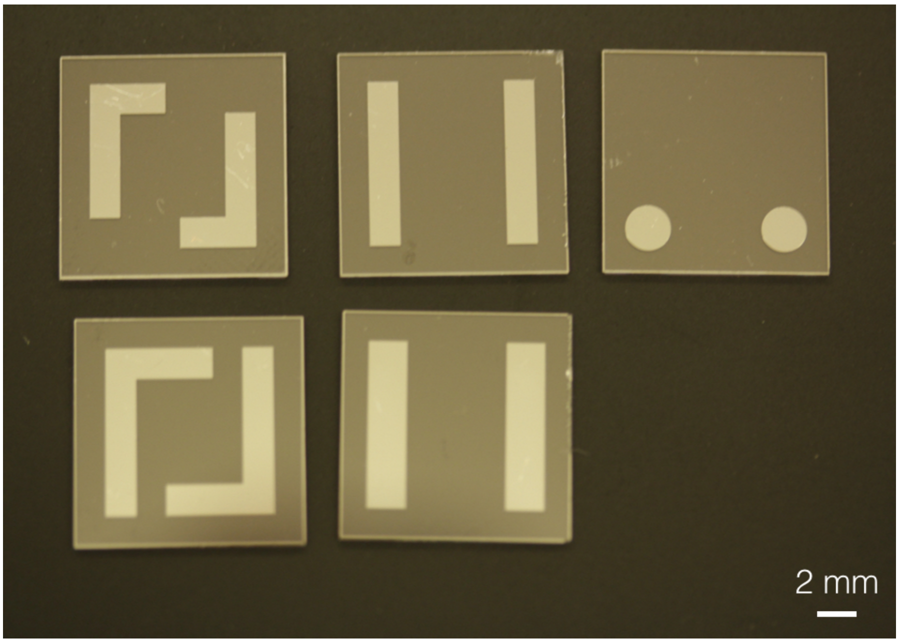

Figure 5.1: An image of the large electrodes patterned on lithium niobate substrate using a simple laminator.

to precoat sample for SEM - and followed by etching the remaining gold. The results are well defined large scale electrodes, as shown in figure. 5.1. Thorough study of different electrode configurations and which design is provides the most efficient power consumption is currently taking place.

Surface acoustic waves have traditionally been generated by the metal deposition of IDT, however, as explained earlier in the thesis, this possess the challenge of high fabrication const as well as the practical hurdle when conducting fluid come into contact with these IDT. Therefore, a different mechanism of generating SAW, without the need of depositing metal would be advantageous. Periodic polling of Lithium nioabte has been recently proposed by Professor Arnan Mitchell group, where I was partially involved in the project, using a novel UV irradiation mechanism. The results of this work is currently under review, however, further microfluidic actuation application using this novel platform, where UV light can be used to 'write' the electrodes is anticipated, especially for high frequency (100 MHz and beyond) applications, where, standard IDTs fail to provide sufficient power.

Part II

APPENDICES

APPENDIX A

A

MATLAB CODES FOR NUMERICS IN CHAPTER 2

%% pde_1_main.m is the main code to run and it calls initial_1.m and fourthDerivEx1.m. The former contains the initial function equaltion and the latter contains the fourth order equation function (or any less order function that is included) to be solved whch calls the other finite difference routines. pde_1_main.m also calls 'simpsons.m' which calculates the error %. Centre-difference method was used here, but forward and backward methods are also included but just commented.

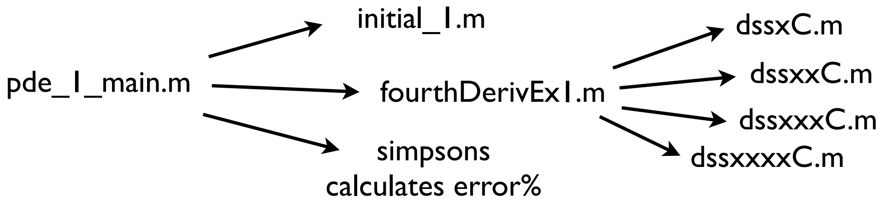

Figure A.1: flow chart for the code solving fourth order partial differential equation.

```
%% File name 'pde_1_main.m'
% Clear previous files
clear all
close all
clc
% Parameters shared with the ODE routine
global T ux uxxx n x xl xu d f s v uxx
% Parameters
n=101;
xl=0;
xu=1;
d = 50;
% Initial condition
t0=0.0;
u0=inital_1(t0);
% Independent variable for ODE integration
tf= .000222;
tout=[t0:tf/5:tf]';
% ODE integration
reltol=1.0e-7; abstol=1.0e-6;
options=odeset('RelTol',reltol,'AbsTol',abstol);
```

```
[t,u]=ode15s(@fourthDerivEx1,tout,u0,options);
figure(1);
plot(x,u,'b')
xlabel('x')
ylabel('u(x,t)')
for i = 1:length(tout)
T(i) = simpsons(u(i,:),xl,xu,1000000);
end
T
k = length(tout);
Dev = (T(1,k-1) - T(1,1))/ (T(1,k-1))
figure(2);
plot(x,ux)
%figure(3);
%plot(x,uxx);
figure(4);
plot(x,uxxx);
%figure(5);
%plot(x,uxxxx);
```

%% File name 'initial_1.m'

```
function u0=inital_1(t0)
% Function inital_1 sets the initial condition
global dx nl nu n x d xl xu ncall ncase ndss vis
% Analytical solution initially
u0=zeros(1,n);
dx=(xu-xl)/(n-1);
for i = 1:n
x(i)=xl+(i-1)*dx;
% u0(i) = exp(-x(i)^2/0.05);
% if i ==1
% u0(1) = 0;
% elseif i ==n
% u0(n) = 0.0001;
% else
% u0(i)= gaussmf(x(i),[0.05 0]) + .2;
% u0(i) = exp(-(x(i)).^2);
% u0(i) = roundn(u0(i),-d);
if i < 0.25*n
u0(i) = 10*((exp(-(1/16)/((x(i)+0.25))^2) * exp(-(1/16)/((x(i) - 0.25))^2)))...
```

```
+ 6.31*10^-5;
else
u0(i) = 6.31*10^-5;
end
% if i <= n/2
% u0(i) = -(x(i)^2) + 4;
% else
% u0(i) = 0;
% end
% u0(i) = (sech(4*x(i))^2);
% if i >= n/4  i <= (3*n)/4
% u0(i) = -cos(x(i)) + 0.001;
% else
% u0(i) = 0;
% end
% u0(i) = 0.8 - cos(pi*x(i))+ 0.25*cos(2*pi*x(i)) -0.05;
% else
% u0(i) = 0;
%end
% if i >= n/3  i <= (2*n)/3
% u0(i) = -x(i)^2 + 1;
%else
% u0(i) = 0;
%end
end
%u0(i) = round2(u0(i),1e-4);
```

%% File name 'fourthDerivEx1.m'

```
function [ut] = fourthDerivEx1(t,u)
global x n ux f v s uxx uxxx uxxxx ubl xl xu nl nu % Global variables
[ux] = dssxC(xl,xu,n,u);
[uxx] = dssxxC(xl,xu,n,u);
[uxxx] = dssxxxC(xl,xu,n,u);
[uxxxx] = dssxxxxC(xl,xu,n,u);
% [ux,uxx,uxxx,uxxxx] = dss(xl,xu,n,u);
f = zeros(1,n);
s = zeros(1,n);
ut = zeros(1,n);
v = zeros(1,n);
fst = zeros(1,n);
```

```
snd = zeros(1,n);
thd = zeros(1,n);
for i=1:n
% ut(i) = -2i*k*c*exp(2i*k*x(i))*exp(2i*w*t)*(u(i).^2) * ux(i) + ...
% (4/3)*(u(i).^3) * k * c * exp(2i * k * x(i)) * exp(2i * w * t)...
%- (u(i).^2) * (ux(i)) * uxxx(i) - (1/3) * (u(i).^3) * (uxxxx(i));
% ut(i) = - ux(i);
%fst(i) = ((((10^-14 * u(i)^3 + u(i)^4) * 7 * (u(i)^6 * ux(i))) - ...
% (u(i)^7 * (3 * 10^-14 * (u(i)^2 * ux(i)) + 4 * (u(i)^3) * ux(i))))...
%/((10^-14 * u(i)^3 + u(i)^4)^2)) * uxxx(i);
%snd(i) = (u(i)^7/(10^-14 * u(i)^3 + u(i)^4)) * uxxxx(i);
%thd(i) = (1.5*0.5*(u(i)^-0.5) * (ux(i)^2)) + (1.5 * u(i)^0.5 * uxx(i));
% if u(i) > .2;
% thd(i) = (18*pi*4*(u(i)^-5) * (ux(i)^2)) - (18 * pi * (u(i)^-4) * (uxx(i)));
% else
% thd(i) = 0;
% end
%thd(i) = (1/6*pi)*((-u(i)^-2 * ux(i) + (uxx(i)/u(i))));
fst(i) = - 3.*u(i)^2. * ux(i) * uxxx(i);
snd(i) = - u(i)^3. * uxxxx(i);
%v(i) = (-10^-5 * ux(i))/((u(i)^2)) + (10^-5 * uxx(i))/(u(i));
% v(i) = (10^-20/(6 * pi * u(i))) * ((ux(i)/u(i) + uxx(i)));
ut(i) = fst(i) + snd(i) + 0*thd(i);
%ut(i) = - fst(i) - snd(i) - thd(i);
% ut(i) = - 0.25*u(i)^2 * uxxx(i) - (1/12) * u(i)^3 * uxxxx(i);
% ut(i)= - (u(i)^3) * ux(i) - 3 * u(i).^2 * uxxx(i) - 3. * ...
% (u(i)).^3 * uxxxx(i);
end
ut=ut';
```

%% File name 'simpsons'

```
function I = simpsons(f,a,b,n)
```

% This function computes the integral "I" via Simpson's rule in the interval [a,b] with n+1 equally spaced points % % Syntax: I = simpsons(f,a,b,n) % % Where, % f= can be either an anonymous function (e.g. f=@(x) sin(x)) or a vector % containing equally spaced values of the function to be integrated % a= Initial point of interval % b= Last point of interval % n= of sub-intervals (panels), must be integer % % Written by Juan Camilo Medina - The University of Notre Dame % 09/2010 (copyright Dr. Simpson) % % % Example 1: % % Suppose you want to integrate a function f(x) in the interval [-1,1]. % You also want 3 integration points (2 panels) evenly distributed through the % domain (you can select more point for better accuracy). % Thus: % % f=@(x) ((x-1).*x./2).*((x-1).*x./2); % I=simpsons(f,-1,1,2) % % % Example 2: %

```
% Suppose you want to integrate a function f(x) in the interval [-1,1]. %
You know some values of the function f(x) between the given interval,
% those are fi= 1,0.518,0.230,0.078,0.014,0,0.006,0.014,0.014,0.006,0 %
Thus: % % fi= [1 0.518 0.230 0.078 0.014 0 0.006 0.014 0.014 0.006 0];
% I=simpsons(fi,-1,1,[]) % % note that there is no need to provide the
number of intervals (panels) "n", % since they are implicitly specified
by the number of elements in the % vector fi
  if numel(f)>1 % If the input provided is a vector
  n=numel(f)-1; h=(b-a)/n;
  I= h/3*(f(1)+2*sum(f(3:2:end-2))+4*sum(f(2:2:end))+f(end));
  else % If the input provided is an anonymous function
  h=(b-a)/n; xi=a:h:b;
  I= h/3*(f(xi(1))+2*sum(f(xi(3:2:end-2)))+4*sum(f(xi(2:2:end)))+ ...
  f(xi(end)));
  end
```

%% File name ’dssxC.m’

```
  function [ux]=dssxC(xl,xu,n,u)
  global x
  % Compute the spatial increment
  dx=(xu-xl)/(n-1);
  ux = zeros(1,n);
  % ux(1)=(-3*u(1) +4*u(2) - u(3))/(2*dx);
  %ux(1) = 0;
  for i=1:n
  if i == 1
  ux(i) = 0;
  elseif i == n
  ux(i) = 0;
  else
  ux(i)=(u(i+1)-u(i-1))/(2*dx);
  end
  end
  %ux(n) = 0;
  % ux(n)= (3*u(n) - 4*u(n-1) + u(n-2))/(2*dx);
  % figure(5)
  % plot(x,ux)
  % hold on
```

%% File name ’dssxxC.m’

```
  function [uxx]=dssxxC(xl,xu,n,u)
  % Grid spacing
  dx=(xu-xl)/(n-1);
  uxx = zeros(1,n);
  % uxx at the left boundary, without ux
```

```
uxx(1)=(-2*u(1)+ 2*u(2))/(dx^2);
% uxx at the right boundary, including ux
uxx(n)=(-2*u(n) + 2*u(n-1))/(dx^2);
% uxx at the interior grid points
for i=2:n-1
uxx(i)=(u(i+1)-2*u(i)+u(i-1))/(dx^2);
end
%% File name 'dssxxxC.m'
function [uxxx]=dssxxxC(xl,xu,n,u)
global x d
% Grid spacing
dx=(xu-xl)/(n-1);
uxxx = zeros(1,n);
% uxxx at the left boundary
%uxxx(1) = 0;
%uxxx(1) = roundn(uxxx(1),-d);
%centre
%uxxx(2) = 0;
%uxxx(2) = (u(4) - 2*u(3) - u(2) + 2*u(1))/(2*dx^3);
%centre reversed
%uxxx(2) = (-u(4) + 2*u(3) + u(2) - 2*u(1))/(2*dx^3);
% %forward
%uxxx(2) = (-5*u(2) + 18*u(3) - 24*u(4) + 14*u(5) - 3*u(6))/(3*dx^3);
%uxxx(2) = roundn(uxxx(2),-d);
% uxxx at the right boundary
%uxxx(n)=0;
%uxxx(n) = roundn(uxxx(n),-d);
%centre
%uxxx(n-1) = 0;
%uxxx(n-1) = (-2*u(n) + u(n-1) + 2*u(n-2) - u(n-3))/(2*dx^3);
%backward
%uxxx(n-1) = (5*u(n-1) - 18*u(n-2) + 24*u(n-3) - 14*u(n-4) + 3*u(n-5))/(3*dx^3);
%uxxx(n-1) = roundn(uxxx(n-1),-d);
% uxxx at the interior grid points
for i=1:n
if i == 1
uxxx(1) = 0;
elseif i == 2
uxxx(i) = (u(i+2) - 2*u(i+1) - u(i) + 2*u(i-1))/(2*dx^3);
elseif i == n
uxxx(n) = 0;
elseif i == n-1
```

```
uxxx(i) = (-2*u(i+1) + u(i) + 2*u(i-1) - u(i-2))/(2*dx^3);
else
uxxx(i)=(u(i+2)-2*u(i+1)+2.*u(i-1)- u(i-2))/(2*dx^3);
end
end
% figure(5)
% plot(x,uxxx)
% hold on
```

%% File name 'dssxxxxC.m'

```
function [uxxxx]=dssxxxxC(xl,xu,n,u)
global d
% Grid spacing
dx=(xu-xl)/(n-1);
uxxxx = zeros(1,n);
%left boundary centre
%uxxxx(1) = (2*u(3) - 8*u(2) + 6*u(1))/(dx^4);
%uxxxx(1) = roundn(uxxxx(1),-d);
%uxxxx(2) = (u(4) - 4*u(3) + 7*u(2) - 4*u(1))/(dx^4);
% uxxxx(2) = roundn(uxxxx(2),-d);
%forward
% uxxxx(1) = (3*u(1) - 14*u(2) + 26*u(3) - 24*u(4) + 11*u(5) - 2*u(6))/(dx^4);
% uxxxx(1) = roundn(uxxxx(1),-d);
% uxxxx(2) = (3*u(2) - 14*u(3) + 26*u(4) - 24*u(5) + 11*u(6) - 2*u(7))/(dx^4);
% uxxxx(2) = roundn(uxxxx(2),-d);
%backward
% uxxxx(n)= (3*u(n) - 14*u(n-1) + 26*u(n-2) - 24*u(n-3) + 11*u(n-4) - 2*u(n-5))/(dx^4);
% uxxxx(n) = roundn(uxxxx(n),-d);
% uxxxx(n-1) = (3*u(n-1) - 14*u(n-2) + 26*u(n-3) - 24*u(n-4) + 11*u(n-5) - 2*u(n-6))/(dx^4);
% uxxxx(n-1) = roundn(uxxxx(n-1),-d);
%right boundary centre
% uxxxx(n) = (6*u(n) - 8*u(n-1) + 2*u(n-2))/(dx^4);
% uxxxx(n) = roundn(uxxxx(n),-d);
% uxxxx(n-1)= (-4*u(n) + 7*u(n-1) - 4*u(n-2) + u(n-3))/(dx^4);
% uxxxx(n-1) = roundn(uxxxx(1),-d);
%uxxxx at the interior grid points
for i=1:n
if i == 1
uxxxx(i) = (2*u(i+2) - 8*u(i+1) + 6*u(i))/(dx^4);
elseif i == 2
uxxxx(i) = (u(i+2) - 4*u(i+1) + 7*u(i) - 4*u(i-1))/(dx^4);
elseif i == n
```

```
uxxxx(i) = (6*u(i) - 8*u(i-1) + 2*u(i-2))/(dx^4);
elseif i == n-1
uxxxx(i)= (-4*u(i+1) + 7*u(i) - 4*u(i-1) + u(i-2))/(dx^4);
else
uxxxx(i)=(u(i+2)- 4*u(i+1)+ 6*u(i) - 4*u(i-1) + u(i-2)) / (dx^4);
end
end
```

APPENDIX B

B

MATLAB CODES FOR MIXING IN CHAPTER 3

```
close all
  clear all
  clc
  N = 100;
  % IMAGES = cell(1,N);
  % base = ’base%d.jpg’;
  Hb = 198.56;
  Hy = 50.021;
  %Hg = 147;
  Hg = (Hb+Hy)/2;
  %%%%%%%%%%%%Allocating memory%%%%%%%%%%%%
  IMAGES = cell(1,N);
  %%%%%%%%%%%%%%%%%%%%%%%%%%%%%%%%%%%%%%%
  % Load images
  for k=1:N
  IMAGESk = imread(sprintf(’withsaw%03d.png’, k));
  end
  % Run code
  %%Locations corrdinates:
  %First
  fx1 =85;
  fx2 =93;
  fy1=501;
  fy2=510;
  ftot = ((fx2 - fx1)+1)*((fy2-fy1)+1);
  %
  %Second
  sx1 =84;
  sx2 =95;
  sy1=337;
  sy2=347;
  stot = ((sx2 - sx1)+1)*((sy2-sy1)+1);
  %Third
  thx1 =191;
  thx2 =199;
  thy1=402;
  thy2=452;
```

```
thtot = ((thx2 - thx1)+1)*((thy2-thy1)+1);
%Fourth
fox1 =357;
fox2 =362;
foy1=407;
foy2=441;
fotot = ((fox2 - fox1)+1)*((foy2-foy1)+1);
%Fifth
fix1 =532;
fix2 =537;
fiy1=406;
fiy2=440;
fitot = ((fix2 - fix1)+1)*((fiy2-fiy1)+1);
%Sixth
six1 =698;
six2 =702;
siy1=409;
siy2=443;
sitot = ((six2 - six1)+1)*((siy2-siy1)+1);
%Seventh
sex1 =864;
sex2 =868;
sey1=406;
sey2=448;
setot = ((sex2 - sex1)+1)*((sey2-sey1)+1);
%Eigth
eix1 =1030;
eix2 =1034;
eiy1=406;
eiy2=451;
eitot = ((eix2 - eix1)+1)*((eiy2-eiy1)+1);
%Ninth
nix1 =1357;
nix2 =1364;
niy1=406;
niy2=450;
nitot = ((nix2 - nix1)+1)*((niy2-niy1)+1);
%position 1
for k = 1:N
Te = IMAGESk;
T = rgb2hsv(Te);
%FIRST POSITION
h1(:,:,k)= T(fy1:fy2,fx1:fx2,1).*360;
```

```
for i = 1: (fy2 -fy1) +1;
for j = 1: (fx2-fx1) + 1
if h1(i,j,k)<= Hg
Hnorm1(i,j) = -1.*((h1(i,j,k)-Hy)./(Hg-Hy)) + 1 ;
else
Hnorm1(i,j) = ((h1(i,j,k)-Hg))./(Hb-Hg);
end
end
end
Hnormtrue1(k) = mean(mean(Hnorm1));
%Second POSITION
h2(:,:,k)= T(sy1:sy2,sx1:sx2,1).*360;
for i = 1: (sy2 -sy1) +1;
for j = 1: (sx2-sx1) + 1
if h2(i,j,k)<= Hg
Hnorm2(i,j) = -1.*((h2(i,j,k)-Hy)./(Hg-Hy)) + 1 ;
else
Hnorm2(i,j) = ((h2(i,j,k)-Hg))./(Hb-Hg);
end
end
end
Hnormtrue2(k) = mean(mean(Hnorm2));
%THIRD POSITION
h3(:,:,k)= T(thy1:thy2,thx1:thx2,1).*360;
for i = 1: (thy2 -thy1) +1;
for j = 1: (thx2-thx1) + 1
if h3(i,j,k)<= Hg
Hnorm3(i,j) = -1.*((h3(i,j,k)-Hy)./(Hg-Hy)) + 1 ;
else
Hnorm3(i,j) = ((h3(i,j,k)-Hg))./(Hb-Hg);
end
end
end
Hnormtrue3(k) = mean(mean(Hnorm3));
%FOURTH POSITION
h4(:,:,k)= T(foy1:foy2,fox1:fox2,1).*360;
for i = 1: (foy2 -foy1) +1;
for j = 1: (fox2-fox1) + 1
if h4(i,j,k)<= Hg
Hnorm4(i,j) = -1.*((h4(i,j,k)-Hy)./(Hg-Hy)) + 1 ;
else
Hnorm4(i,j) = ((h4(i,j,k)-Hg))./(Hb-Hg);
end
```

```
end
end
Hnormtrue4(k) = mean(mean(Hnorm4));
%FIFTH POSITION
h5(:,:,k)= T(fiy1:fiy2,fix1:fix2,1).*360;
for i = 1: (fiy2 -fiy1) +1;
for j = 1: (fix2-fix1) + 1
if h5(i,j,k)<= Hg
Hnorm5(i,j) = -1.*((h5(i,j,k)-Hy)./(Hg-Hy)) + 1 ;
else
Hnorm5(i,j) = ((h5(i,j,k)-Hg))./(Hb-Hg);
end
end
end
Hnormtrue5(k) = mean(mean(Hnorm5));
%SixTH POSITION
h6(:,:,k)= T(siy1:siy2,six1:six2,1).*360;
for i = 1: (siy2 -siy1) +1;
for j = 1: (six2-six1) + 1
if h6(i,j,k)<= Hg
Hnorm6(i,j) = -1.*((h6(i,j,k)-Hy)./(Hg-Hy)) + 1 ;
else
Hnorm6(i,j) = ((h6(i,j,k)-Hg))./(Hb-Hg);
end
end
end
Hnormtrue6(k) = mean(mean(Hnorm6));
%SeVENTH POSITION
h7(:,:,k)= T(sey1:sey2,sex1:sex2,1).*360;
for i = 1: (sey2 -sey1) +1;
for j = 1: (sex2-sex1) + 1
if h7(i,j,k)<= Hg
Hnorm7(i,j) = -1.*((h7(i,j,k)-Hy)./(Hg-Hy)) + 1 ;
else
Hnorm7(i,j) = ((h7(i,j,k)-Hg))./(Hb-Hg);
end
end
end
Hnormtrue7(k) = mean(mean(Hnorm7));
%EiGHTTH POSITION
h8(:,:,k)= T(eiy1:eiy2,eix1:eix2,1).*360;
for i = 1: (eiy2 -eiy1) +1;
for j = 1: (eix2-eix1) + 1
```

```
if h8(i,j,k)<= Hg
Hnorm8(i,j) = -1.*((h8(i,j,k)-Hy)./(Hg-Hy)) + 1 ;
else
Hnorm8(i,j) = ((h8(i,j,k)-Hg))./(Hb-Hg);
end
end
end
Hnormtrue8(k) = mean(mean(Hnorm8));
%NINTH POSITION
h9(:,:,k)= T(niy1:niy2,nix1:nix2,1).*360;
for i = 1: (niy2 -niy1) +1;
for j = 1: (nix2-nix1) + 1
if h9(i,j,k)<= Hg
Hnorm9(i,j) = -1.*((h9(i,j,k)-Hy)./(Hg-Hy)) + 1 ;
else
Hnorm9(i,j) = ((h9(i,j,k)-Hg))./(Hb-Hg);
end
end
end
Hnormtrue9(k) = mean(mean(Hnorm9));
end
% x = 1:N;
% plot(x,hnorm1,'+',x,h2(:,:,2),'o',x,h3(:,:,3),'+',x,h4(:,:,4),'o',...
% x,h5(:,:,5),'+')
% % ,x,H(:,6),'o',x,H(:,7),'+',x,H(:,8),'o',...
% % x,H(:,9),'o')
% title('HUE angle change over time')
% hold on
% xlabel('Frame (time)')
% ylabel('HUE angle')
% legend ('position1', 'position2', 'position3', 'position4', ...
% 'position5', 'position6', 'position7','position8','position9')
x = 1:N;
figure
plot(x,Hnormtrue1,'+',x,Hnormtrue2,'o',x,Hnormtrue3,'+',x,Hnormtrue4,'o',...
x,Hnormtrue5,'+',x,Hnormtrue6,'o',x,Hnormtrue7,'+',x,Hnormtrue8,'o',...
x,Hnormtrue9,'+')
title('Normalised HUE angle change over time')
hold on
xlabel('Frame (time)')
ylabel('Normalised HUE angle')
legend ('position1', 'position2', 'position3', 'position4', 'position5'...
, 'position6', 'position7', 'position8' , 'position9')
```

```
H = [Hnormtrue1; Hnormtrue2; Hnormtrue3; Hnormtrue4; Hnormtrue5;...
Hnormtrue6; Hnormtrue7; Hnormtrue8; Hnormtrue9];
x = [1;2;3;4;5;6;7;8;9;];
figure, plot(x,H,’+’);
```

BIBLIOGRAPHY

[1] K Abe, K Suzuki, and D Citterio. Inkjet-printed microfluidic multianalyte chemical sensing paper. *Analytical Chemistry*, 80 (18):6928–6934, 2008. (Cited on page 64.)

[2] K Abi-Samra, L Clime, L Kong, R Gorkin III, T-H Kim, Y-K Cho, and M Madou. Thermo-pneumatic pumping in centrifugal microfluidic platforms. *Microfluidics and nanofluidics*, 11(5):643–652, 2011. (Cited on page 5.)

[3] D Ahmed, X Mao, BK Juluri, and TJ Huang. A fast microfluidic mixer based on acoustically driven sidewall-trapped microbubbles. *Microfluidics and nanofluidics*, 7(5):727–731, 2009. (Cited on page 6.)

[4] D Ahmed, X Mao, J Shi, BK Juluri, and TJ Haung. A millisecond micromixer via single-bubble-based acoustic streaming. *Lab on a Chip*, 9(18):2738–2741, 2009. (Cited on page 6.)

[5] AT Al-Halhouli, MI Kilani, and S Büttgenbach. Development of a novel electromagnetic pump for biomedical applications. *Sensors and Actuators A: Physical*, 162(2):172–176, 2010. (Cited on page 5.)

[6] M Alvarez, JR Friend, and LY Yeo. Surface vibration induced spatial ordering of periodic polymer patterns on a substrate. *Langmuir*, 24(19):10629–10632, 2008. (Cited on pages 15 and 23.)

[7] M Alvarez, JR Friend, and LY Yeo. Rapid generation of protein aerosols and nanoparticles via surface acoustic wave atomization. *Nanotechnology*, 19(45):455103, 2008. (Cited on page 15.)

[8] M Alvarez, LY Yeo, JR Friend, and M Jamriska. Rapid production of protein-loaded biodegradable microparticles using surface acoustic waves. *Biomicrofluidics*, 3:014102, 2009. (Cited on page 15.)

[9] S Alzuaga, J-F Manceau, and F Bastien. Motion of droplets on solid surface using acoustic radiation pressure. *J. Sound Vib.*, 282:151–162, 2005. (Cited on pages 23 and 80.)

[10] RMI Arzt, E Salzmann, and K Dransfeld. Elastic surface waves in quartz at 316 MHz. *Appl. Phys. Lett.*, 10:165–167, Feb 1967. (Cited on page 37.)

[11] DR Ballerini, X Li, and W Shen. Flow control concepts for thread-based microfluidic devices. *Biomicrofluidics*, 5(1):014105, 2011. doi: DOI:10.1063/1.3567094. URL `http://dx.doi.org/doi/10.1063/1.3567094`. (Cited on page 71.)

[12] CN Baroud, MR de Saint Vincent, and J-P Delville. An optical toolbox for total control of droplet microfluidics. *Lab on a Chip*, 7(8):1029–1033, 2007. (Cited on page 8.)

[13] Amar S Basu and Yogesh B Gianchandani. Virtual microfluidic traps, filters, channels and pumps using marangoni flows. *Journal of Micromechanics and Microengineering*, 18(11):115031, 2008. (Cited on page 7.)

[14] GK Batchelor. *An Introduction to Fluid Dynamics*. Cambridge University, Cambridge, 1967. (Cited on page 24.)

[15] HH Bau, J Zhong, and M Yi. A minute magneto hydro dynamic (mhd) mixer. *Sensors and Actuators B: Chemical*, 79(2):207–215, 2001. (Cited on pages 6 and 8.)

[16] WL Benard, H Kahn, AH Heuer, and MA Huff. Thin-film shape-memory alloy actuated micropumps. *Microelectromechanical Systems, Journal of*, 7(2):245–251, 1998. (Cited on page 5.)

[17] TB Benjamin and F Ursell. The stability of the plane free surface of a liquid in vertical periodic motion. *Proc. R. Soc. Lond. A*, 225: 505–515, 1954. (Cited on page 24.)

[18] J Bennès, S Alzuaga, P Chabé, G Morain, F Chérioux, J-F Manceau, and F Bastien. Action of low frequency vibration on liquid droplets and particles. *Ultrasonics*, 44:e497–e502, 2006. (Cited on pages 23 and 24.)

[19] D Benny. Long waves on liquid films. *J. Math. Phys.*, 45:150–155, 11 1966. (Cited on pages 32, 34, and 38.)

[20] PK Bhattacharjee, AG McDonnell, R Prabhakar, LY Yeo, and JR Friend. Extensional flow of low-viscosity fluids in capillary bridges formed by pulsed surface acoustic wave jetting. *New Journal of Physics*, 13(2):023005, 2011. (Cited on page 15.)

[21] S Biwersi, JF Manceau, and F Bastien. Displacement of droplets and deformation of thin liquid layers using flexural vibrations of structures. Influence of acoustic radiation pressure. *J. Acoust. Soc. Am.*, 107:661–664, 2000. (Cited on pages 23 and 24.)

[22] J Blamey, LY Yeo, and JR Friend. Microscale capillary wave turbulence excited by high frequency vibration. *Langmuir*, 29 (11):3835–3845, 2013. (Cited on page 95.)

[23] FE Borgnis. Acoustic radiation pressure of plane compressional waves. *Rev. Mod. Phys.*, 25:653–664, 2010. (Cited on page 42.)

[24] E Bormashenko, R Pogreb, G Whyman, and M Erlich. Cassie–Wenzel wetting transition in vibrating drops deposited on rough surfaces: Is the dynamic Cassie–Wenzel wetting transition a 2D or 1D affair? *Langmuir*, 23:6501–6503, 2007. (Cited on page 23.)

[25] Y Bourquin, J Reboud, R Wilson, Y Zhang, and JM Cooper. Integrated immunoassay using tuneable surface acoustic waves and lensfree detection. *Lab on a Chip*, 11:2725–2730, 2011. (Cited on pages 15 and 81.)

[26] P Brunet, J Eggers, and R Deegan. Vibration-induced climbing of drops. *Phys. Rev. Lett.*, 99:144501, 2007. doi: 10.1103/PhysRevLett.99.144501. (Cited on pages 23 and 24.)

[27] P Brunet, J Eggers, and RD Deegan. Motion of a drop driven by substrate vibrations. *Euro. Phys. J.-Special Topics*, 166:11–14, 2009. (Cited on pages 23 and 24.)

[28] P Brunet, M Baudoin, OB Matar, and F Zoueshtiagh. Droplet displacements and oscillations induced by ultrasonic surface acoustic waves: A quantitative study. *Phys. Rev. E*, 81:036315, Mar 2010. doi: 10.1103/PhysRevE.81.036315. URL `http://link.aps.org/doi/10.1103/PhysRevE.81.036315`. (Cited on pages 13, 55, 94, and 96.)

[29] JWM Bush, HA Stone, and J Bloxham. Axial drop motion in rotating fluids. *Journal of Fluid Mechanics*, 282(1):247–278, 1995. (Cited on page 89.)

[30] F Cabaret, S Bonnot, L Fradette, and PA Tanguy. Mixing time analysis using colorimetric methods and image processing. *Industrial & Engineering Chemistry Research*, 46(14):5032–5042, 2007. (Cited on pages 65 and 68.)

[31] JJ Campbell. Propagation of surface waves at the boundary between a piezoelectric crystal and a fluid medium. *IEEE Trans. Sonics Ultrason.*, 17:71–76, 1970. (Cited on page 55.)

[32] H-C Chang and LY Yeo. *Electrokinetically driven microfluidics and nanofluidics*. Cambridge University Press Cambridge, UK:, 2010. (Cited on page 7.)

[33] JDN Cheeke. *Fundamentals and applications of ultrasonic waves*. CRC press, 2012. (Cited on page 94.)

[34] PY Chiou, AT Ohta, and MC Wu. Massively parallel manipulation of single cells and microparticles using optical images. *Nature*, 436(7049):370–372, 2005. (Cited on page 8.)

[35] BT Chu and RE Apfel. Acoustic radiation pressure produced by a beam of sound. *J. Acoust. Soc. Am.*, 72:1673–1687, 1982. (Cited on pages 31, 42, and 43.)

[36] D Collins, O Manor, A Winkler, H Schmidt, JR Friend, and LY Yeo. Atomization off thin water films generated by high-frequency substrate wave vibrations. *Phys. Rev. E*, 86:056312, November 2012. (Cited on pages 17, 18, 23, 25, 42, and 43.)

[37] RV Craster and OK Matar. Dynamics and stability of thin liquid films. *Rev. Mod. Phys.*, 81:1131–1198, August 2009. (Cited on pages 32 and 34.)

[38] S Daniel, MK Chaudhury, and PG DeGennes. Vibration-actuated drop motion on surfaces for batch microfluidic processes. *Langmuir*, 21:4240–4248, 2005. (Cited on pages 23 and 24.)

[39] Anton A Darhuber and Sandra M Troian. Principles of microfluidic actuation by modulation of surface stresses. *Annu. Rev. Fluid Mech.*, 37:425–455, 2005. (Cited on page 7.)

[40] PG de Gennes. Wetting: statics and dynamics. *Rev. Mod. Phys.*, 57:827–863, 1985. (Cited on page 24.)

[41] J-P Delville, MR de Saint Vincent, RD Schroll, H Chraïbi, B Issenmann, R Wunenburger, D Lasseux, WW Zhang, and E Brasselet. Laser microfluidics: fluid actuation by light. *Journal of Optics A: Pure and Applied Optics*, 11(3):034015, 2009. (Cited on page 8.)

[42] MB Dentry, LY Yeo, and JR Friend. Frequency effects on the scale and behavior of acoustic streaming. *Physical Review E*, In Review, 2013. (Cited on pages 90 and 95.)

[43] K Dholakia, G Spalding, and M MacDonald. Optical tweezers: the next generation. *Physics world*, 15(10):31–36, 2002. (Cited on page 8.)

[44] MA Dineva, D Candotti, F Fletcher-Brown, J-P Allain, and H Lee. Simultaneous visual detection of multiple viral amplicons by dipstick assay. *Journal of Clinical Microbiology*, 43(8):4015–4021, 2005. (Cited on page 65.)

[45] X Ding, S-C Steven Lin, B Kiraly, H Yue, S Li, I-K Chiang, J Shi, SJ Benkovic, and TJ Huang. On-chip manipulation of single microparticles, cells, and organisms using surface acoustic waves. *Proceedings of the National Academy of Sciences*, 2012. doi: 10.1073/pnas.1209288109. (Cited on page 89.)

[46] X Ding, P Li, S-CS Lin, ZS Stratton, N Nama, F Guo, D Slotcavage, X Mao, J Shi, F Costanzo, and TJ Haung. Surface acoustic wave microfluidics. *Lab on a Chip*, 13:3626–3649, 2013. (Cited on pages 81 and 86.)

[47] SS Dixit, H Kim, A Vasilyev, A Eid, and GW Faris. Light-driven formation and rupture of droplet bilayers. *Langmuir*, 26(9):6193–6200, 2010. (Cited on page 8.)

[48] EB Dussan V and RTP Chow. On the ability of drops or bubbles to stick to non-horizontal surfaces of solids. *J. Fluid Mech.*, 137: 1–29, 1983. (Cited on page 24.)

[49] C Eckart. Vortices and streams caused by sound waves. *Phys. Rev.*, 73:68–76, 1948. (Cited on pages 11, 27, 31, 94, and 96.)

[50] JCT Eijkel, C Dalton, CJ Hayden, JPH Burt, and A Manz. A circular ac magnetohydrodynamic micropump for chromatographic applications. *Sensors and Actuators B: Chemical*, 92(1):215–221, 2003. (Cited on page 8.)

[51] Y Fainman, L Lee, D Psaltis, and C Yang. *Optofluidics: fundamentals, devices, and applications*. McGraw-Hill New York:, 2010. (Cited on page 8.)

[52] IS Fayzrakhmanova and AV Straube. Stick-slip dynamics of an oscillated sessile drop. *Phys. Fluids*, 21:072104, 2009. (Cited on pages 23 and 24.)

[53] EM Fenton, MR Mascarenas, GP LoÌĄpez, and SS Sibbett. Multiplex lateral-flow test strips fabricated by two-dimensional shaping. *ACS Applied Materials & Interfaces*, 1(1):124–129, 2009. doi: 10.1021/am800043z. URL `http://pubs.acs.org/doi/abs/10.1021/am800043z`. PMID: 20355763. (Cited on page 64.)

[54] M Focke, D Kosse, C Müller, H Reinecke, R Zengerle, and F von Stetten. Lab-on-a-foil: microfluidics on thin and flexible films. *Lab on a Chip*, 10(11):1365–1386, 2010. (Cited on page 81.)

[55] AM Forte and WR Peltier. The kinematics and dynamics of poloidal-toroidal coupling in mantle flow: The importance of surface plates and lateral viscosity variations. *Advances in Geophysics*, 36:1–119, 1994. (Cited on page 89.)

[56] T Franke, AR Abate, DA Weitz, and A Wixforth. Surface acoustic wave (saw) directed droplet flow in microfluidics for pdms devices. *Lab on a Chip*, 9(18):2625–2627, 2009. (Cited on page 14.)

[57] T Franke, S Braunmüller, L Schmid, A Wixforth, and DA Weitz. Surface acoustic wave actuated cell sorting (sawacs). *Lab on a Chip*, 10:789–794, 2010. (Cited on pages 14 and 81.)

[58] JR Friend and LY Yeo. Microscale acoustofluidics: Microfluidics driven via acoustics and ultrasonics. *Rev. Mod. Phys.*, 83:647–704, Jun 2011. doi: 10.1103/RevModPhys.83.647. URL `http://link.aps.org/doi/10.1103/RevModPhys.83.647`. (Cited on pages 6, 10, 12, 24, 31, 42, 55, 64, 81, 86, 87, 89, and 90.)

[59] JR Friend, LY Yeo, DR Arifin, and A Mechler. Evaporative self-assembly assisted synthesis of polymeric nanoparticles by surface acoustic wave atomization. *Nanotechnology*, 19(14):145301, 2008. (Cited on page 15.)

[60] T Frommelt, M Kostur, M Wenzel-Schäfer, P Talkner, P Hänggi, and A Wixforth. Microfluidic mixing via acoustically driven chaotic advection. *Phys. Rev. Lett.*, 100:034502, Jan 2008. doi: 10.1103/PhysRevLett.100.034502. URL `http://link.aps.org/doi/10.1103/PhysRevLett.100.034502`. (Cited on pages 76 and 89.)

[61] E Fu, P Kauffman, B Lutz, and P Yager. Chemical signal amplification in two-dimensional paper networks. *Sensors and Actuators B: Chemical*, 149(1):325–328, 2010. ISSN 0925-4005. doi: DOI:10.1016/j.snb.2010.06.024. URL `http://www.sciencedirect.com/science/article/pii/S0925400510005010`. (Cited on page 64.)

[62] E Fu, B Lutz, P Kauffman, and P Yager. Controlled reagent transport in disposable 2d paper networks. *Lab on a Chip*, 10(7):918–920, 2010. (Cited on page 64.)

[63] E Fu, S Ramsey, P Kauffman, B Lutz, and P Yager. Transport in two-dimensional paper networks. *Microfluidics and Nanofluidics*, 10:29–35, 2011. ISSN 1613-4982. URL `http://dx.doi.org/10.1007/s10404-010-0643-y`. 10.1007/s10404-010-0643-y. (Cited on page 71.)

[64] L Gervais and E Delamarche. Toward one-step point-of-care immunodiagnostics using capillary-driven microfluidics and pdms substrates. *Lab on a Chip*, 9(23):3330–3337, 2009. (Cited on page 7.)

[65] NR Glass, RJ Shilton, PPY Chan, JR Friend, and LY Yeo. Miniaturized lab-on-a-disc (miniload). (Cited on pages 14 and 83.)

[66] R Gorkin III, L Clime, M Madou, and H Kido. Pneumatic pumping in centrifugal microfluidic platforms. *Microfluidics and Nanofluidics*, 9(2-3):541–549, 2010. (Cited on page 5.)

[67] RD Gregory and I Gladwell. The reflection of a symmetric rayleigh-lamb wave at the fixed or free edge of a plate. *Journal of Elasticity*, 13(2):185–206, 1983. (Cited on page 90.)

[68] DG Grier. Optical tweezers in colloid and interface science. *Current opinion in colloid & interface science*, 2(3):264–270, 1997. (Cited on page 8.)

[69] WH Grover, RHC Ivester, EC Jensen, and RA Mathies. Development and multiplexed control of latching pneumatic valves using microfluidic logical structures. *Lab on a Chip*, 6(5):623–631, 2006. (Cited on page 5.)

[70] NR Harris, M Hill, R Townsend, NM White, and SP Beeby. Performance of a micro-engineered ultrasonic particle manipulator. *Sensors and Actuators B: Chemical*, 111:481–486, 2005. (Cited on page 80.)

[71] SJ Hart and AV Terray. Refractive-index-driven separation of colloidal polymer particles using optical chromatography. *Applied physics letters*, 83(25):5316–5318, 2003. (Cited on page 8.)

[72] SJ Hart, A Terray, J Arnold, and TA Leski. Sample concentration using optical chromatography. *Optics express*, 15(5):2724–2731, 2007. (Cited on page 8.)

[73] T Hasegawa, T Kido, T Iizuka, and C Matsuoka. A general theory of Rayleigh and Langevin radiation pressure. *J. Acoust. Soc. Jap. E*, 21:146–152, 2000. (Cited on page 42.)

[74] A Hashmi, G Yu, M Reilly-Collette, G Heiman, and J Xu. Oscillating bubbles: a versatile tool for lab on a chip applications. *Lab on a Chip*, 12(21):4216–4227, 2012. (Cited on pages 6 and 80.)

[75] JJ Hawkes and WT Coakley. Force field particle filter, combining ultrasound standing waves and laminar flow. *Sensors and Actuators B: Chemical*, 75(3):213–222, 2001. (Cited on page 80.)

[76] SR Heron, R Wilson, SA Shaffer, DR Goodlett, and JM Cooper. Surface acoustic wave nebulization of peptides as a microfluidic interface for mass spectrometry. *Analytical chemistry*, 82(10):3985–3989, 2010. (Cited on pages 15 and 65.)

[77] J Ho, MK Tan, DB Go, LY Yeo, JR Friend, and H-C Chang. Paper-based microfluidic surface acoustic wave sample delivery and ionization source for rapid and sensitive ambient mass spectrometry. *Analytical chemistry*, 83(9):3260–3266, 2011. (Cited on pages 15 and 65.)

[78] LM Hocking. Waves produced by a vertically oscillating plate. *J. Fluid Mech.*, 179:267–281, 1987. (Cited on page 24.)

[79] LM Hocking. The damping of capillary–gravity waves at a rigid boundary. *J. Fluid Mech.*, 179:253–266, 1987. (Cited on page 24.)

[80] RP Hodgson, MK Tan, LY Yeo, and JR Friend. Transmitting high power rf acoustic radiation via fluid couplants into superstrates for microfluidics. *Applied Physics Letters*, 94(2):024102, 2009. doi: 10.1063/1.3049128. (Cited on pages 14 and 90.)

[81] J Holtsmark, I Johnsen, T Sikkeland, and S Skavl. Boundary layer flow near a cylindrical obstacle in an oscillating, incompressible fluid. *J. Acoust. Soc. Am.*, 26:26–39, Oct 1954. (Cited on page 24.)

[82] N Ichikawa, K Hosokawa, and R Maeda. Interface motion of capillary-driven flow in rectangular microchannel. *Journal of colloid and interface science*, 280(1):155–164, 2004. (Cited on page 7.)

[83] EF Jaeger, LA Berry, JR Myra, DB Batchelor, E D'Azevedo, PT Bonoli, CK Phillips, DN Smithe, DA D'Ippolito, MD Carter, et al. Sheared poloidal flow driven by mode conversion in tokamak plasmas. *Physical review letters*, 90(19):195001, 2003. (Cited on page 89.)

[84] J Jang and SS Lee. Theoretical and experimental study of mhd (magnetohydrodynamic) micropump. *Sensors and Actuators A: Physical*, 80(1):84–89, 2000. (Cited on page 8.)

[85] L-S Jang, Y-J Li, S-J Lin, Y-C Hsu, W-S Yao, M-C Tsai, and C-C Hou. A stand-alone peristaltic micropump based on piezoelectric actuation. *Biomedical microdevices*, 9(2):185–194, 2007. (Cited on page 5.)

[86] OC Jeong and SS Yang. Fabrication and test of a thermopneumatic micropump with a corrugated< i> p</i>+ diaphragm. *Sensors and Actuators A: Physical*, 83(1):249–255, 2000. (Cited on page 5.)

[87] Y Jin and SG Joshi. Characteristics of ultrasonic Lamb waves in 128/spl deg/rotated Y-cut lithium niobate. *... and Frequency Control*, 1994. (Cited on page 93.)

[88] Yu Jin and SG Joshi. Characteristics of ultrasonic lamb waves in 128/spl deg/rotated y-cut lithium niobate. *IEEE Transactions on Ultrasonics, Ferroelectrics and Frequency Control*, 41(2):279–283, 1994. (Cited on page 84.)

[89] L Johansson, J Enlund, S Johansson, I Katardjiev, M Wiklund, and V Yantchev. Surface acoustic wave-induced precise particle manipulation in a trapezoidal glass microfluidic channel. *Journal of Micromechanics and Microengineering*, 22(2):025018, 2012. (Cited on page 14.)

[90] DA Johnson and DL Feke. Methodology for fractionating suspended particles using ultrasonic standing wave and divided flow fields. *Separations Technology*, 5(4):251–258, 1995. (Cited on page 80.)

[91] TJ Johnson, D Ross, and LE Locascio. Rapid microfluidic mixing. *Analytical Chemistry*, 74(1):45–51, 2001. (Cited on page 76.)

[92] SM Kenyon, MM Meighan, and MA Hayes. Recent developments in electrophoretic separations on microfluidic devices. *Electrophoresis*, 32(5):482–493, 2011. (Cited on page 7.)

[93] J-H Kim, B-G Kim, H Nam, D-E Park, K-S Yun, J-B Yoon, J You, and E Yoon. A disposable dna sample preparation microfluidic chip for nucleic acid probe assay. In *Proceedings of the Fifteenth IEEE International Conference on Micro Electro Mechanical Systems*, pages 133–136, 2002. doi: 10.1109/MEMSYS.2002.984222. (Cited on page 65.)

[94] J-H Kim, K-H Na, CJ Kang, and Y-S Kim. A disposable thermopneumatic-actuated micropump stacked with pdms layers and ito-coated glass. *Sensors and Actuators A: Physical*, 120(2): 365–369, 2005. (Cited on page 5.)

[95] LV King. On the acoustic radiation pressure on spheres. *Proc. R. Soc. Lond. A*, 147:212–240, 1934. (Cited on pages 31 and 42.)

[96] M Koch, N Harris, AG Evans, NM White, and A Brunnschweiler. A novel micromachined pump based on thick-film piezoelectric actuation. *Sensors and Actuators A: Physical*, 70(1):98–103, 1998. (Cited on page 5.)

[97] W Krantz and S Goren. Finite-amplitude, long waves on liquid films flowing down a plane. *Ind. Eng. Chem. Fundam.*, 9:107–113, 1970. (Cited on page 32.)

[98] K Kulkarni, JR Friend, LY Yeo, and P. Perlmutter. Surface acoustic wave assisted drop-scale synthetic chemistry. *Lab on a Chip*, 9 (6):754–745, 2009. (Cited on page 14.)

[99] KP Kulkarni, SH Ramarathinam, JR Friend, LY Yeo, AW Purcell, and P Perlmutter. Rapid microscale in-gel processing and digestion of proteins using surface acoustic waves. *Lab on a Chip*, 10 (12):1518–1520, 2010. (Cited on page 14.)

[100] SM Langelier, LY Yeo, and JR Friend. Uv epoxy bonding for enhanced saw transmission and microscale acoustofluidic integration. *Lab on a Chip*, 12(16):2970–2976, 2012. (Cited on page 14.)

[101] T Laurell, F Petersson, and A Nilsson. Chip integrated strategies for acoustic separation and manipulation of cells and particles. *Chemical Society Reviews*, 36(3):492–506, 2007. (Cited on page 81.)

[102] IM Lazar and Barry L Karger. Multiple open-channel electroosmotic pumping system for microfluidic sample handling. *Analytical chemistry*, 74(24):6259–6268, 2002. (Cited on page 7.)

[103] D Leighton and A Acrivos. Shear-induced migration of particles in concentrated suspensions. *Journal of Fluid Mechanics*, 181(1): 415–439, 1987. (Cited on page 98.)

[104] AV Lemoff and AP Lee. An ac magnetohydrodynamic micropump. *Sensors and Actuators B: chemical*, 63(3):178–185, 2000. (Cited on page 8.)

[105] DR Li, Xand Ballerini and W Shen. A perspective on paper-based microfluidics: Current status and future trends. *Biomicrofluidics*, 6:012810, 2012. (Cited on page 81.)

[106] H Li, JR Friend, and LY Yeo. Surface acoustic wave concentration of particle and bioparticle suspensions. *Biomedical Microdevices*, 9(5):647–656, 2007. ISSN 1387-2176. doi: 10.1007/s10544-007-9058-2. URL `http://dx.doi.org/10.1007/s10544-007-9058-2`. (Cited on page 13.)

[107] H Li, JR Friend, and LY Yeo. A scaffold cell seeding method driven by surface acoustic waves. *Biomaterials*, 28(28):4098–4104, 2007. (Cited on page 13.)

[108] H Li, JR Friend, and LY Yeo. Surface acoustic wave concentration of particle and bioparticle suspensions. *Biomedical Microdevices*, 9:647–656, 2007. ISSN 1387-2176. URL `http://dx.doi.org/10.1007/s10544-007-9058-2`. 10.1007/s10544-007-9058-2. (Cited on page 76.)

[109] H Li, JR Friend, and LY Yeo. Microfluidic colloidal island formation and erasure induced by surface acoustic wave radiation. *Phys. Rev. Lett.*, 101:084502, 2008. (Cited on pages 13, 89, and 90.)

[110] W Liang and G Lindner. Investigations of droplet movement excited by lamb waves on a non-piezoelectric substrate. *Journal of Applied Physics*, 114(4):044501, 2013. (Cited on page 90.)

[111] J Lighthill. Acoustic streaming. *J. Sound Vib.*, 61:391–418, Jun 1978. (Cited on pages 27 and 31.)

[112] Sir James Lighthill. Acoustic streaming. *Journal of Sound and Vibration*, 61(3):391–418, 1978. (Cited on page 11.)

[113] S-CS Lin, X Mao, and TJ Huang. Surface acoustic wave (saw) acoustophoresis: now and beyond. *Lab on a Chip*, 12:2766–2770, 2012. (Cited on pages 81 and 86.)

[114] SS Lin, X Mao, and TJ Huang. Surface acoustic wave (saw) acoustophoresis: now and beyond. *Lab Chip*, 12:2766–2770, 2012. doi: 10.1039/C2LC90076A. URL `http://dx.doi.org/10.1039/C2LC90076A`. (Cited on pages 12, 24, and 89.)

[115] RH Liu, MA Stremler, KV Sharp, MG Olsen, JG Santiago, RJ Adrian, H Aref, and DJ Beebe. Passive mixing in a three-dimensional serpentine microchannel. *Journal of Microelectromechanical Systems*, 9(2):190–197, 2000. (Cited on pages 65 and 68.)

[116] Y Liu and K Lim. Particle separation in microfluidics using a switching ultrasonic field. *Lab on a Chip*, 11(18):3167–3173, 2011. (Cited on page 80.)

[117] MS Longuet-Higgins. Mass transport in water waves. *Philos. Trans. R. Soc. Lond.*, 245:535–581, Dec 1953. (Cited on page 24.)

[118] P Luginbuhl, SD Collins, G-A Racine, M-A Gretillat, NF De Rooij, KG Brooks, and N Setter. Microfabricated lamb wave device based on pzt sol-gel thin film for mechanical transport of solid particles and liquids. *Microelectromechanical Systems, Journal of*, 6 (4):337–346, 1997. (Cited on pages 6 and 79.)

[119] T-D Luong and N-T Nguyen. Surface acoustic wave driven microfluidics — a review. *Micro and Nanosystems*, 2:217–225, 2010. (Cited on pages 81 and 86.)

[120] TD Luong, VN Phan, and NT Nguyen. High-throughput micromixers based on acoustic streaming induced by surface acoustic wave. *Microfluidics and Nanofludics*, 10:619–625, 2011. (Cited on page 76.)

[121] DV Lyubimov, TP Lyubimova, and SV Shklyaev. Behavior of a drop on an oscillating solid plate. *Phys. Fluids*, 18:012101, 2006. doi: 10.1063/1.2137358. (Cited on page 23.)

[122] A Machauf, Y Nemirovsky, and U Dinnar. A membrane micropump electrostatically actuated across the working fluid. *Journal of Micromechanics and Microengineering*, 15(12):2309, 2005. (Cited on page 6.)

[123] M Madou, G Zoval, Jand Jia, H Kido, J Kim, and N Kim. Lab on a cd. *Annu. Rev. Biomed. Eng.*, 8:601–628, 2006. (Cited on page 14.)

[124] P Mandal, R Dey, and S Chakraborty. Electrokinetics with Òpaper-and-pencilÓ devices. *Lab on a Chip*, 12(20):4026–4028, 2012. (Cited on page 81.)

[125] O Manneberg, S Melker Hagsäter, J Svennebring, HM Hertz, JP Kutter, H Bruus, and M Wiklund. Spatial confinement of ultrasonic force fields in microfluidic channels. *Ultrasonics*, 49 (1):112–119, 2009. (Cited on page 80.)

[126] O Manor, MB Dentry, JR Friend, and LY Yeo. Substrate dependent drop deformation and wetting under high frequency vibration. *Soft Matter*, 7:7976–7979, 2011. (Cited on pages 23, 25, 60, and 80.)

[127] O Manor, LY Yeo, and JR Friend. Boundary Layers and drift flows under the excitation of High Frequency Surface Waves. *J. Fluid Mech.*, 707:482–495, 2012. (Cited on pages 24, 31, 32, 34, and 95.)

[128] D Mark, S Haeberle, R Günter, F von Stetten, and R Zengerle. Microfluidic lab-on-a-chip platforms: requirements, characteristics and applications. *Chemical Society Reviews*, 39(3):1153–1182, 2010. (Cited on page 81.)

[129] AW Martinez, ST Phillips, MJ Butte, and GM Whitesides. Patterned paper as a platform for inexpensive, low-volume, portable bioassays. *Angewandte Chemie International Edition*, 46(8): 1318–1320, 2007. ISSN 1521-3773. doi: 10.1002/anie.200603817.

URL http://dx.doi.org/10.1002/anie.200603817. (Cited on page 64.)

[130] AW Martinez, ST Phillips, and GM Whitesides. Three-dimensional microfluidic devices fabricated in layered paper and tape. *Proceedings of the National Academy of Sciences USA*, 105 (50):19606–19611, 2008. (Cited on page 64.)

[131] AW Martinez, ST Phillips, BJ Wiley, M Gupta, and GM Whitesides. Flash: a rapid method for prototyping paper-based microfluidic devices. *Lab on a Chip*, 8(12):2146–2150, 2008. (Cited on pages 66, 81, and 85.)

[132] AW Martinez, ST Phillips, GM Whitesides, and E Carrilho. Diagnostics for the developing world: microfluidic paper-based analytical devices. *Analytical Chemistry*, 82(1):3–10, 2009. (Cited on page 7.)

[133] AW Martinez, ST Phillips, GM Whitesides, and E Carrilho. Diagnostics for the developing world: Microfluidic paper-based analytical devices. *Analytical Chemistry*, 82(1):3–10, 2010. doi: 10.1021/ac9013989. URL http://pubs.acs.org/doi/abs/10.1021/ac9013989. PMID: 20000334. (Cited on page 64.)

[134] L Masini, M Cecchini, S Girardo, R Cingolani, D Pisignano, and F Beltram. Surface-acoustic-wave counterflow micropumps for on-chip liquid motion control in two-dimensional microchannel arrays. *Lab on a Chip*, 10(15):1997–2000, 2010. (Cited on page 14.)

[135] PJ Mazzone, J Hammel, R Dweik, J Na, C Czich, D Laskowski, and T Mekhail. Diagnosis of lung cancer by the analysis of exhaled breath with a colorimetric sensor array. *Thorax*, 62(7):565–568, 2007. doi: 10.1136/thx.2006.072892. URL http://thorax.bmj.com/content/62/7/565.abstract. (Cited on page 65.)

[136] A Menachery, D Graham, SM Messerli, R Pethig, and PJS Smith. Dielectrophoretic tweezer for isolating and manipulating target cells. *Nanobiotechnology, IET*, 5(1):1–7, 2011. (Cited on page 7.)

[137] AH Meng, N-T Nguyen, and RM White. Focused flow micropump using ultrasonic flexural plate waves. *Biomedical Microdevices*, 2(3):169–174, 2000. (Cited on pages 6, 79, and 90.)

[138] Long Meng, Feiyan Cai, Zidong Zhang, Lili Niu, Qiaofeng Jin, Fei Yan, Junru Wu, Zhanhui Wang, and Hairong Zheng. Transportation of single cell and microbubbles by phase-shift introduced to standing leaky surface acoustic waves. *Biomicrofluidics*, 5:044104, 2011. (Cited on page 12.)

[139] RM Moroney, RM White, and RT Howe. Microtransport induced by ultrasonic lamb waves. *Applied physics letters*, 59:774, 1991. (Cited on pages 6, 79, and 90.)

[140] F Mugele and J-C Baret. Electrowetting: from basics to applications. *Journal of Physics: Condensed Matter*, 17(28):R705, 2005. (Cited on page 7.)

[141] J Nam, H Lim, C Kim, JY Kang, and S Shin. Density-dependent separation of encapsulated cells in a microfluidic channel by using a standing surface acoustic wave. *Biomicrofluidics*, 6:024120, 2012. (Cited on page 12.)

[142] V Namasivayam, RG Larson, DT Burke, and MA Burns. Transpiration-based micropump for delivering continuous ultra-low flow rates. *Journal of Micromechanics and Microengineering*, 13(2):261–271, 2003. URL `http://stacks.iop.org/0960-1317/13/i=2/a=314`. (Cited on page 65.)

[143] SL Neale, MP MacDonald, K Dholakia, and TF Krauss. All-optical control of microfluidic components using form birefringence. *Nature Materials*, 4(7):530–533, 2005. (Cited on page 8.)

[144] NT Nguyen and Z Wu. Micromixers—a review. *Journal of Micromechanics and Microengineering*, 15:R1–R16, 2005. (Cited on page 68.)

[145] X Noblin, A Buguin, and F Brochard-Wyart. Vibrated sessile drops: Transition between pinned and mobile contact line oscillations. *Euro. Phys. J. E*, 14:395–404, 2004. (Cited on pages 23, 24, and 80.)

[146] X Noblin, A Buguin, and F Brochard-Wyart. Triplon modes of puddles. *Phys. Rev. Lett.*, 94:1–4, 2005. doi: 10.1103/PhysRevLett.94.166102. (Cited on page 24.)

[147] WL Nyborg. Acoustic streaming due to attenuated plane waves. *J. Acoust. Soc. Am.*, 25:1–8, Oct 1952. (Cited on pages 24, 27, 31, and 80.)

[148] C-D Ohl, M Arora, R Ikink, N de Jong, M Versluis, M Delius, and D Lohse. Sonoporation from jetting cavitation bubbles. *Biophysical journal*, 91(11):4285–4295, 2006. (Cited on page 80.)

[149] ND Orloff, JR Dennis, M Cecchini, E Schonbrun, E Rocas, Y Wang, D Novotny, RW Simmonds, J Moreland, I Takeuchi, and JC Booth. Manipulating particle trajectories with phase-control in surface acoustic wave microfluidics. *Biomicrofluidics*, 5 (4):044107–044107, 2011. (Cited on page 12.)

[150] A Oron, SH Davis, and SG Bankoff. Long-scale evolution of thin liquid films. *Rev. Mod. Phys.*, 69:931–980, 01 1997. URL `http://rmp.aps.org/abstract/RMP/v69/i3/p931_1`. (Cited on page 34.)

[151] JL Osborn, B Lutz, E Fu, P Kauffman, DY Stevens, and P Yager. Microfluidics without pumps: reinventing the T-sensor and H-filter in paper networks. *Lab on a Chip*, 10(20):2659–2665, 2010. (Cited on page 64.)

[152] MV Patel, AR Tovar, and AP Lee. Lateral cavity acoustic transducer as an on-chip cell/particle microfluidic switch. *Lab on a Chip*, 12(1):139–145, 2012. (Cited on page 80.)

[153] RL Peek and DA McLean. Capillary penetration of fibrous materials. *Industrial & Engineering Chemistry Analytical Edition*, 6(2):85–90, 1934. doi: 10.1021/ac50088a001. URL `http://pubs.acs.org/doi/abs/10.1021/ac50088a001`. (Cited on page 71.)

[154] F Petersson, A Nilsson, C Holm, H Jönsson, and T Laurell. Separation of lipids from blood utilizing ultrasonic standing waves in microfluidic channels. *Analyst*, 129(10):938–943, 2004. (Cited on page 81.)

[155] R Pethig. Review articleÑdielectrophoresis: Status of the theory, technology, and applications. *Biomicrofluidics*, 4:022811, 2010. (Cited on page 7.)

[156] A Qi, LY Yeo, and JR Friend. Interfacial destabilization and atomization driven by surface acoustic waves. *Physics of Fluids*, 20(7):074103, 2008. (Cited on pages 15, 23, and 65.)

[157] A Qi, JR Friend, LY Yeo, DAV Morton, MP McIntosh, and L Spiccia. Miniature inhalation therapy platform using surface acoustic wave microfluidic atomization. *Lab on a Chip*, 9(15):2184–2193, 2009. (Cited on pages 15, 64, 81, and 82.)

[158] A Qi, LY Yeo, JR Friend, and J Ho. The extraction of liquid, protein molecules and yeast cells from paper through surface acoustic wave atomization. *Lab on a Chip*, 10(4):470–476, 2010. (Cited on pages 11 and 65.)

[159] A Qi, P Chan, J Ho, A Rajapaksa, JR Friend, and LY Yeo. Template-free synthesis and encapsulation technique for layer-by-layer polymer nanocarrier fabrication. *ACS nano*, 5(12):9583–9591, 2011. (Cited on page 15.)

[160] A Renaudin, P Tabourier, V Zhang, JC Camart, and C Druon. Saw nanopump for handling droplets in view of biological applications. *Sensors and Actuators B: Chemical*, 113(1):389–397, 2006. (Cited on page 13.)

[161] A Renaudin, V Chabot, E Grondin, V Aimez, and PG Charette. Integrated active mixing and biosensing using surface acoustic waves (saw) and surface plasmon resonance (spr) on a common substrate. *Lab on a Chip*, 10:111–115, 2010. (Cited on page 81.)

[162] AR Rezk, O Manor, JR Friend, and LY Yeo. Unique fingering instabilities and soliton-like wave propagation in thin acoustowetting films. *Nat. Commun.*, 3:1167, November 2012. (Cited on pages 23, 26, 28, 43, 50, 60, and 89.)

[163] AR Rezk, A Qi, JR Friend, WH Li, and LY Yeo. Uniform mixing in paper-based microfluidic systems using surface acoustic waves. *Lab on a Chip*, 12(4):773–779, 2012. (Cited on pages 14, 81, 82, 83, 85, and 86.)

[164] AR Rezk, O Manor, JR Friend, and LY Yeo. Double flow reversal in thin liquid films driven by MHz order surface vibration. page under review, 2013. (Cited on pages 23, 26, 29, and 38.)

[165] N Riley. Oscillating viscous flows. *Mathematika*, 12:161–175, Nov 1965. (Cited on pages 24 and 47.)

[166] N Riley. Streaming from a cylinder due to an acoustic source. *J. Fluid Mech.*, 180:319–326, Aug 1986. (Cited on page 24.)

[167] N Riley. Acoustic streaming. *Theoret. Comput. Fluid Dynamics*, 10:349–356, Jan 1998. (Cited on pages 24, 32, and 34.)

[168] N Riley. Steady streaming. *Annu. Rev. Fluid Mech.*, 33:43–65, May 2001. (Cited on pages 24, 32, and 34.)

[169] Priscilla R Rogers, James R Friend, and Leslie Y Yeo. Exploitation of surface acoustic waves to drive size-dependent microparticle concentration within a droplet. *Lab on a Chip*, 10(21):2979–2985, 2010. (Cited on page 14.)

[170] CGJ Schabmueller, M Koch, ME Mokhtari, AGR Evans, A Brunnschweiler, and H Sehr. Self-aligning gas/liquid micropump. *Journal of Micromechanics and Microengineering*, 12(4): 420, 2002. (Cited on page 5.)

[171] WE Schiesser. *The Numerical Method of Lines*. Academic Press, San Diego, 1991. (Cited on page 39.)

[172] H Schlichting. Calculation of even periodic barrier currents. *Physik. Z.*, 33. (Cited on pages 10, 24, and 34.)

[173] H Schlichting and K Gersten. *Boundary–Layer Theory*. Springer–Verlag, Berlin, 8 edition, 2003. (Cited on pages 24 and 25.)

[174] SW Schneider, S Nuschele, A Wixforth, C Gorzelanny, A Alexander-Katz, RR Netz, and MF Schneider. Shear-induced unfolding triggers adhesion of von willebrand factor fibers. *Proceedings of the National Academy of Sciences*, 104(19):7899–7903, 2007. (Cited on pages 13 and 14.)

[175] J Scortesse, J-F Manceau, and F Bastien. Interaction between a liquid layer and vibrating plates: application to the displacement of liquid droplets. *J. Sound Vib.*, 254:927–938, 2002. (Cited on pages 23 and 24.)

[176] TW Secomb. Flow in a channel with pulsating walls. *J. Fluid Mech.*, 88:273–288, Jan 1978. (Cited on page 24.)

[177] J Shi, X Mao, D Ahmed, A Colletti, and TJ Huang. Focusing microparticles in a microfluidic channel with standing surface acoustic waves (ssaw). *Lab Chip*, 8(2):221–223, 2008. (Cited on page 12.)

[178] J Shi, D Ahmed, X Mao, S-CS Lin, A Lawit, and TJ Huang. Acoustic tweezers: patterning cells and microparticles using standing surface acoustic waves (ssaw). *Lab on a Chip*, 9(20): 2890–2895, 2009. (Cited on page 12.)

[179] RJ Shilton, MK Tan, LY Yeo, and JR Friend. Particle concentration and mixing in microdrops driven by focused surface acoustic waves. *Journal of applied physics*, 104(1):014910–014910, 2008. (Cited on pages 14, 76, 86, 89, 90, and 96.)

[180] K Shinoda, M Mishima, K Nakao, and K Munekane. Development of an artificial synapse using an electrochemical micropump. *Journal of Artificial Organs*, 7(4):210–215, 2004. (Cited on page 8.)

[181] S Shiokawa, Y Matsui, and T Ueda. Liquid streaming and droplet formation caused by leaky Rayleigh waves. In *Proceedings of the IEEE Ultrasonics Symposium*, pages 643–646, Montreal, Canada, Oct. 1989. (Cited on page 55.)

[182] K Sollier, CA Mandon, KA Heyries, L Blum, and CA Marquette. Òprint-n-shrinkÓ technology for the rapid production of microfluidic chips and protein microarrays. *Lab on a Chip*, 9(24): 3489–3494, 2009. (Cited on page 81.)

[183] HA Stone, AD Stroock, and A Ajdari. Engineering flows in small devices. *Annual Review of Fluid Mechanics*, 36(1):381–411, 2004. doi: 10.1146/annurev.fluid.36.050802.122124. URL `http://www.annualreviews.org/doi/abs/10.1146/annurev.fluid.36.050802.122124`. (Cited on page 64.)

[184] M Strani and F Sabetta. Free vibrations of a drop in partial contact with a solid support. *J. Fluid Mech.*, 141:233–247, 1984. (Cited on page 23.)

[185] AD Stroock, SKW Dertinger, A Ajdari, I Mezić, HA. Stone, and GM Whitesides. Chaotic mixer for microchannels. *Science*, 295 (5555):647–651, 2002. (Cited on pages 65 and 76.)

[186] JT Stuart. Double boundary layers in oscillatory viscous flow. *J. Fluid Mech.*, 24:673–687, Aug 1966. (Cited on pages 24, 34, and 47.)

[187] AP Sudarsan and VM Ugaz. Multivortex micromixing. *Proceedings of the National Academy of Sciences USA*, 103(19):7228–7233, 2006. (Cited on page 77.)

[188] H Suzuki and R Yoneyama. A reversible electrochemical nanosyringe pump and some considerations to realize low-power consumption. *Sensors and Actuators B: chemical*, 86(2):242–250, 2002. (Cited on page 8.)

[189] Y Takamura, H Onoda, H Inokuchi, S Adachi, A Oki, and Y Horiike. Low-voltage electroosmosis pump for stand-alone microfluidics devices. *Electrophoresis*, 24(1-2):185–192, 2003. (Cited on page 7.)

[190] D Taller, DB Go, and H-C Chang. Self-similar micron-size and nanosize drops of liquid generated by surface acoustic waves. *Phys. Rev. Lett.*, 109:224301, Nov 2012. doi: 10.1103/PhysRevLett.109.224301. URL `http://link.aps.org/doi/10.1103/PhysRevLett.109.224301`. (Cited on page 89.)

[191] MK Tan, JR Friend, and LY Yeo. Microparticle collection and concentration via a miniature surface acoustic wave device. *Lab on a Chip*, 7(5):618–625, 2007. (Cited on pages 13 and 55.)

[192] MK Tan, JR Friend, and LY Yeo. Interfacial jetting phenomena induced by focused surface vibrations. *Phys. Rev. Lett.*, 103:024501, Jul 2009. doi: 10.1103/PhysRevLett.103.024501. URL `http://link.aps.org/doi/10.1103/PhysRevLett.103.024501`. (Cited on pages 15 and 89.)

[193] MK Tan, LY Yeo, and JR Friend. Rapid fluid flow and mixing induced in microchannels using surface acoustic waves. *EPL (Europhysics Letters)*, 87(4):47003, 2009. (Cited on pages 12 and 14.)

[194] MK Tan, JR Friend, OK Matar, and LY Yeo. Capillary wave motion excited by high frequency surface acoustic waves. *Phys. Fluids*, 22:112112, 2010. (Cited on page 23.)

[195] MK Tan, LY Yeo, and JR Friend. Unique flow transitions and particle collection switching phenomena in a microchannel induced by surface acoustic waves. *Applied Physics Letters*, 97:234106, 2010. (Cited on page 12.)

[196] F Tolmon and J Wood. Fringe spacing in interference microscopes. *Sci. Instrum.*, 33:236, Jan 1956. (Cited on page 29.)

[197] AR Tovar and AP Lee. Lateral cavity acoustic transducer. *Lab on a Chip*, 9(1):41–43, 2009. (Cited on page 80.)

[198] FCM Van de Pol, HTG Van Lintel, M Elwenspoek, and JHJ Fluitman. A thermopneumatic micropump based on microengineering techniques. *Sensors and Actuators A: Physical*, 21(1):198–202, 1990. (Cited on page 5.)

[199] J Vanneste and O Buhler. Streaming by leaky surface acoustic waves. *Proc. R. Soc. Lond. A*, 467:1779–1800, 06 2011. (Cited on pages 31, 34, and 47.)

[200] S Vyawahare, S Sitaula, S Martin, D Adalian, and A Scherer. Electronic control of elastomeric microfluidic circuits with shape memory actuators. *Lab Chip*, 8(9):1530–1535, 2008. (Cited on page 5.)

[201] CY Wang. On high-frequency oscillatory viscous flows. *J. Fluid Mech.*, 32:55–68, Nov 2005. (Cited on page 24.)

[202] H Wang, P Iovenitti, E Harvey, and S Masood. Optimizing layout of obstacles for enhanced mixing in microchannels. *Smart Materials and Structures*, 11(5):662–667, 2002. URL `http://stacks.iop.org/0964-1726/11/i=5/a=306`. (Cited on page 76.)

[203] X Wang, S Wang, B Gendhar, C Cheng, CK Byun, G Li, M Zhao, and S Liu. Electroosmotic pumps for microflow analysis. *TrAC Trends in Analytical Chemistry*, 28(1):64–74, 2009. (Cited on pages 6 and 7.)

[204] Z Wang and J Zhe. Recent advances in particle and droplet manipulation for lab-on-a-chip devices based on surface acoustic waves. *Lab on a Chip*, 11(7):1280–1285, 2011. (Cited on page 64.)

[205] EW Washburn. The dynamics of capillary flow. *Physical Review*, 17(3):273–283, Mar 1921. doi: 10.1103/PhysRev.17.273. (Cited on page 71.)

[206] L Wei and L Gerhard. Investigations of droplet movement excited by lamb waves on a non-piezoelectric substrate. *Journal of Applied Physics*, 114(4):044501–044501, 2013. (Cited on page 83.)

[207] PJ Westervelt. The theory of steady rotational flow generated by a sound field. *J. Acoust. Soc. Am.*, 25:60–67, Oct 2004. (Cited on page 24.)

[208] AR Wheeler. Putting electrowetting to work. *Science*, 322(5901): 539–540, 2008. (Cited on page 7.)

[209] SE Widnall, DB Bliss, and C Tsai. The instability of short waves on a vortex ring. *Journal of Fluid Mechanics*, 66(1):35–47, 1974. (Cited on page 98.)

[210] ED Wilkes and OA Basaran. Nonlinear oscillations of pendant drops. *Phys. Fluids*, 9:1512–1528, 1997. (Cited on page 23.)

[211] A Wixforth, C Strobl, C Gauer, A Toegl, J Scriba, and ZV Guttenberg. Acoustic manipulation of small droplets. *Analytical and bioanalytical chemistry*, 379(7-8):982–991, 2004. (Cited on page 13.)

[212] D Wu, J Qin, and B Lin. Electrophoretic separations on microfluidic chips. *Journal of Chromatography A*, 1184(1):542–559, 2008. (Cited on page 7.)

[213] Z Wu and N-T Nguyen. ConvectiveâĂŞdiffusive transport in parallel lamination micromixers. *Microfluidics and Nanofluidics*, 1:208–217, 2005. ISSN 1613-4982. URL `http://dx.doi.org/10.1007/s10404-004-0011-x`. 10.1007/s10404-004-0011-x. (Cited on page 74.)

[214] D Xu, L Wang, G Ding, Y Zhou, A Yu, and B Cai. Characteristics and fabrication of niti/si diaphragm micropump. *Sensors and Actuators A: Physical*, 93(1):87–92, 2001. (Cited on page 5.)

[215] J Xu and D Attinger. Acoustic excitation of superharmonic capillary waves on a meniscus in a planar microgeometry. *Phys. Fluids*, 19:108107, 2007. doi: 10.1063/1.2790968. (Cited on page 24.)

[216] P Yager, T Edwards, E Fu, K Helton, K Nelson, MR Tam, and BH Weigl. Microfluidic diagnostic technologies for global public health. *Nature*, 442:412–418, July 2006. doi: 10.1038/nature05064. (Cited on page 64.)

[217] Z Yang, S Matsumoto, H Goto, M Matsumoto, and R Maeda. Ultrasonic micromixer for microfluidic systems. *Sensors and Actuators A: Physical*, 93(3):266–272, 2001. (Cited on page 90.)

[218] GG Yaralioglu, IO Wygant, TC Marentis, and BT Khuri-Yakub. Ultrasonic mixing in microfluidic channels using integrated transducers. *Analytical Chemistry*, 76(13):3694–3698, 2004. (Cited on page 79.)

[219] LY Yeo and H-C Chang. Static and spontaneous electrowetting. *Modern Physics Letters B*, 19(12):549–569, 2005. (Cited on pages 7 and 26.)

[220] LY Yeo and H-C Chang. Electrowetting films on parallel line electrodes. *Phys. Rev. E*, 73:011605, 2006. (Cited on page 26.)

[221] LY Yeo and JR Friend. Surface acoustic wave microfluidics. *Annual Review of Fluid Mechanics*, page to appear. (Cited on pages 81 and 86.)

[222] LY Yeo and JR Friend. Ultrafast microfluidics using surface acoustic waves. *Biomicrofluidics*, 3(1):012002, 2009. ISSN 19321058. doi: DOI:10.1063/1.3056040. URL `http://dx.doi.org/doi/10.1063/1.3056040`. (Cited on pages 11, 24, 64, 67, and 82.)

[223] LY Yeo, H-C Chang, PPY Chan, and JR Friend. Microfluidic devices for bioapplications. *Small*, 7(1):12–48, 2011. ISSN 1613-6829. doi: 10.1002/smll.201000946. URL `http://dx.doi.org/10.1002/smll.201000946`. (Cited on pages 3, 6, 63, and 64.)

[224] Z Yin and A Prosperetti. A microfluidic'blinking bubble'pump. *Journal of Micromechanics and microengineering*, 15(3):643, 2005. (Cited on page 8.)

[225] Y Zhou and F Amirouche. An electromagnetically-actuated all-pdms valveless micropump for drug delivery. *Micromachines*, 2(3):345–355, 2011. (Cited on page 5.)

[226] M Zimmermann, S Bentley, H Schmid, P Hunziker, and E Delamarche. Continuous flow in open microfluidics using controlled evaporation. *Lab on a Chip*, 5(12):1355–1359, 2005. (Cited on page 65.)